

## ABSTRACT

Title of dissertation: COOLING AND STABILIZATION OF  
GRAPHENE NANOPATELETS  
IN HIGH VACUUM

Pavel Nagornykh, Doctor of Philosophy, 2015

Dissertation directed by: Dr. Bruce E. Kane  
Laboratory for Physical Sciences

The study of 2D materials is a rapidly growing area of research, where the ability to isolate and probe an individual single-layer specimen is of high importance. The levitation approach serves as a natural solution for this problem and can be used in ways complementary to the standard techniques. Experiments, including study of properties at high or close to melting temperatures, stretching, folding, vibration and functionalization, can be conducted on levitated 2D materials. As a first step towards realization of all these ideas, one needs to develop and test a system allowing for control over the thermal state and orientation of mono-layer flakes.

In this thesis, I present the results of implementation of the parametric feedback cooling scheme in a quadrupole ion trap for stabilization and cooling of graphene nanoplatelets. I have tested and showed that the feedback allows to stabilize levitated graphene nanoplatelets in high vacuum conditions ( $< 10^{-6}$  Torr) to have trapped life times longer than a week. Cooling of the center of mass motion to temperatures below 20 K for all translational degrees of freedom was observed.

I have also studied the coupling of DC patch potentials, which were found to be present in the high vacuum chamber. Their effect on cooling was studied and the protocol for minimizing the noise coupling created by the DC fields was designed. We have shown that by varying DC voltages on a set of auxiliary DC electrodes, placed near the trap, one can balance out the DC fields and achieve the lowest cooling temperature. The settings corresponding to this temperature were measured to have a slow drift in time. Ability to tune the settings to balance this drift without breaking the vacuum was studied and found to be a viable solution for the drift cancellation.

In addition, our effort in characterization of the flakes is presented. It was shown that the flake discharge quantization observed during the initial pumping down of the high vacuum chamber allows to extract absolute values of flake mass and charge. I also mention the issues experienced with estimation of the shape of the flake, as well as its temperature based on an equipartition theorem.

Finally, I discuss the preliminary data on the precession and reorientation of the flakes in the presence of circularly polarized light (CPL) and DC stray fields. The dependence of flake orientation on the offset from the nulling settings is observed and is explained in terms of basic model of a solid charged disk in the presence of two torques created by CPL and DC stray fields.

COOLING AND STABILIZATION OF  
GRAPHENE NANOPATELETS IN HIGH VACUUM

by

Pavel Nagornykh

Dissertation submitted to the Faculty of the Graduate School of the  
University of Maryland, College Park in partial fulfillment  
of the requirements for the degree of  
Doctor of Philosophy  
2015

Advisory Committee:

Dr. Bruce E. Kane, Advisor  
Professor Dennis H. Drew, Chair  
Professor Christopher R. Monroe  
Professor Christopher J. Lobb  
Professor Ichiro Takeuchi

© Copyright by  
Pavel Nagornykh  
2015

## Acknowledgments

I believe that finishing Ph.D. would be impossible for me, if not for the help and support of many people I had a joy of interacting with. Some helped me, when I felt down or not sure what to do next, others helped by sharing their knowledge and experience. Although, I face a challenge of remembering everyone I would like to thank without missing some name, I will try my best by listing their names below.

I am strongly indebted to my advisor Dr. Bruce E. Kane for showing me how exciting and challenging the experimental science can be. He was always on the spot, when it came to figuring out what the obstacle in the experiment was as well as suggesting the solution. In a similar way, Dr. Michael Dreyer made me truly appreciate the importance of design and implementation of individual components, and how by making the right modification, one can simplify and speed up the research.

In my early years of Ph.D., when I was working on theoretical research in condensed matter, my interaction with Prof. Victor Yakovenko and Prof. Victor Galitski had shaped my attitude towards a given problem and provided me with a lot of insight in the theory of solid state, which serves me up to this day.

I want to specially thank my friend, Kostya Nesterov, with whom I had numerous discussions about science, life and pretty much anything there is to discuss. He helped me to overcome many challenges and was always there and ready to provide an advice. In more than ten years I have known him, Kostya affected my view of the world in uncountable ways and I think that it helped me to become better as a result.

My mom was the other person who believed in me, no matter what problems and

challenges I have faced, and its her unconditioned love, assistance and the guidance that gave me energy and belief in myself, necessary for working through the Ph.D. program.

As far as my collaborators and senior colleagues go, Rusko Ruskov and William Cullen shared their wisdom about theory and experiment with me many times. Specifically, Rusko Ruskov helped me to understand the big picture of stochastic processes and suggested some programming ideas that were extremely useful for my numerical simulations work. William Cullen and a graduate student working in his lab under guidance of Prof. Michael Fuhrer, Jacob Tosado, are two of very smart and talented experimental scientists that always had some thoughts and projects that left me in owe and sparked my own thinking process.

My groupmates, Joyce Coppock and Ian McAdams, were working on the project with me and their effort and hard work were crucial in getting the results I present in the thesis.

Many graduate students I have interacted with over the years proved to be friendly, brilliant and kind people and I am thankful to each of them for our time together. Here, I would like to especially point out Yaniv Rosen (it was no easy task to help me in picking up the doughnuts for the defense talk), Sergey Novikov (and Yaniv) for having multiple lunches together, which were filled with talk over all aspects of life, Sergey Pershoguba and Dmitry Kashin for giving me advice over the final months of my Ph.D. on how to grind through the thesis writing. Anita Roychowdhury, Moe Khalil, Bala Suri, Bahman Sarabi and many others were sharing the graduate beachhead room with me, and speaking with them allowed me to learn many new things, which were

often outside of my immediate study. Vitaley Zaretsky, Kevin Meagher and Simon Slutsky were the people who I hang out with outside of the work on Fridays, and the Friday movie club was my introduction to many rare and unusual movies I would have probably missed otherwise.

Margaret Lukomska and Jane Hessing were invaluable in solving the administrative and procedural situations in a quick and efficient way, making it very easy to concentrate on research.

I am grateful to Prof. Dennis H. Drew who I have often bothered with signing up the necessary paperwork and who trusted Dr. Kane and me in finishing this project while on a short time schedule.

I would also like to thank the rest of the members of my committee - Prof. Ichiro Takeuchi, Prof. Christopher R. Monroe and Prof. Christopher J. Lobb - for providing a feedback about this thesis as well as raising interesting questions and suggesting future directions for the experiments.

---

## Table of Contents

---

List of Figures	viii
1 Introduction	1
1.1 Benefits of levitation method	2
1.1.1 Mechanical study	2
1.1.2 Thermal study	3
1.1.3 Functionalization	4
1.2 Previous work	5
1.2.1 Previous experiments on levitated particles	5
1.2.2 Levitated graphene experiments 2010	7
1.2.3 Problem of low life times in trap in high vacuum	8
1.3 Main results	9
1.3.1 Particle cooling and stabilization	9
1.3.2 Stray fields minimization	11
1.3.3 Particle characterization	12
1.3.4 Preliminary data on precession	13
1.4 Thesis outline	13
2 Ion trap theory and experiment	16
2.1 Requirements on trapping potential	16
2.2 AC approach and equations of motion	18
2.2.1 Mechanical analogy	18
2.2.2 Quasipotential approach	19
2.2.3 Mathieu equations and exact solutions	22
2.2.4 Search for stability of the solution	26
2.2.5 Patch field gradients effect on eigenfrequencies	27
2.3 Paul trap geometries	29
2.3.1 Hyperbolic shape	29
2.3.2 Graphene trap	29
2.3.3 Duffing equation	34
2.3.4 Typical operating parameters	34

3	Experimental setup	36
3.1	Overall system	36
3.2	Particle introduction to the system	38
3.3	Front chamber and particle detection	42
3.4	Particle transfer	43
3.5	Back chamber and particle detection	45
3.5.1	Signal detection	45
3.5.2	Knifeedge prism beam splitter	47
3.6	Electronics	50
3.7	Auxiliary electrodes	52
4	Parametric feedback : theory and limitation by noise	54
4.1	Parametric feedback principle	54
4.1.1	Parametric feedback effect on damping	56
4.1.2	Dependence of cooling on gain	58
4.1.3	Noise effect on the feedback	59
4.2	Derivation of equations of motion	60
4.2.1	Effect of DC fields	62
4.2.2	Alternative explanation of DC noise coupling	64
4.2.3	Numerical simulation	66
4.3	Conclusions	67
5	Field Programmable Gate Array (FPGA) control	68
5.1	FPGA overview	68
5.2	Signal amplification and balancing	70
5.3	Signal filters and signal phase shift	72
5.4	Feedback generation	75
5.5	Correction of lens position	77
6	Flakes in high vacuum	79
6.1	Calibration of signal	79
6.2	Particle behavior at high vacuum	82
6.2.1	Behavior in high vacuum without cooling	83
6.3	Cooling vs. amplitude modulation	84
6.3.1	Cooling dependence on laser power	86
6.4	Warm up and cool down tests	88
7	Effect of DC fields on cooling	93
7.1	Nulling of DC stray fields	95
7.1.1	Nulling settings dependence on time	98
7.1.2	Flake stabilization with circularly polarized light	99
7.2	Flake reorientation vs. DC stray fields	100
7.2.1	Conclusions	104

8	Particle characterization	106
8.1	Mass and charge extraction . . . . .	106
8.1.1	Reproducibility of charge and mass estimates . . . . .	109
8.2	Alternative estimation of temperature . . . . .	110
8.3	Discussion of the flake shape . . . . .	112
8.3.1	Dependence of S/N ratio in CCD intensity on pressure . . . . .	114
9	Conclusions and future work	116
9.1	Conclusions . . . . .	116
9.1.1	Cooling and stabilization . . . . .	116
9.1.2	Effect of DC stray fields on cooling . . . . .	117
9.1.3	Particle characterization . . . . .	118
9.1.4	Particle precession : preliminary data . . . . .	118
9.2	Future work . . . . .	119
A	Electric fields nulling	122
B	Cooling and stabilization protocol	125
B.1	Damping of intensity fluctuations via CPL . . . . .	126
	Bibliography	128

---

## List of Figures

---

1.1 (a) Image of a particle (small bright dot under the blue arrow) as trapped in the trap potential; (b) Particle intensity when linearly/circularly polarized light is used at pressure below $10^{-5}$ Torr. Variations in the intensity prove the particles aspheric shape. . . . .	8
1.2 Dependence of temperature (a), pressure (b) and feedback gain (c) on time during the pumping of the system before and after the feedback cooling is turned on. It can be seen that particle goes from a temperature of 300 K at high pressures (5-10 mTorr) and no feedback to temperature below 20 K at low pressure ( $4 \cdot 10^{-7}$ Torr) and feedback turned on. . . . .	10
1.3 Dependence of cooling on pressure (a), feedback gain in AM % (b) and stray fields optimization done by varying auxiliary electrode's voltage (c)	11
1.4 (a) Dependence of eigenfrequency along $Z$ axis on time; (b) Dependence of average intensity of the particle on voltage settings and laser power level (dashed - $245 \mu\text{W}$ , solid - $145 \mu\text{W}$ ); (c) Precession of the particle intensity after the change in an auxiliary electrode setting at different values of electrode offsets. . . . .	15
2.1 Exact solution of Mathieu equation, when quasipotential approximation is valid (blue line; $a = 0$ and $q = 0.04$ ) and when there is no distinction between micro- and macro- motion (red line; $a = 0$ and $q = 0.905$ , where $q$ is chosen to be close to instability boundary $q_{crit} = 0.91$ )	24
2.2 Stability (yellow-filled) regions for: (a) Mathieu Equation; (b) Quadrupole Ion trap with $\alpha = \beta = -\gamma/2$ (three Mathieu equations); (c) Quadrupole Ion trap with $\alpha = 1.5\beta = -2.5\gamma$ . Notice qualitative similarity to case (b).	27
2.3 Graphene Trap: (a) General view (outer electrode is shown in red and inner electrode in green); (b) View from above; (c) Potential distribution; (d) Photo of the currently used trap version. . . . .	30
2.4 Trap potential dependence along $X$ (red), $Y$ (green) and $Z$ (blue) trap axes for a trap with (left side) and without (right side) the slot. . . . .	32
3.1 Overall view of the experimental setup as viewed from above. . . . .	37

3.2	Images of front chamber with the electrospray setup on top of it (a) and back chamber (b). . . . .	38
3.3	Electrospray scheme as viewed from the side. . . . .	39
3.4	General view of the <i>FRONT</i> chamber (as viewed from above) and corresponding optical setup. . . . .	42
3.5	(a) View of the UHV chamber as viewed through one of the chamber windows. Motion of two traps (color coded for convenience) relative to each other can be seen. (b) Schematic protocol of transferring particle from one trap to another. Gray disk represents the particle and serves as a visual guidance showing which trap particle is in. . . . .	44
3.6	(a) General view of the <i>BACK</i> chamber as viewed from above and corresponding optical setup; (b) Pseudo-3D schematic of the optical setup is shown, including the relative orientation of 532 nm laser, 671 nm laser and the prism setup (prism + two photodetectors). Rotation axis denotes the axis around which the prism setup can be rotated. . . . .	46
3.7	(a) Schematic description of particle motion detection with a help of a prism knifeedge beam splitter; (b) Projection of particle motion in case of the knifeedge orientation at 0, 90 and 54.5 degrees . . . . .	48
3.8	Electronics Scheme. . . . .	50
3.9	(a) View from above of the relative position of auxiliary electrodes and the particle trap (b) Photo of the trap showing the auxiliary electrodes. The grounded shield, shown in the photo, is used for minimizing the interaction between the wiring and residual charge voltages and the particle motion in the trap. . . . .	52
4.1	Transition of the particle motion, when parametric modulation at twice the frequency is turned on (a) and when the feedback modulation is turned on (b) . . . . .	55
4.2	(a) Numerical Simulation of $T$ dependence on DC stray field value $E_{dc}$ . The fit with $C_0$ , $C_2$ and $C_4$ is shown as dashed black curves and same values of the coefficients were used to fit all three curves. Gain settings of $k_1 = 0.032$ (red), $k_1 = 0.169$ (green) and $k_1 = 0.545$ (blue) were chosen for simulation. (b) Numerical Simulation of $T$ dependence on feedback gain $k_1$ at different stray fields strengths. The yellow arrows are shown for both plots to point the direction, which the feedback strength (a) and stray fields strength (b) are increased. . . . .	65
5.1	Scheme of FPGA integration in the experiment. . . . .	69
5.2	Schematics of FPGA VI. . . . .	70
5.3	Schematics of loop for signal amplification. . . . .	70
5.4	Measured signals from photodetectors $A$ and $B$ vs. inner electrode voltage. . . . .	71
5.5	Feedback loop consists of two subloops. First loop is used for signal filtering. The second generates a product of the signal by its derivative and scales the product based on gain $G_F$ . . . . .	73

5.6	Phase shift of generated feedback signal relative to the ideal feedback signal for three different values of filter settings. At phase shifts greater than 90 degrees, the feedback leads to heating rather than to cooling of the particle motion. . . . .	76
6.1	Power spectrum of signal $S$ at pressure of 4 mTorr (a) and $4 \times 10^{-7}$ Torr (b). . . . .	80
6.2	Peaks' dependence on pressure (a) and time (b) for motion along $X$ (red), $Y$ (green) and $Z$ (blue) axes. . . . .	82
6.3	Comparison of different regimes of particle motion (description in the text). Curves are labeled as red ( $T_x$ ), green ( $T_y$ ) and blue ( $T_z$ ). . . . .	83
6.4	Dependence of cooling on (a) Amplitude Modulation ( $G_{AM}$ ) and (b) FPGA gain ( $g$ ). . . . .	87
6.5	Dependence of $T_z$ on $G_{AM}$ at three different laser power levels. . . . .	88
6.6	Typical dependence of warm up of the particle motion, once the feedback is turned off. Four temperature trajectories, labeled 1-4, are shown for relative comparison. The difference of time dependence between the trajectories is a sign of stochastic nature of the particle heating. . .	91
6.7	3D Histogram of particle heating up [contains 197 heat up curves]. . .	92
7.1	Dependence of particle position, as measured by CCD camera, on FPGA settings of electrodes $V_{10}/V_2/V_6$ . Linear fit is shown for comparison with measured data points. . . . .	94
7.2	Dependence of temperature on electrode voltage near the nulling settings ( $T_x$ - red, $T_y$ - green, $T_z$ - blue): (a) vs. offset in $V_{10}$ , (b) vs. offset in $V_2$ , (c) vs. offset in $V_6$ . . . . .	97
7.3	Drift of auxiliary electrodes settings vs time. . . . .	98
7.4	Dependence of particle temperature (a) and CCD intensity (b) on time. Grey and orange vertical lines show the times, when the CPL laser is turned off and on. Sphere and disk represent the chaotic spinning of the flake and the CPL stabilized spinning correspondingly. . . . .	100
7.5	Schematic depiction of how the interaction between the CPL produced torque (red) and the patch fields torque (blue) is expected to lead to the reorientation of the flake rotation. Increase in the patch fields torque is assumed from left to right and would correspond to experimental case of moving away from the nulling settings. . . . .	101
7.6	Comparison of transient behavior of particle intensity at CPL of (a) 245 $\mu\text{W}$ and (b) 145 $\mu\text{W}$ . Curves of the same color correspond to the switching to the same offset values. . . . .	102
7.7	Comparison of average intensity dependence on offset of $V_{10}$ from nulling settings at CPL power of 145 $\mu\text{W}$ (black) and 245 $\mu\text{W}$ (red). Dashed lines represent the levels of intensity measured at 10 mTorr with no cooling at corresponding CPL power levels. Lines going through the data points are shown for a visual guidance. . . . .	104

7.8	Transient oscillations of intensity observed at red laser power of (a) 145 $\mu\text{W}$ and (b) 245 $\mu\text{W}$ . . . . .	105
8.1	Dependence of frequency shift on time for $f_x$ (a), $f_y$ (b) and $f_z$ (c) . . .	108
8.2	Comparison of six (6) consecutive discharge series, used to independently extract the minimum frequency jump $\delta\omega_z$ . . . . .	110
8.3	Comparison of dependence of $P_S(\omega = 0)$ on particle displacement along Z at three different focusing settings. . . . .	113
8.4	(a) Schematic representation of the particle reorientation during the photcounter averaging at different regimes, corresponding to different ratios between the damping $\Gamma$ and the measurement time $T_m$ . (b) Dependence of the signal to noise ratio of the photocount number on the pressure. . . . .	115

## Introduction

---

The discovery of graphene in 2004 [1] rekindled interest in study of layered materials [2]. Realization that single layered 2D systems can be separated and individually studied led to new proposals for fundamental experiments and industrial applications [3]. Initial lack of interest in the research on monolayer systems partially stemmed from the assumed thermal instability and folding of 2D materials, which were theoretically predicted [4,5]. Another issue was a perceived complexity of effort required to create monolayered samples. For example, scratching of graphite nanopillars attached to an atomic force microscopy (AFM) probe [6] was tested as method to create graphene samples during the same year, when graphene was first produced with a use of a scotch tape [1].

Within next ten years after discovery, it was shown that large quantities of graphene can be produced in many different ways - mechanical exfoliation [1], chemical vapor deposition [7] and epitaxial growth on SiC substrate [8]. At the same time, the

methodology for graphene study and its characterization were fine tuned and developed [9]. This surge in experiments benefited not only the graphene, but the whole field of 2D materials, where graphene-tested techniques were used to produce materials like silicene [10], graphane [11], germanane [12] and many more. The growth of the field of 2D materials inspired discussion about replacing silicon, as an electronics industry standard, with hybrid layered systems consisting of mixed monolayers [2,3]. These structures are expected to be capable of combining high thermal and electrical conductivity, and variable band gap in one device, while still being only a few atomic layers thin. At the same time, since any industrial application requires a good understanding of the underlying system, there is a lot of work to be done on characterization of the properties of all these materials, and research on new methods for fast and precise measurements of 2D materials is always welcome.

## 1.1 Benefits of levitation method

While usual techniques used for study of 2D materials are often sufficient for the research, there are regimes and conditions that can require development of new methods. In this regard, flakes levitation in the quadrupole ion trap, approach used in our experiments, has some unique advantages. Here, we briefly list some of experiments that become possible via the levitation of 2D materials.

### 1.1.1 Mechanical study

A trapped 2D flake is not connected to any wires or a substrate, and its motion around the center of mass is completely free, following the free membrane dynamics.

If one were to use a combination of tunable circularly polarized light beams, one could realize a full control over the orientation and spinning [13] of the flake, positioning the flake based on the experimental requirements. Study of flake vibrations can be used to search for flexural phonons, unique phonon mode of 2D systems, that strongly affect thermal conductivity and charge carrier mobility of monolayered materials [14–16].

Varying the frequency of the spinning will modify the amount of stress the flake is under due to centrifugal forces. By varying the amount of stress one can examine behavior of the material under the critical stress or stretch it to a required lattice spacing. The stretched flake can be deposited on a substrate of choice afterwards, where effects of lattice mismatch on the properties of 2D materials on a substrate can be studied.

### 1.1.2 Thermal study

Thermal properties of 2D materials are also challenging to measure [2], since the behavior of a mono-layered system is strongly affected by its environment. For levitated flakes, there is close to no interaction between the flakes and the rest of the world, when the trap is placed in the ultra-high vacuum chamber. Therefore, experiments on properties of the material at high temperatures or at temperatures close to melting (estimated to be as high as 4510 K for graphene [17]) can be conducted.

Study of non-equilibrium dynamics [18, 19] of free flakes is another area of research, where usually used study on statistical ensembles of similar particles reaches a resolution limitation. Phenomena like deviations from equipartition theorem under trap anharmonicity effect [20], test of Landauer's principle [21] and measurements

of random walk with ultra-high resolution [22] have been observed on trapped particles so far. For 2D flakes, the spectrum of possible experiments extends even more, including research on thermal folding [23] and thermal vibrations at different flake thicknesses and sizes.

### 1.1.3 Functionalization

The functionalization of 2D materials is of interest in various areas of industry and fundamental research. Since properties and the flatness of monolayer flakes are easily modified depending on what chemicals the surface of the flake interacts with, flake folding [24], twisting [25] or rolling/unrolling can be analyzed after the flake exposure to a given chemical substance [23, 26, 27]. For example, study of unfolding/-folding of graphene during absorption/desorption of adsorbates, as predicted theoretically for the case of graphene [23], can be done via exposing graphene flakes to proper chemicals/heating the flakes above the evaporation temperature of the adsorbate. Similarly, deposition of charge on the flakes or their discharge can be used to create a transition between stable and unstable configurations of the 2D sheets, when van der Waals interaction overcomes the electrostatic repulsion of the flake edges.

A discussion of microparticles assembly processes with applications to photonic nanostructures and nanoantennas was recently published with a protocol involving particle pre-characterization and combination in the segmented Paul trap [28]. It was shown that if separate parts of the trap are used to trap oppositely charged microparticles, and particles are placed next to each other, the resulting Coulomb interaction will produce a stable nanoassembly. This approach can be considered an extension of the

functionalization one, where the functionalization helps to study particle properties modification after minor collisions.

## 1.2 Previous work

### 1.2.1 Previous experiments on levitated particles

Initial development of levitation techniques began in the early 1950s with experiments on mass spectrometry and trapping of charged particles via quadrupole potential geometry. Over the next sixty years, it was shown that particles of all sizes from mm-sized spheres [29] down to individual ions can be trapped [30], if the right design and trap operating parameters are chosen. While initial geometry relied on use of three or four electrodes set to surround the trap volume for high potential symmetry, modern designs (planar [31], stylus [32] and linear trap [33, 34] geometries) aim for a high access angle and fine tuning of the particle behavior in the trap is done by using end electrodes of the trap [35].

Invention of electrodynamic trapping, was followed by optical trapping based on a single upwards-propagating focused beam geometry [36]. Within the next fifteen years, optical trapping was improved to provide trapping of the flakes in all three dimensions down to pressures of  $10^{-6}$  Torr [37, 38]. At the same time, it became clear that temperature control of the trapped particles is necessary and some sort of feedback is required, since natural dissipation channels stop being efficient in high and ultra high vacuum conditions [37, 39].

A shift from quadrupole ion trapping to the optical experiments on micro- and

nanoparticles [40] followed, where the most recent research was concentrated on development of cooling of the trapped particles. One of the lowest temperatures observed on laser-cooled microparticle in a vacuum, 1.5 mK, has been created by use of three external lasers for cooling [41]. Alternative methods, relying on cavity cooling of nanoparticles [42, 43] and parametric feedback cooling [44] were found to work as well and to produce similar levels of cooling.

Aside of stabilizing the particle motion, the cooling is looked into as a way to reach ultra-high pressure regime, where quality factor values of up to  $10^{12}$  are expected [39]. High quality factor and low temperatures are required for experiments on macroscopic quantum mechanics, where creating a ground state of macroscopic object (nano- or microparticle) while keeping its coherence (high Q factor) are the ultimate goals [13, 45, 46]. One of the most recent proposals includes use of nanodiamonds, where development of nanoscale interferometry with nitrogen vacancy centers on a cooled nanodiamond is currently under way [47].

Another direction of research currently explored is the use of nanoparticles to characterize the environment. Study of radiation pressure forces experienced by particles in a quadrupole pole trap based on momentum transfer was conducted in Ref. [48]. Experiments targeting detection of exotic forces such as non-Newtonian gravity corrections and Casimir forces [49], and search for millicharged particles (elementary particles with charge much lower than an electron charge) [50] have been proposed and conducted. Resolution of these experiments was estimated to be close to or even better than a state of the art AFM resolution.

Characterization of particles themselves involving detection of absolute charge and

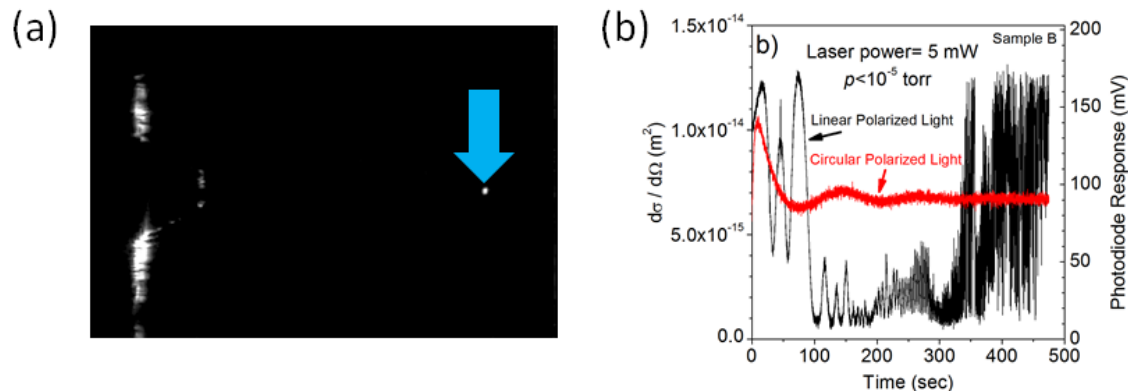
mass of the particles was shown to be viable based on charge/discharge measurements, where such techniques as soft X-rays [51] and an electron gun charging [52] were implemented for study of SiO<sub>2</sub> nanoparticles. Similar experiments were conducted on more complex particles like quantum dot nanocrystals CdSe/ZnS [53], where high resolution tracking of changes in mass and charge can shed light on chemical processes by tracing changes in eigenfrequency of the particle motion.

Finally, the whole field of stochastic processes can be sampled with a nanoscale resolution at a rate much faster than previously achievable, where an optical detection of particle motion was used to extract information about particle temperature and motion. Previously mentioned Brownian motion study [22] and relaxation of nanoparticle to thermodynamic equilibrium [19] are among the most recently published papers in this area. Measurements of gas temperature with nanoscale resolution, dependence of accommodation coefficient on particle environment and nanoparticle melting were studied [54], where memory effects in the Brownian motion, entropy production and micro-rheology have been mentioned as future directions for the experiments.

### 1.2.2 Levitated graphene experiments 2010

Since use of optical trapping of 2D materials will have such issues as flake orientation locking to the optical trap profile [55], as well as heating up under the laser beam pressure, the quadrupole trapping approach presents a complementary technique to previously discussed optical trapping experiments. Another reason, why quadrupole trapping was used for measurements on graphene flakes, as conducted in 2010 [56], was to prevent a folding of 2D flake [57] by creating a net flake charge.

**Figure 1.1:** (a) Image of a particle (small bright dot under the blue arrow) as trapped in the trap potential; (b) Particle intensity when linearly/circularly polarized light is used at pressure below  $10^{-5}$  Torr. Variations in the intensity prove the particles aspheric shape.



A homemade experimental setup with a quadrupole ion trap set in a vacuum chamber was used for the original experiments (see Fig. 1.1.a, where the trapped flake image relative to the trap can be seen). High aspect ratio of the trapped particles optical response was observed (hinting that they are indeed asymmetric as expected for graphene flakes, Fig. 1.1.b), and preliminary estimates on charge, mass, and size of the particles were presented. Although it was estimated that only multilayer flakes were studied in the paper, the trapping of a single layer flakes using the same setup was predicted to be possible if enough effort and care were taken [56].

### 1.2.3 Problem of low life times in trap in high vacuum

One of the key problems encountered in the levitation experiments in 2010 was reminiscent of problems of optical trapping. It was found that the time flakes stay trapped before escaping reduced from timescale longer than a week at mTorr level pressure [56] down to less than a day in UHV conditions.

Possible explanation for this effect involves overheating of the particle motion by a noise source. In the case of the quadrupole trap this can be either heating by the laser beam used for imaging the particle or some form of coupling between the external noise sources and the particle motion that leads to parametric heating [54]. One of the ways to solve this issue is by creating an additional dissipation channel, large enough to divert any heating of the flake motion, e.g. by adding an active feedback scheme, where the damping becomes proportional to the size of particle oscillations in the trap and the particle motion is cooled [44,58].

A similar active feedback scheme is implemented in our system, where a parametric feedback is generated at twice the frequency of the trap motion at a phase locked to the particle motion, leading to the energy dissipation. The resulting cooling and its optimization are studied in detail and were the goal of our project.

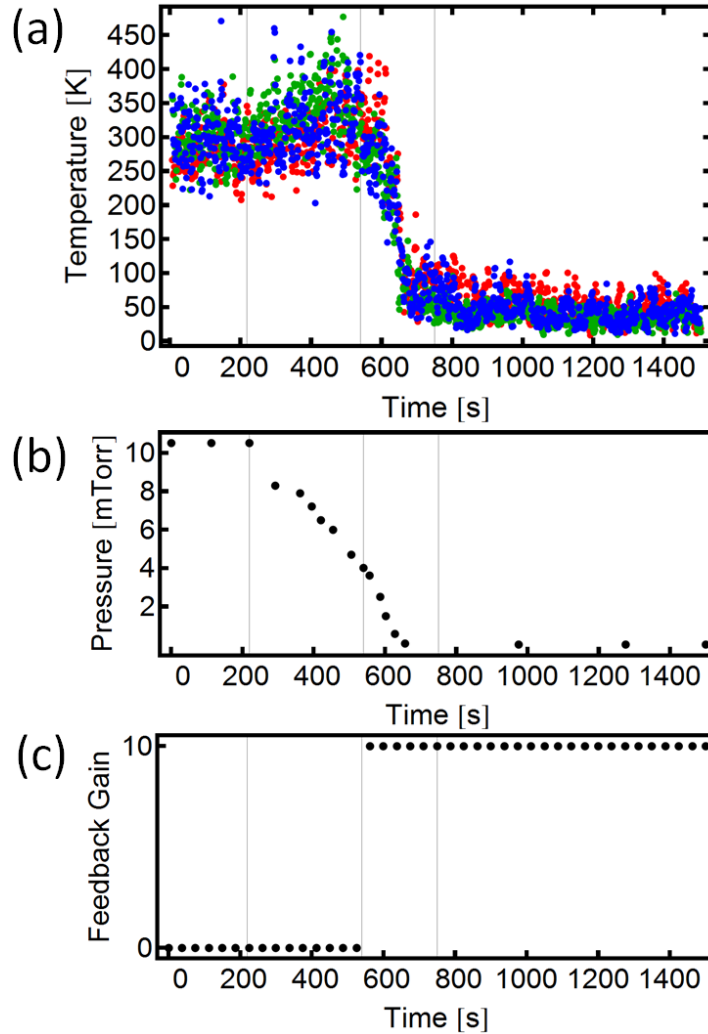
## 1.3 Main results

This thesis presents the progress and results of study on implementation of parametric feedback technique for stabilization and cooling of microparticles under high vacuum conditions (pressures in the range of  $0.5\text{-}1\ \mu\text{Torr}$ ). The main results are briefly discussed in the following subsections and their full description as well as the experimental setup comprise the rest of the thesis.

### 1.3.1 Particle cooling and stabilization

We have shown that the feedback scheme implemented in our experiment increases the time the particles can stay in the trap at high vacuum well above a few

**Figure 1.2:** Dependence of temperature (a), pressure (b) and feedback gain (c) on time during the pumping of the system before and after the feedback cooling is turned on. It can be seen that particle goes from a temperature of 300 K at high pressures (5-10 mTorr) and no feedback to temperature below 20 K at low pressure ( $4 \cdot 10^{-7}$  Torr) and feedback turned on.

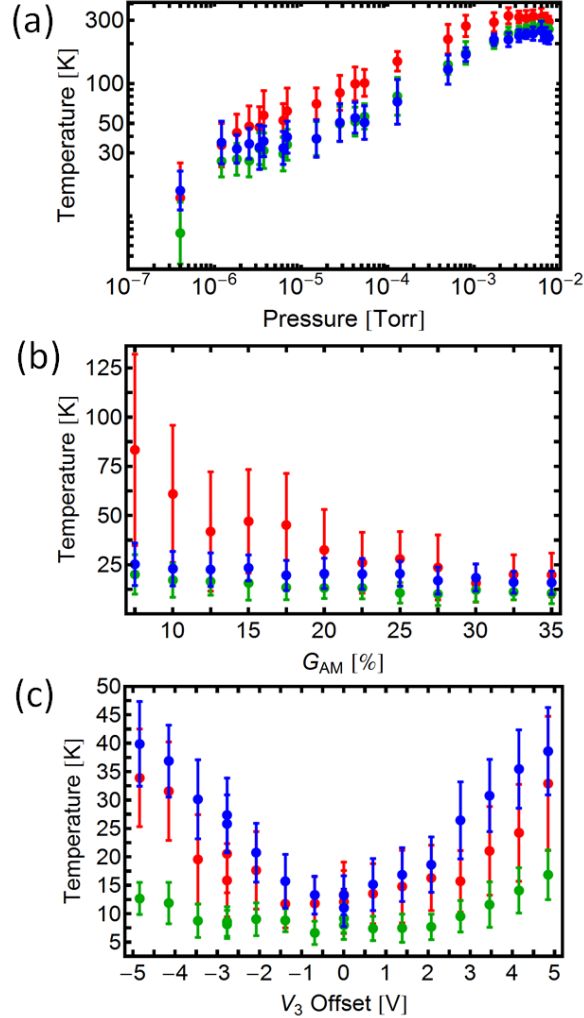


days scale as compared to trapping time of a few hours without the feedback. Flakes center of mass motion temperature was cooled below 20 K for all three degrees of freedom once the feedback is turned on and the pressure level goes below  $10^{-6}$  Torr (See Fig.1.3.a). To obtain this result, it was necessary to null stray DC electric fields. The fields nulling was done by changing voltages on a set of three auxiliary electrodes located near the trap. We have studied the dependence of cooling on various parame-

ters and observed that cooling is dependent on the feedback strength (See Fig.1.3.b).

### 1.3.2 Stray fields minimization

**Figure 1.3:** Dependence of cooling on pressure (a), feedback gain in AM % (b) and stray fields optimization done by varying auxiliary electrode's voltage (c)



The importance of the nulling of the DC stray electric fields, which are always present in the chamber [35], arises from the increase in sensitivity of the feedback to noise when there are non-zero DC fields acting on the particle. Since the stray (patch) potentials are hard to get rid of, we chose to minimize their effect by adding a set of

auxiliary electrodes to the trap. The electrodes were positioned around the trap and used to create compensating fields, where the amount of field was chosen to give the optimal cooling of the motion. We have systematically studied and showed that this nulling of the fields is necessary for our system as can be seen from figure 1.3.c.

The quantitative locating of the "sweet" spot in the electrodes settings was done by using a lock-in response to probe the sensitivity of the particle motion to an external perturbation. A fine tuning of the parameters was done in high vacuum conditions by measuring the particle temperature dependence on small variations in the DC settings. The resulting cooling stays close to initial value even a few days later, though the slow drift of stray fields was observed and an implementation of the feedback control of the auxiliary electrodes could be necessary for experiments that take more than a few days to conduct.

### 1.3.3 Particle characterization

Characterization of the particle in terms of absolute values of charge and mass was achieved by fitting the observed quantization of the discharge (Fig. 1.4.a). The calibration is based on the fact that eigenfrequency of motion is proportional to  $q/m$ , where  $q$  and  $m$  are total charge and mass of the flake. By calibrating frequency jumps in terms of minimum possible frequency jump ( $\delta q = \pm e$ ), we are able to extract the absolute mass and charge values. We also discuss some estimates on the size and shape of the particles we studied.

### 1.3.4 Preliminary data on precession

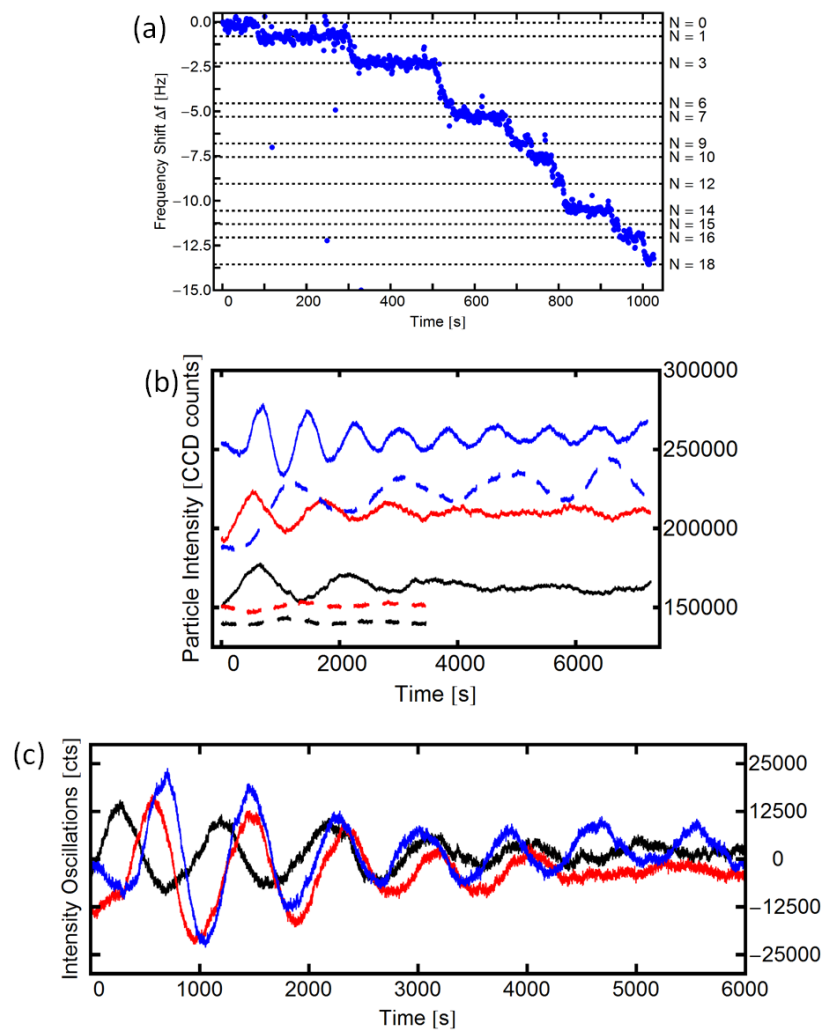
Finally, it was shown that a whole new world of transient dynamics is accessible for research if one learns how to control the particle spinning and its orientation. By setting the spinning of the flake via circularly polarized light, we collected the preliminary data on the precession and spinning reorientation under the influence of the DC stray fields. While this data is not enough to make a definite conclusion about the exact values of torque and force acting on the particle, the approach of combining the DC fields and circularly polarized lights to tune the orientation of the spinning axis looks as an interesting direction to follow.

## 1.4 Thesis outline

The rest of the thesis is organized as follows. Chapter 2 explains the concept of the quadrupole ion trap and presents the theory of its operation. Chapter 3 describes the overall experimental setup and its main components. Chapter 4 describes the parametric feedback concept, its theory and effect of noise on the achievable cooling temperature. Chapter 5 goes into deeper detail on operation of an Field Programmable Gate Array (FPGA), the core processing unit of the feedback scheme. In chapter 6, we present data on particle motion at low pressures, proof of cooling in the feedback regime and show how the cooling depends on various control parameters. Chapter 7 explains the procedure used for optimization of the particle cooling relative to patch fields as well as preliminary data on particle reorientation under the influence of DC stray fields. Particle characterization in terms of absolute mass and charge values are

written about in chapter 8, and conclusions and future work are discussed in the final chapter, chapter 9.

**Figure 1.4:** (a) Dependence of eigenfrequency along  $Z$  axis on time; (b) Dependence of average intensity of the particle on voltage settings and laser power level (dashed -  $245 \mu\text{W}$ , solid -  $145 \mu\text{W}$ ); (c) Precession of the particle intensity after the change in an auxiliary electrode setting at different values of electrode offsets.



### Ion trap theory and experiment

---

#### 2.1 Requirements on trapping potential

Idea of particle levitation was originally tested in 1913 by Millikan in his famous experiments. By studying levitated oil drops, he was able to find an electron charge with the highest accuracy available at the time [59]. But it was only in the mid-1950s, when research on confinement of high-energy particles led to realization that a properly configured electromagnetic fields are capable of trapping charged particles in a dynamic equilibrium [30]. This can sound counterintuitive due to the Earnshaw's theorem [60] on stability of charges' assembly.

Earnshaw's theorem, a well-known fact in electrodynamics, declares that even the smallest deviations of position of any of the charges placed in equilibrium will lead to collapse of the configuration. The logic behind such claim is based on Gauss' law (which in turn originates from the scalar nature of the electrostatic fields). Indeed,

since an electrostatic potential  $\Phi$  at a point with no charge adds up to  $\Delta\Phi = 0$ , it will provide a restriction on the electric forces  $F_{el}$  acting on the particle at any given point

$$\nabla \sum F_{el} = -\Delta\Phi = 0, \quad (2.1)$$

which in turn implies that any point of electrostatic equilibrium has to be a saddle point. This means that there is always at least one direction which has a negative force gradient leading to an escape route for a particle.

If we want a spring like force to act on the particle moving near the equilibrium point, the force dependence on distance  $F \sim r^{l-1}$  with  $l = 2$  or higher is required. Corresponding force is created, when the potential has a symmetry of  $2l$ , meaning that its general dependence on  $r$  and angles  $\theta$  and  $\phi$  can be written as:

$$\Phi \approx r^l \sum_m C_m P_l^m(\theta) e^{im\phi}, \quad (2.2)$$

where  $P_l^m(\theta)$  are Legendre polynomials and exact values of  $C_m$  are defined by the geometry of the trap in question. For most of the Paul trap designs, the lowest symmetry (quadrupole symmetry when  $2l = 4$ ) is used during the trap design [30, 61]. Higher symmetries are sometimes of interest, though the traps with symmetry higher than quadrupole (sextupole, octupole) provide weaker confinement force, when compared to quadrupole traps [62]. General form for a quadrupole potential can be written as:

$$\Phi = \frac{\alpha x^2 + \beta y^2 + \gamma z^2}{2z_0^2} \Phi_0, \quad (2.3)$$

where coefficients  $\alpha$ ,  $\beta$  and  $\gamma$  have a constraint defined by Gauss's law ( $\nabla\Phi = 0$ ):

$$\alpha + \beta + \gamma = 0, \tag{2.4}$$

and  $z_0$  is the scaling factor that depends on the exact geometry of the trap and serves as a characteristic length scale of the trap potential.

## 2.2 AC approach and equations of motion

### 2.2.1 Mechanical analogy

In order to understand how one can create a stable equilibrium configuration from an unstable one, let us compare the a quadrupole potential to a corresponding case in mechanics [63, 64]. Imagine that we place a small ball into a potential that has a saddle point configuration, similar to the potential experienced by the charged particle. Depending on which direction the ball is pushed in, it will either escape or return back to the center of saddle. But if we start to spin the saddle around its symmetry axis, the ball will start to experience an effective attractive potential [64]. If high enough frequency of rotation is chosen, the ball will become trapped in a spinning saddle and, as long the case of negligible mechanical friction is considered, it will stay there till the spinning of the saddle is stopped.

In a similar way, one can try to create a "spinning" of the DC trapping potential that will result in an effective attractive force in all directions. The procedure that corre-

sponds to spinning of the mechanical potential is the switching from the DC potential to the AC one:

$$\Phi_{\text{DC}} = \frac{\alpha x^2 + \beta y^2 + \gamma z^2}{2z_0^2} \Phi_0 \rightarrow \Phi_{\text{AC}} = \frac{\alpha x^2 + \beta y^2 + \gamma z^2}{2z_0^2} \Phi_0 \cos(\Omega t), \quad (2.5)$$

where  $\Omega$  is the frequency the trap potential is "spinning" with. While the exact solution for the mechanical saddle has a different quantitative dependence on variable parameters [30], it still serves as a nice model for getting an insight in how the Paul trap works.

### 2.2.2 Quasipotential approach

If we assume that particle stays close to the trap center, where the quadrupole expansion of the potential works well, the electrical force acting on the particle will be created by a potential  $\Phi(r)$ :

$$\Phi(r) = \Phi(x, y, z) = V_{\text{AC}} \cos(\Omega t) \frac{[\alpha x^2 + \beta y^2 + \gamma z^2]}{2z_0^2}, \quad (2.6)$$

leading to:

$$\vec{E}(r) = -\nabla\Phi(r) = \vec{E}_0(r) \cos(\Omega t) = -(\alpha x, \beta y, \gamma z) \frac{V_{\text{AC}}}{z_0^2} \cos(\Omega t). \quad (2.7)$$

In the simplest case of no damping and no other forces present, the equation of motion takes form of:

$$m\ddot{r} = q\vec{E}(r). \quad (2.8)$$

The most intuitive way to understand how the resulting motion looks like is to use the quasipotential approach. It is assumed that particle motion has two incommensurate harmonics with frequencies  $\Omega$  and  $\omega$  (value of  $\omega$  is derived below). This means that we are looking for a solution of the equation as a combination of fast changing part  $r_0$  and slowly changing part  $R$ :

$$r = (x, y, z) = R + r_0, \quad (2.9)$$

where we assume that  $r_0 \ll R$ . In this approximation the Eq. 2.8 can be rewritten as follows:

$$m\ddot{R} + m\ddot{r}_0 - q\vec{E}_0(R)\cos(\Omega t) - q\nabla\vec{E}_0(R) \cdot r_0 \cos(\Omega t) = 0. \quad (2.10)$$

By separating the parts of last equation into fast and slowly changing terms, we can write the equation for  $r_0$ :

$$m\ddot{r}_0 = q\vec{E}_0(R)\cos(\Omega t), \quad (2.11)$$

which has a solution

$$r_0(t) = -\frac{qE_0(R)}{m\Omega^2}\cos(\Omega t). \quad (2.12)$$

By substituting  $r_0$  into equation for slow component of the particle motion,  $R$ , we get:

$$m\ddot{R} + \frac{q^2\vec{E}_0(R)\nabla E_0(R)}{m\Omega^2}\cos^2(\Omega t) = 0. \quad (2.13)$$

By averaging equation 2.13 over timescale of  $1/\Omega$  (we are looking for much slower  $R(t)$  as a solution), we get a harmonic equation for the particle macromotion in a

quasipotential approach:

$$m\ddot{R} + \frac{q^2 [\nabla E_0(R)]^2}{2m\Omega^2} R = 0, \quad (2.14)$$

where the quasipotential, which the particle moves in, is equal to  $q^2 [\nabla E_0(R)]^2 / 2m\Omega^2$ .

The solution of such equation is given by  $R(t) = R_0 \cos(\omega t + \varphi)$  and can be derived in a similar way for the motion along axes  $Y$  and  $Z$ . By using the quadrupole nature of the trap potential, we can derive corresponding eigenfrequencies of motion:

$$\omega_{x,y,z} = \frac{q |\nabla_{x,y,z} E_0(R)|}{\sqrt{2}m\Omega} \quad (2.15)$$

as:

$$\omega_x = |\alpha| \frac{qV_{AC}}{\sqrt{2}m\Omega z_0^2}, \quad \omega_y = |\beta| \frac{qV_{AC}}{\sqrt{2}m\Omega z_0^2}, \quad \omega_z = |\gamma| \frac{qV_{AC}}{\sqrt{2}m\Omega z_0^2}, \quad (2.16)$$

where  $\omega_x + \omega_y = \omega_z$ .

Finally, the equations of motion can be written as:

$$\ddot{x} + \Gamma_x \dot{x} + \omega_z^2 x = 0 \quad (2.17)$$

$$\ddot{y} + \Gamma_y \dot{y} + \omega_z^2 y = 0 \quad (2.18)$$

$$\ddot{z} + \Gamma_z \dot{z} + \omega_z^2 z = 0, \quad (2.19)$$

where we have added the damping to the motion along each of axes, and damping ratios  $\Gamma_x, \Gamma_y, \Gamma_z$  are equal in the zero approximation and depend on gas pressure [13, 65].

The damping ratios could be different if non-thermal channels of anisotropic nature

are present.

We can check what conditions are required for validity of the quasipotential approach ( $r_0 \ll R$ ) by rewriting  $r_0$  in terms of  $R$ :

$$R \frac{q}{m} \frac{\alpha_{x,y,z}}{\Omega^2 z_0^2} \ll R, \quad (2.20)$$

that can in turn be rewritten in a simpler form:

$$\omega_{x,y,z} \ll \Omega. \quad (2.21)$$

This requirement is true for the particles we study, and it is interesting to note that the case of  $\omega \sim \Omega$  corresponds to the onset of instability, the conditions of which are described in the next section.

In the regime, where quasipotential approach is valid, the particle interaction with external fields and forces can be described by adding the corresponding terms to the harmonic potential equation, a fact that is heavily used in our discussion of DC fields effect on particle cooling (see Chapters 4 and Chapter 7).

### 2.2.3 Mathieu equations and exact solutions

While the quasipotential approach is useful for study of particle motion at trap parameters set to be far from values leading to instability of motion, one needs to use a more rigorous approach to get those values in the first place.

The derivation of the instability boundaries starts with writing down the equations

of motion of the particle in the AC quadrupole field:

$$\ddot{x} + [a_x - 2q_x \cos(2\tau)]x = 0 \quad (2.22)$$

$$\ddot{y} + [a_y - 2q_y \cos(2\tau)]y = 0 \quad (2.23)$$

$$\ddot{z} + [a_z - 2q_z \cos(2\tau)]z = 0 \quad (2.24)$$

where we wrote the equations of motion in the form typically used for this type of differential equations, which are called Mathieu equations [66]. The relationship between  $\tau$ ,  $a$ ,  $q$  and the trap parameters and time  $t$  is as follows:

$$\tau = \frac{\Omega t}{2} \quad (2.25)$$

$$a_x = -\alpha \frac{qV_{DC}}{z_0^2}; q_x = \alpha \frac{qV_{AC}}{2z_0^2} \quad (2.26)$$

$$a_y = -\beta \frac{qV_{DC}}{z_0^2}; q_y = \beta \frac{qV_{AC}}{2z_0^2} \quad (2.27)$$

$$a_z = -\gamma \frac{qV_{DC}}{z_0^2}; q_z = \gamma \frac{qV_{AC}}{2z_0^2} \quad (2.28)$$

Here, we have added a  $V_{DC}$  term to the equations to account for the case when an additional DC voltage is applied between the trap electrodes.

Due to Floquet theorem [67], the search of the solution can be limited to product of periodic function and the exponential term:

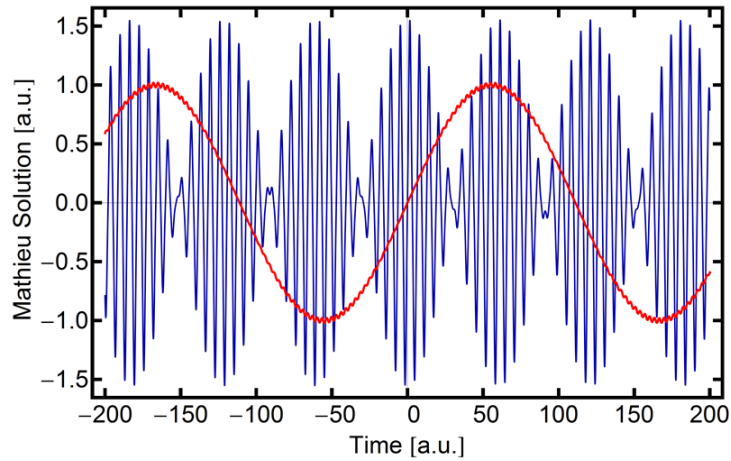
$$x = e^{\mu\tau} \left\{ \sum_n A_n \cos(n\tau) + B_n \sin(n\tau) \right\}, \quad (2.29)$$

where  $A_n$ ,  $B_n$  and  $\mu$  are found by substituting Eq. 2.29 into Eq. 2.22. By collecting the terms that have same  $n\tau$  dependence together, we can get a system of chain equations [68]:

$$\left[ a - (n - i\mu)^2 \right] A_n - q(A_{n-2} + A_{n+2}) = 0 \quad (2.30)$$

and similar looking equations for  $B_n$ . The resulting time dependence of the equation changes drastically based on the values of  $a$  and  $q$  (see Fig. 2.1, where solutions at different  $(a, q)$  settings are shown). This can be thought of as the result of weaker or stronger coupling between the harmonics of the solution, which depends on  $a$  and  $q$  (See Eq. 2.30).

**Figure 2.1:** Exact solution of Mathieu equation, when quasipotential approximation is valid (blue line;  $a = 0$  and  $q = 0.04$ ) and when there is no distinction between micro- and macro- motion (red line;  $a = 0$  and  $q = 0.905$ , where  $q$  is chosen to be close to instability boundary  $q_{crit} = 0.91$ )



We can rewrite equations 2.30 in form of matrix equation  $K(\mu) \cdot A = 0$ , where

$A = (\dots, A_{2n}, A_{2(n-1)}, A_{2(n-2)}, \dots)$  by introducing matrix  $K(\mu)$  [69]:

$$K(\mu) = \begin{bmatrix} \cdot & \cdot & \cdot & \cdot & \cdot & \cdot & \cdot \\ \cdot & -q & g_n & -q & 0 & 0 & \cdot \\ \cdot & 0 & -q & g_{n-1} & -q & 0 & \cdot \\ \cdot & 0 & 0 & -q & g_{n-2} & -q & \cdot \\ \cdot & 0 & 0 & 0 & -q & g_{n-3} & \cdot \\ \cdot & \cdot & \cdot & \cdot & \cdot & \cdot & \cdot \end{bmatrix}, \quad (2.31)$$

where  $g_n = a - (2n - i\mu)^2$ . Since we are looking for nontrivial solutions to the Mathieu equation, the determinant  $\Delta(\mu) = \det K(\mu)$  has to be equal to zero [69]:

$$\Delta(\mu) = 0. \quad (2.32)$$

Therefore the search for solution of the Mathieu equation is reduced to solving the infinite order equation, created by expanding the determinant. To avoid the issues that appear when trying to solve such equation, we can use properties of complex functions to write the solution  $\mu$  in terms of determinant  $\Delta(0) = \Delta(\mu = 0)$  [69]:

$$\mu = \frac{1}{\pi} [1 - \Delta(0)(1 - \cosh \pi \sqrt{a})]. \quad (2.33)$$

The last equation is useful for finding exact values of  $\mu$  numerically with any set accuracy, by substituting  $\Delta(0)$  with  $\Delta_N(0)$ , where  $\Delta_N(0)$  is the determinant of the submatrix of full matrix  $K$  with size  $N \times N$  and  $\Delta(\mu) = \lim \Delta_N(\mu)$ . The calculation can

be simplified further by using a relationship  $\gamma_n = q/g_n$  [69]:

$$\Delta_i = (1 - \gamma_i \gamma_{i-1}) \Delta_{i-1} - \gamma_i \gamma_{i-1} \Delta_{i-2} + \gamma_i \gamma_{i-1}^3 \gamma_{i-2}^2 \Delta_{i-3}. \quad (2.34)$$

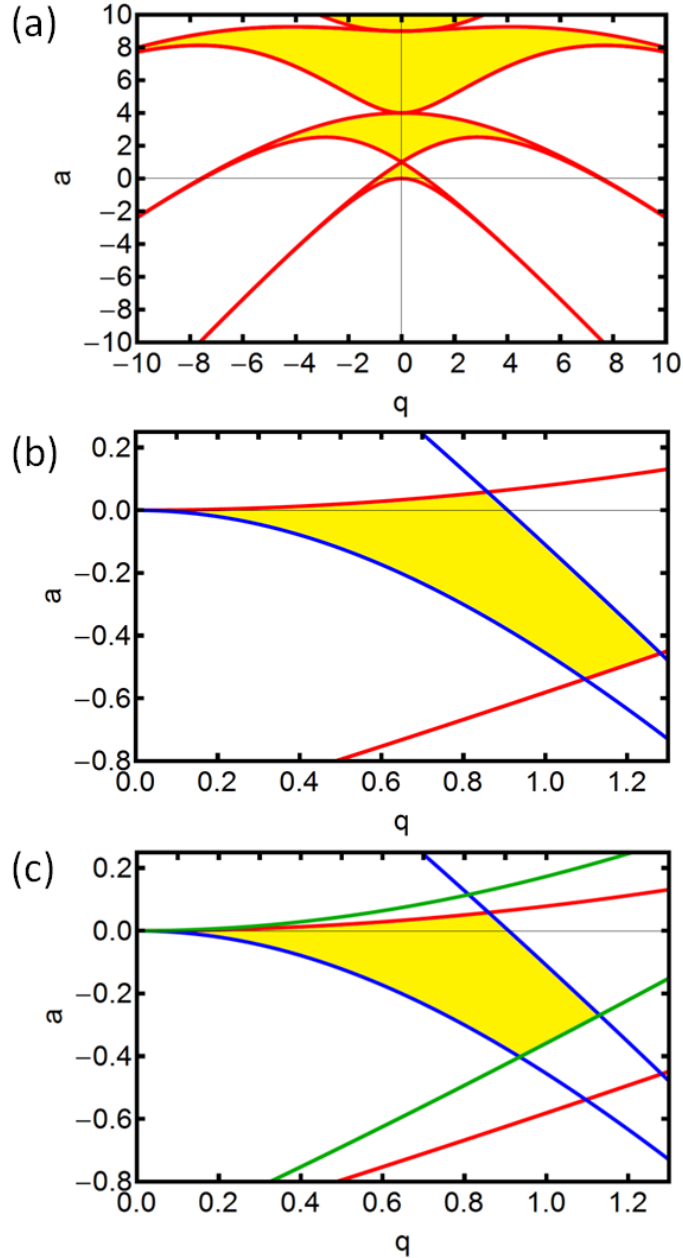
#### 2.2.4 Search for stability of the solution

Once the value of  $\mu$  is found, we can make a conclusion on whether a given  $(a, q)$  combination leads to stable trapping or not. The particle motion in the trap is stable, when  $\mu$  is a purely imaginary number (otherwise solution will diverge when  $t \rightarrow \infty$  or  $t \rightarrow -\infty$ ).

Instead of testing all values of  $a$  and  $q$ , we can locate all values that give characteristic curves (case of  $\mu = N$ , where  $N$  is integer). As it turns out, regions confined between characteristic curves with different  $N$  have either only stable or only unstable solutions and it is easy to map out all such regions in a consistent manner (typical distribution of stable (yellow-filled) and unstable regions is shown in Fig. 2.2.a).

Since the boundary conditions for stability we found set the stable motion in only one direction, the last step left is to use all three equations of motions to find the parameters leading to stable trapping in all directions. This can be done by plotting the stability regions for each of the axis of motion on the same plot, the feat that is achieved by stretching the plot given in the initial example by  $(\alpha, \alpha)$  for  $X$  (and by  $(\beta, \beta)$  and  $(\gamma, -\gamma)$  for  $Y$  and  $Z$  correspondingly). The resulting overlapping plots give the lowest parameters' region with stable solutions in all three directions to have a shape that is shown on Fig. 2.2.b. While there are other stable regions, they have much smaller areas than the region we showed in Fig. 2.2.b.

**Figure 2.2:** Stability (yellow-filled) regions for: (a) Mathieu Equation; (b) Quadrupole Ion trap with  $\alpha = \beta = -\gamma/2$  (three Mathieu equations); (c) Quadrupole Ion trap with  $\alpha = 1.5\beta = -2.5\gamma$ . Notice qualitative similarity to case (b).



### 2.2.5 Patch field gradients effect on eigenfrequencies

As previously mentioned (see Eq. 2.16), in the regime when quasipotential approach is valid, eigenfrequencies of motion along three main axes of the trap satisfy

$\omega_x + \omega_y = \omega_z$ . This is true only if the derivatives of DC fields are equal to zero near the trap center. In the opposite case, the motion of the particle near the trap center is modified:

$$m\ddot{\mathbf{R}} + \omega^2 \mathbf{R} - q \nabla \vec{E}_{DC}(\mathbf{R}) \cdot \mathbf{R} = 0. \quad (2.35)$$

If we search for the solution in form  $\mathbf{R} = (x_s, y_s, z_s) e^{i\omega_{dc}t}$ , we get a matrix equation:

$$\begin{bmatrix} m(\omega_x^2 - \omega_{dc}^2) - qE_{xx} & -qE_{yx} & -qE_{zx} \\ -qE_{xy} & m(\omega_y^2 - \omega_{dc}^2) - qE_{yy} & -qE_{zy} \\ -qE_{xz} & -qE_{yz} & m(\omega_z^2 - \omega_{dc}^2) - qE_{zz} \end{bmatrix} \begin{bmatrix} x_s \\ y_s \\ z_s \end{bmatrix} = 0, \quad (2.36)$$

where  $E_{xy}$  denotes  $x$ -derivative of DC field  $E_y$ ,  $E_{xx}$  denotes  $x$  derivative of DC field  $E_x$ , and so on. One can find an equation for eigenfrequencies  $\omega_{dc,x}$ ,  $\omega_{dc,y}$ ,  $\omega_{dc,z}$  in the presence of non-zero DC field gradients by setting to zero the gradient of matrix in equation 2.36. To lowest order in expansion in derivatives, the solution is:

$$\omega_{dc,x} \approx \omega_x + \frac{qE_{xx}}{2m\omega_x}, \quad \omega_{dc,y} \approx \omega_y + \frac{qE_{yy}}{2m\omega_y}, \quad \omega_{dc,z} \approx \omega_z + \frac{qE_{zz}}{2m\omega_z}. \quad (2.37)$$

It is clear that these new, modified frequencies are different from non-perturbed ones and, in general, do NOT satisfy  $\omega_{dc,x} + \omega_{dc,y} = \omega_{dc,z}$ . Corresponding motion becomes more complex as well, and deviates from motion along main axes  $X$ ,  $Y$  and  $Z$ . The amount of discrepancy between unperturbed calculations and calculations with field derivatives depends on the DC fields present in the experiment.

To estimate the deviation, we take eigenfrequencies of particle 101614A, which

had values of 283, 475 and 719 Hz for nominal directions of  $X$ ,  $Y$  and  $Z$ . For these numbers, the difference between  $\omega_x + \omega_y$  and  $\omega_z$  is about 2.7 %. This value is important to keep in mind, since this deviation affects the crosstalk between the degrees of motion, when parametric modulation, intentional or unintentional, is present in the system.

## 2.3 Paul trap geometries

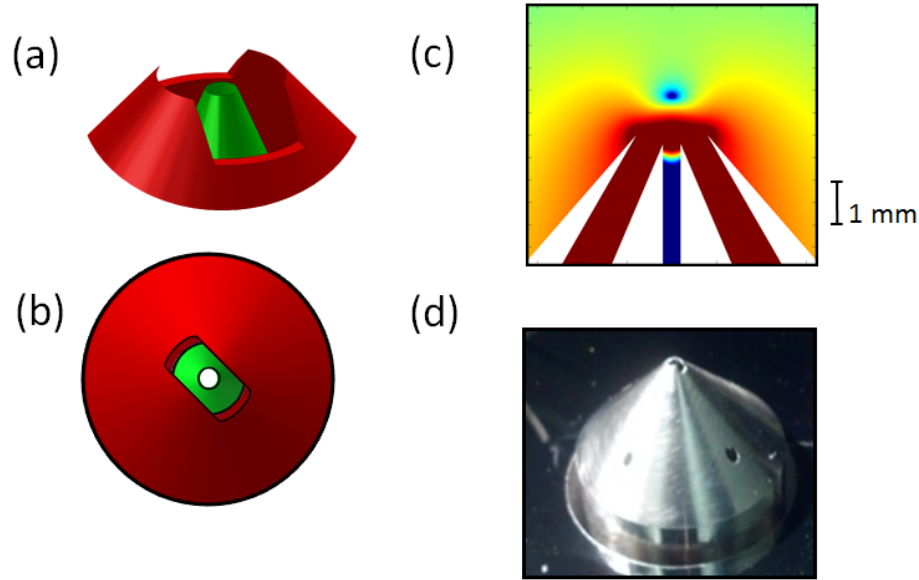
### 2.3.1 Hyperbolic shape

The basic shape of the trap that allows for a perfect quadrupole symmetry in all three dimensions was developed as a result of research on quadrupole mass spectrometry [70,71]. It can be thought of as a combination of three electrodes - two hyperbolic electrodes and one ring-like electrode, shapes chosen to give  $\alpha = \beta = -\gamma/2$ . The main disadvantage of this type of trap is an issue of accessing the trap volume, which becomes especially relevant, when study of such particles as ions is concerned. This is why linear [72,73] or planar traps [74,75] are usually used nowadays for quadrupole trapping of ions since they provide a high access solid angle.

### 2.3.2 Graphene trap

At the same time, another way to increase an access angle was proposed in an ion stylus trap design [32]. A range of potential applications, hard or impossible to conduct using a regular Paul trap design, were speculated for this type of trap, e.g. ion-based force sensor and ion entanglement experiments. Considering that solid access

**Figure 2.3:** Graphene Trap: (a) General view (outer electrode is shown in red and inner electrode in green); (b) View from above; (c) Potential distribution; (d) Photo of the currently used trap version.



angle close to  $4\pi$  (the paper quotes 96 % access area for one of the traps designed and tested in the experiment) was observed, the stylus trap looked like a perfect candidate for graphene trapping and manipulation experiments. Therefore, a similar design was developed and successfully tested in 2010 [56].

While 2010 trap satisfied most of the experimental requirements, it lacked large enough eigenfrequencies separation, one of the requirements for an efficient feedback cooling and resolution of particle motion. Thence, a new design with similar basic geometry of two coaxial electrodes (Fig.2.3.a) was implemented in 2014. The electrodes geometry is chosen to give a trap minimum position at  $z_0 = 2.19$  mm relative to the electrodes center, and the inner electrode of the trap has a through hole used for sending a circularly polarized laser beam. The use of the laser is necessary to stabilize particle spinning at low pressures, an issue which can not be easily solved

otherwise.

The key difference between the 2014 and 2010 trap designs is an additional symmetry breaking added via a slot in the outer electrode (see Fig.2.3.a). The slot is required due to the way we collect the data about the trapped particles : the light scattered from the particle is collected through a single lens and is processed after being split into two beams (providing signal to two photodetectors). Since we use only a pair of photodetectors, at least two degrees of motion ( $X$  and  $Y$  in our case) become hard to distinguish spatially. On the other hand, it is quite easy to distinguish particle motion along separate axes in frequency domain. The only requirement is their non-degeneracy, the effect that is created by the slot. It is easy to see that particle motion along the slot ( $X$ ) will have weaker confinement than the motion across the slot ( $Y$ ). While similar effect could be achieved via setting auxiliary electrodes voltages as was done in original paper about the ion stylus trap [32], the slot provides an easier degeneracy splitting that is large enough for our needs.

Another difference between the graphene trap and the regular Paul trap is the asymmetry of the graphene trap (two electrodes used instead of the original Paul trap with three electrodes) that leads to asymmetry of the trap potential (see Fig. 2.3.c). While higher terms in potential expansion (sextupole and octupole terms) can be neglected for our experiments, it is useful to figure out conditions which make it necessary to account for these terms. The trap can be thought about as purely quadrupole one, if the contribution of harmonic potential (quadrupole potential) is much larger

than from the anharmonic one (sextupole, octupole, etc.):

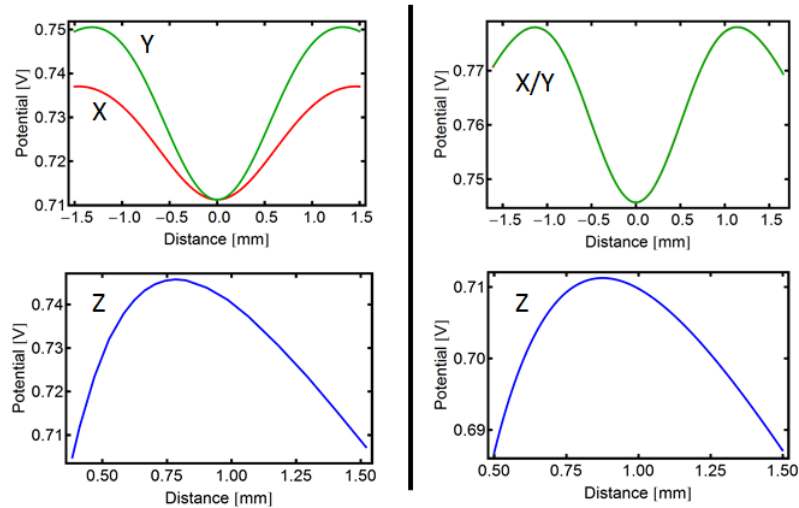
$$U_{\text{harmonic}}(x) \gg U_{\text{anharmonic}}. \quad (2.38)$$

If we consider two lowest terms in anharmonic potential, the restriction can be written as:

$$U_{\text{harmonic}}(x) = a_2 x^2 \gg U_{\text{anharmonic}}(x) = a_3 x^3 + a_4 x^4, \quad (2.39)$$

where  $a_2$ ,  $a_3$  and  $a_4$  are coefficients of quadrupole, sextupole and octupole corrections. Based on the trap geometry sextupole correction is going to be a limiting factor only for  $Z$  direction while  $X$  and  $Y$  will be dominated by octupole corrections. If we define a critical amplitude of motion as amplitude at which  $U_{\text{harmonic}} = U_{\text{anharmonic}}$ , we get  $A \ll A_{\text{crit},3} = a_2/a_3$  and  $A \ll A_{\text{crit},4} = \sqrt{a_2/a_4}$  for sextupole and quadrupole corrections correspondingly.

**Figure 2.4:** Trap potential dependence along  $X$  (red),  $Y$  (green) and  $Z$  (blue) trap axes for a trap with (left side) and without (right side) the slot.



The trap potential was simulated in a static field configuration by using SolidWorks software. In the simulation [76] both trap with and without slot were modeled and inner and outer electrode voltages were set to 0 V and 1 V correspondingly. By plotting squared gradient values of the field at each point, we get a quasipotential strength map (See Fig. 2.3.c), which shows a distinct minimum. In the vicinity of the minimum dependence of the potential on deviation from the center can be plotted (See Fig.2.4), and by fitting the plot curves to third order polynomials we can extract values of all the trap parameters (See Table 2.1).

**Table 2.1:** Trap parameters found from fitting potential near the trap minimum to the fourth order polynomial.

Parameter	X	Y	Z
$a_2(mm^{-2})$	0.039	0.070	- 0.109
$a_3(mm^{-3})$	0.00057	0.00090	0.12
$a_4(mm^{-4})$	-0.022	-0.043	-0.11
$A_{crit,3}(mm)$	68	78	0.92
$A_{crit,4}(mm)$	1.32	1.27	1.02

It can be seen from the table that all corrections to the quadrupole approximation can be neglected as long as particle motion is below  $\sim 1$  mm, the case that is true for our experiments.

Another interesting effect of the slot in the outer electrode of the trap is a quantitative change in the shape of the stability region (See Fig.2.2.c), based on changes in the stability regions for motion along  $X$ ,  $Y$  and  $Z$ . This leads to a situation, where one can have a stable solution along  $X$  with unstable motion along  $Y$  and vice versa (for a

totally symmetric trap,  $X$  and  $Y$  will become unstable/stable for the same parameter settings).

### 2.3.3 Duffing equation

Although, discussion of non-linear regime of particle motion goes beyond the scope of this thesis, the case when amplitudes of motion get close to critical ( $A \sim A_{crit}$ ) is very useful for study of various complex dynamics like motion phase-locking and hysteresis in the frequency response [20, 77, 78]. In the anharmonic regime the particle motion is no longer described by a harmonic equation, but rather by the Duffing equation:

$$\ddot{x} + \Gamma x + \omega^2 x + \kappa x^3 = 0, \quad (2.40)$$

where  $\kappa x^3$  is cubic correction to harmonic motion and defines the strength of anharmonicity of motion. Duffing equation is of interest since it is a basic example of how nonlinearity can create phenomena non-existent in linear regimes. This regime was previously observed and studied both for ions in a quadrupole trap [78–80] and for optically trapped nanoparticles [20]. Frequency pulling, motion synchronization and hysteresis of the response vs. frequency sweep direction were among the measured results and are of interest in various areas of research. Conducting similar measurements on the graphene flakes can be an interesting direction for a future research.

### 2.3.4 Typical operating parameters

As a reference of what typical values of the parameters discussed in this chapter look like experimentally, we present the numbers (See Table 2.1) used for trapping

and study of the motion of the flake 101614A. Flakes of similar charge to mass ratio were used during the development of the cooling scheme and when the reproducibility of trapping was studied.

**Table 2.2:** Trap operating parameters used for particle 101614A.

Parameter	Value
Trap voltage $V_{AC}$	300 V
Trap frequency $\Omega/2\pi$	12 kHz
Damping $\Gamma$ at 5 mTorr	10 Hz
Charge over mass ratio $q/m$	7 C/kg
Eigenfrequency $\omega_x/2\pi$	283 Hz
Eigenfrequency $\omega_y/2\pi$	475 Hz
Eigenfrequency $\omega_z/2\pi$	719 Hz

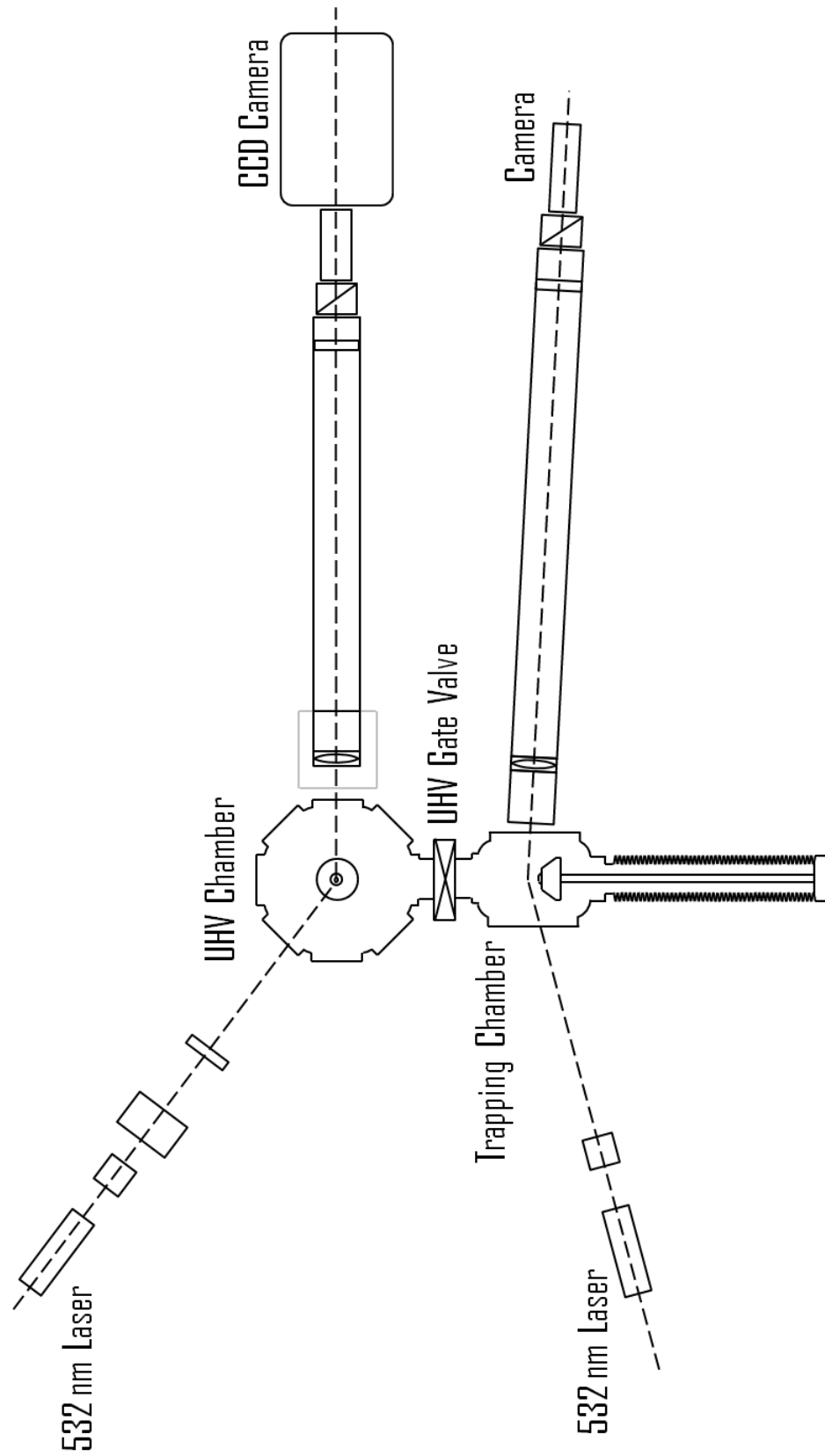
### Experimental setup

---

#### 3.1 Overall system

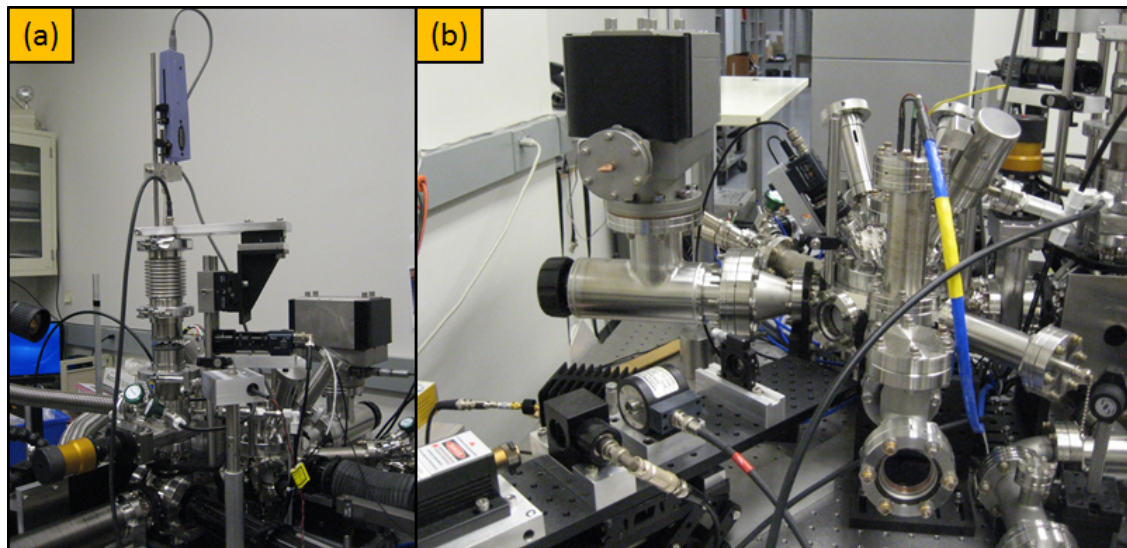
At the core level, our experimental setup (see Fig. 3.1 for an overall schematic) serves two main purposes. The first one is to introduce the particle into the system and second is to study it under high and ultra-high vacuum conditions. In order to separate these processes, we use two vacuum chambers (see Fig. 3.2 for images of back and front chambers) and transfer of the particles between the chambers is achieved by making one of the traps mobile. The main reason for using one chamber for particle trapping and a different one for experiments is to avoid contamination of an ultra-high vacuum (UHV) chamber with particulates and solution residue that are created during the particle trapping. Using separate chambers also allows us to speed up the throughput process by keeping a high vacuum environment separate and ready for future experiments during the trapping. This way, after the particle is trapped and

Figure 3.1: Overall view of the experimental setup as viewed from above.



transferred to the UHV chamber, the vacuum can be restored more quickly than in the case when one chamber is used for all the particle handling. The two-chamber

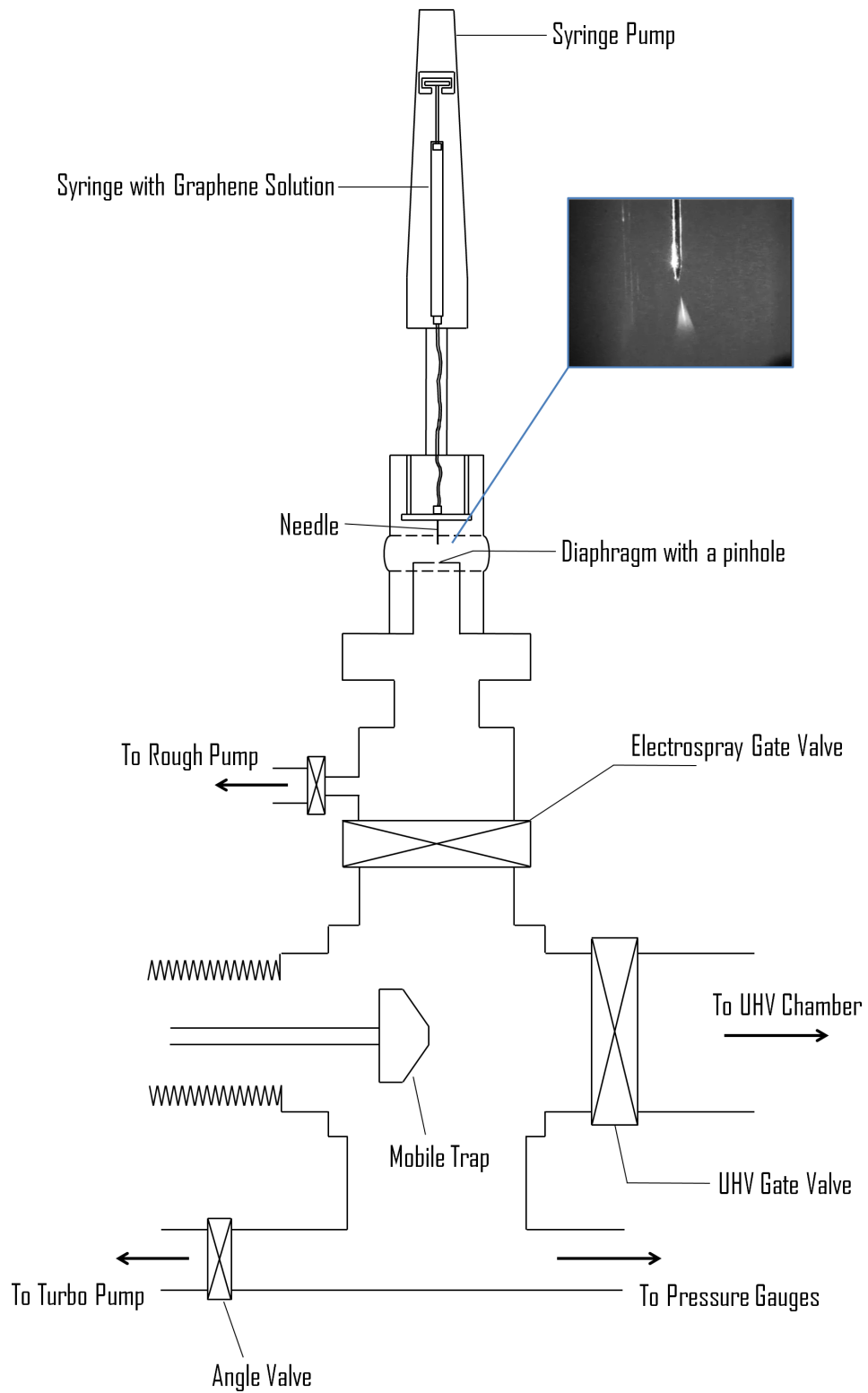
**Figure 3.2:** Images of front chamber with the electrospray setup on top of it (a) and back chamber (b).



system naturally leads to this chapter's structure, main sections of which are - particle generation and introduction into the system, description of the trapping chamber and corresponding apparatus, transfer from the trapping chamber to the high vacuum one, and finally, the description of the UHV chamber and corresponding electronics.

## 3.2 Particle introduction to the system

A consistent source of charged graphene flakes is created via an electrospray technique [81], where a graphene flake suspension is used as a particle source [82]. The suspension is made by mixing 5 mg of graphite powder with 5 mL of solution of water and isopropyl alcohol (IPA) (3:1 concentration). The procedure is done in the cleanroom environment to avoid unnecessary contamination. After the cleanroom prepa-

**Figure 3.3:** Electrospray scheme as viewed from the side.

ration, the vials containing the mixture are sonicated, and centrifuged afterwards at a speed of 3351 RPM for 30 minutes. The final liquid is close to transparent with a light gray coloring and an absorption length of 80-100  $\text{m}^{-1}$  [82]. The resulting suspension is loaded into the syringe pump (see Fig. 3.3) that infuses the liquid into the apparatus region above the transfer chamber via the metallic needle. The needle itself is held at a high DC voltage, set in the range of 2300-3000 V, generated by Keithley 247 high voltage supply. Both positive and negative polarity setting can be experimentally chosen, but for the consistency purpose we chose the positive sign and used only that polarity for the trapping. The electro spray plume has a cone-like shape (see inset in Fig. 3.3) and consists of charged micro-droplets, which are a mix of IPA and graphene flakes. The IPA evaporates during the micro-droplets' fall, leaving us with the falling charged graphene nanoplatelets.

The electro spray setup is connected to the chamber through the gate valve and a metallic diaphragm (see Fig. 3.3). The diaphragm held at the ground potential has a small pinhole with a diameter of 25  $\mu\text{m}$  and serves as a counter-electrode to the needle and as a way to guide and filter the droplets that are entering the system. The pressure above the diaphragm is held at about 1 atm nitrogen pressure. The pressure in the trapping chamber itself is in the region 250-300 mTorr and is achieved by opening the valve to the roughening pump that is used only during the electro spray operation. This pressure level was chosen to provide high enough damping for particles during their fall, which leads to higher trapping rate of the falling graphene flakes. The electro spray gate valve between the upper part and the trapping chamber is open only during the electro spray operation.

It is important to note that two issues with the pinhole in a diaphragm were observed during the experiments. The first one is its high contamination rate that results in the pinhole getting clogged by graphite residue. This results in slowing down of the experiment till the clogged pinhole is properly cleaned by sonication in the IPA. Even worse, it was found that after some time of operation, switching to a new diaphragm is necessary, which could be related to incomplete unclogging of the diaphragm during the sonication. The second issue is the orientation of the pinhole in the diaphragm relative to the axis between the needle and the trap, which was found to drastically affect the trapping rate of the flakes. This issue was recently addressed by modification of the system, which was done by Joyce Coppock and consisted of adding an X/Y/Z positioning setup for the needle [76].

The particles trapped during the experiments had a high variance in the properties, making the trapping of each particle a challenging and complex process (closer to art than science). Typical trapping protocol involved varying the needle voltage, the flow rate, and trap frequency till the particle was trapped. Parameters for trapping changed from a suspension to suspension, varying depending on the cleanliness of the needle and the needle position. In a similar way, the trapped particles showed large charge over mass ratio ( $10\text{-}100 \text{ C} \cdot \text{kg}^{-1}$ ) and brightness variations. We suspect that main culprit is the wide distribution of the flakes in size and shape after the sonication. Indeed, by using a simple model of a flake as a disk with radius  $a$  and thickness  $c \ll a$ , we can see that particles charged to the same voltage  $V$  will have a charge and mass

equal to [83]:

$$q = V \frac{4\pi\sqrt{a^2 - c^2}}{a \tan^{-1} \sqrt{\frac{a^2 - c^2}{c^2}}}, m = \rho\pi a^2 c \quad (3.1)$$

resulting in charge over mass ratio  $q/m$  that is strongly affected by the flake shape:

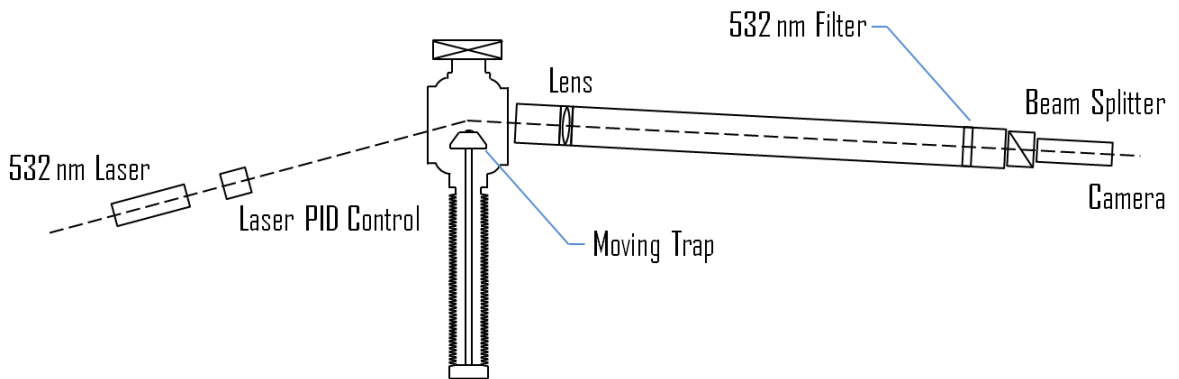
$$\frac{q}{m} \sim \frac{1}{ac}, \quad (3.2)$$

which would explain the spread in the observed charge over mass ratios.

Therefore, the particle quality is an issue to be addressed in the future, when and if the particle trapping becomes a limiting factor in the experiments. Ways to solve this problem include using a commercially prepared flake powder for the solution preparation. The resulting consistency in the particles shape and size will help to know what values to aim for, which in turn would narrow the parameter space to tune the trap in.

### 3.3 Front chamber and particle detection

**Figure 3.4:** General view of the *FRONT* chamber (as viewed from above) and corresponding optical setup.



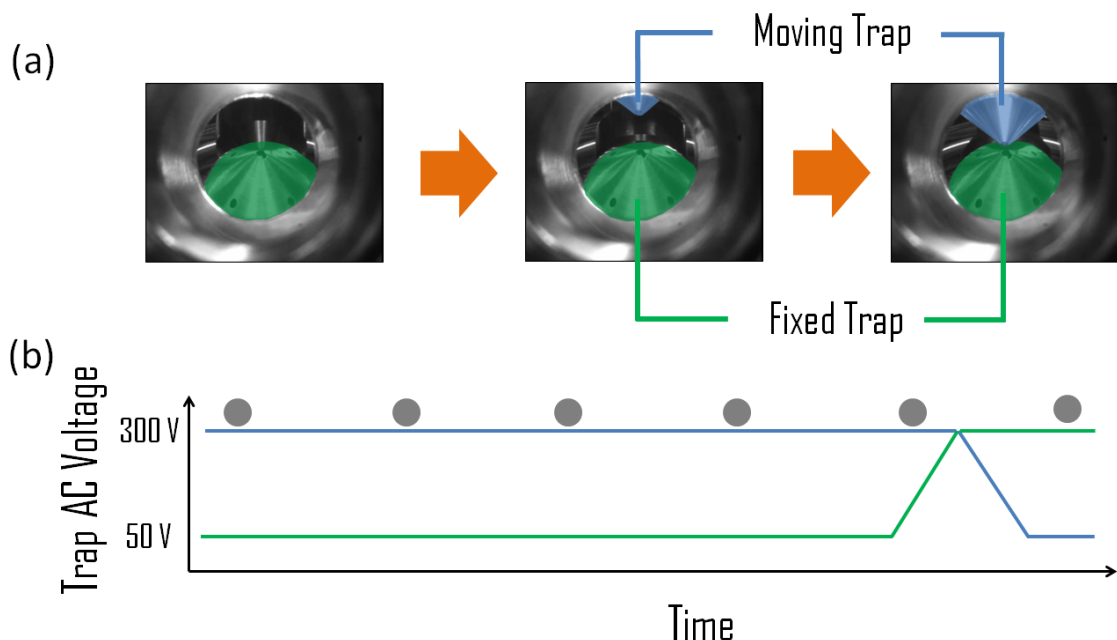
After the particle is introduced into the trapping chamber, we rely on optical detection to track whether it becomes trapped or not. The optical signal comes from the 532 nm laser beam with a beam width of about 0.16 mm that is scattered from the particle. The scattered light is collected using the lens set outside of the chamber at a distance of 12.5 cm. The light is split by 50:50 beam splitter, with split beams focused at the photcounter (not used in our experiments) and the detection camera, both at the lens focal distance of 75 cm.

Since the solution used in the experiments generated a wide distribution of particles in charge to mass ratio and brightness, the camera was also used to tune the electrospray settings by checking how many particles were detected by the camera and how much time they have spent in the detectable region. The settings that provided a visible flow of about 10-20 particles per minute (as detected via the camera) at the flow rate of 2  $\mu\text{L}/\text{minute}$  were considered optimal. At the optimal settings, we chose to wait for 5-10 minutes and if no successful trapping was detected, parameters (needle voltage, trap frequency, electrospray flow rate or inner trap electrode voltage) were tuned and improvement in trapping was checked for at new conditions. As a final measure, if no particles were getting trapped within one or two hours, we either cleaned up the pinhole and/or the electrospray needle, repositioned the needle relative to the trap, or changed a graphene solution.

### 3.4 Particle transfer

After the particle is successfully trapped, its transfer from the trapping chamber to the UHV chamber is required. First, the electrospray is turned off, the electrospray

**Figure 3.5:** (a) View of the UHV chamber as viewed through one of the chamber windows. Motion of two traps (color coded for convenience) relative to each other can be seen. (b) Schematic protocol of transferring particle from one trap to another. Gray disk represents the particle and serves as a visual guidance showing which trap particle is in.



gate valve is closed, and the gate valve leading to the UHV chamber is open (see Fig. 3.1 for the UHV valve). Then, the trap with particle, the mobile trap, is moved towards the fixed trap, located at the center of the UHV chamber, via the motorized motion of the rod (See Fig. 3.5.a). When the traps are at a distance of about 1.3 mm between the center axis of one trap and the terminal circumference of the electrodes of the other trap, AC voltages at the traps are varied in a way that leads to transfer of the particle from the moving trap to the fixed one (basic idea behind voltage change is shown schematically in Fig. 3.5.b). This is followed by retracting the mobile trap from the UHV chamber, and the UHV gate valve can be closed, sealing the UHV chamber off, with following pumping down to ultra-high vacuum (pressures below  $10^{-9}$  Torr) with

the ion pump. Otherwise, the turbo pump connected to the trapping chamber (see Fig. 3.3) can be used to pump down the trapping chamber and the connected to it UHV chamber to high vacuum pressures of about  $4 \cdot 10^{-7}$  Torr. The time needed for reaching high vacuum ranges between a day and a few hours. The latter case is true, when an exposure of the UHV chamber to any contamination is minimized by keeping the UHV gate valve closed all the time except for the particle transfer.

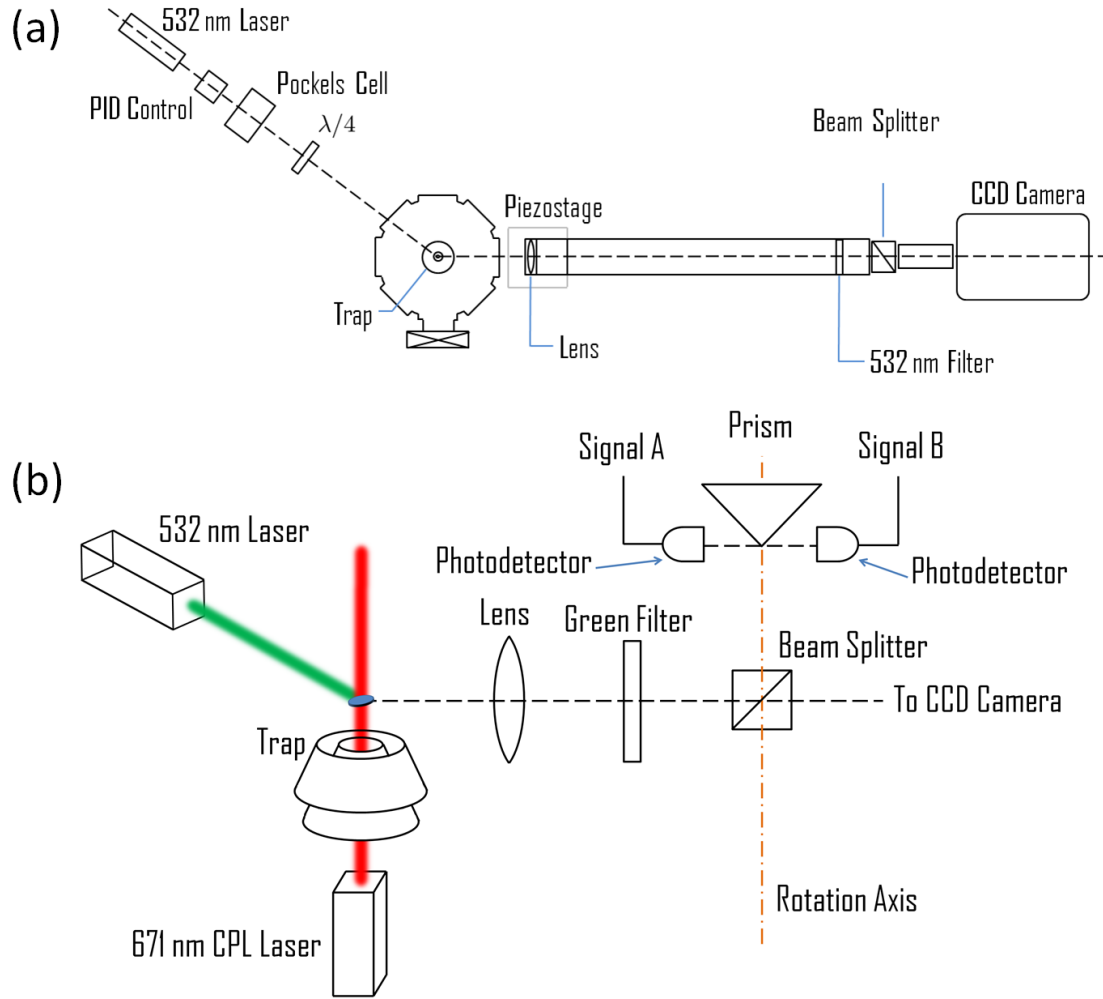
## 3.5 Back chamber and particle detection

Once the particle is in the back chamber (UHV chamber), it can be studied in more detail and most of the data we present in this thesis was taken in that chamber.

### 3.5.1 Signal detection

The laser setup used for illuminating the particle in the UHV chamber consists of a linearly polarized 532 nm laser with a beam waist of 0.16 mm at the trap center (see Fig. 3.6.a) and an additional circularly polarized (CPL) 671 nm laser beam, which goes through the trap center parallel to the  $Z$  axis (see Fig. 3.6.b) and is used to stabilize a flake spinning during the high vacuum experiments. Before illuminating the particle, the 532 nm laser passes through a Pockels cell (not used in our experiments) and a quarter-wave plate setting the linearly polarized light orientation along the experimental setup plane. The light scattered from the particle is collected by a lens with the diameter of 37 mm, which is located outside the UHV chamber at 12.5 cm distance from the center of the trap. The distance and the size of the lens give us the collection angle of about  $0.05 \times 4\pi$ . The focused light is filtered by 532 nm filter and

**Figure 3.6:** (a) General view of the *BACK* chamber as viewed from above and corresponding optical setup; (b) Pseudo-3D schematic of the optical setup is shown, including the relative orientation of 532 nm laser, 671 nm laser and the prism setup (prism + two photodetectors). Rotation axis denotes the axis around which the prism setup can be rotated.



is split by a 50:50 beam splitter afterwards. This setup gives a diffraction limit of

$$l = \frac{\lambda f}{2D} = \frac{532 \text{ nm} \cdot 125 \text{ mm}}{2 \cdot 37 \text{ mm}} \approx 900 \text{ nm} \quad (3.3)$$

for the smallest flake size distinguishable by the optics.

The first of the split beams is imaged by the charge-coupled device (CCD) camera

Pro-EM 512 with a pixel matrix of 512 x 512 (pixel size  $16\mu \times 16\mu$ ), which is located at a distance of 75 cm from the lens, giving the magnification factor  $M = 75/12.5 = 6$ . The signal collected by this camera provides information about the particle intensity (its value and variance) and position of its image relative to the camera. The speed of camera is set at 0.25-1 sec per frame, giving us the signal averaged over the flake vibrations and spinning (typical speeds are on the order of kHz in mTorr pressure range and reach a few MHz at  $\mu$ Torr pressures [56]). The data from the CCD camera is used to trace slow processes like precession and flake reorientation, which were observed at high vacuum conditions (see Chapter 7 for more detail).

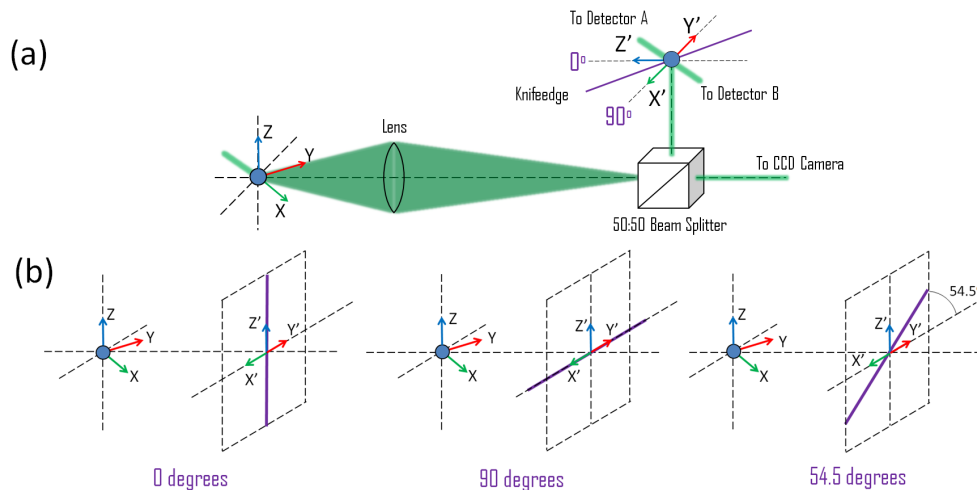
### 3.5.2 Knifeedge prism beam splitter

The second beam is focused on the knifeedge of the prism beam splitter, which guides the signal into the pair of two MPPC (multi-pixel photon counter) Hamamatsu photodetectors with nominal gain of  $2.39 \times 10^6$  electrons/photon (see Fig. 3.6.b). The focusing lens is setup on the piezo-stage with piezovoltage feedback controlled by an FPGA (see Chapter 5 for detail) to keep an average position of the image focused at the knifeedge. The settings of an FPGA control are chosen to provide a piezovoltage that makes contributions from both of the photodetectors equal up to the calibration coefficient. The scaling of photodetectors response is necessary due to the experimental difference between their saturation levels. The speed of feedback (4.4 Hz) is chosen to make average position of the particle image centered on the knifeedge while still keeping the signal from the particle oscillations in the trap. In this setup, the difference of signals between the photodetectors is proportional to the motion of

the particle, and the slow feedback to the piezovoltages cancels out the thermal drift of the lens relative to the chamber.

The configuration with two photodetectors is the simplest version necessary for detection of all three degrees of motion. This can sound counterintuitive, since we claim to be able to detect three degrees of freedom by measuring two signals (signal A and signal B). In fact, our ability to do this relies on frequency separation of major modes of the particle motion in the trap that is created intentionally as discussed in Chapter 2. The only requirement left is to make sure that all modes of motion produce a non-zero contribution to the signal measured by photodetectors. To make sure that each degree of freedom is equally represented, the whole prism setup, consisting of prism and both photodetectors, which are always set to be orthogonal to the prism knifeedge, is set on a rotating frame. The rotating axis is set to be parallel to  $Z$  axis of the trap and, as can be seen from Fig. 3.6.b and Fig. 3.7.a, leads to the change of projections of the particle motion measured by the photodetectors. Indeed, by looking

**Figure 3.7:** (a) Schematic description of particle motion detection with a help of a prism knifeedge beam splitter; (b) Projection of particle motion in case of the knifeedge orientation at 0, 90 and 54.5 degrees



at Fig 3.7.a, we can realize that by rotating the prism setup by an angle  $\varphi_{prism}$ , the signal from a particle displacement  $(X, Y, Z)$  measured by the photodetectors will be proportional to  $(X', Y', Z')$ , where:

$$X' = X \cos \varphi_{slot} \sin \varphi_{prism} \quad (3.4)$$

$$Y' = Y \sin \varphi_{slot} \sin \varphi_{prism} \quad (3.5)$$

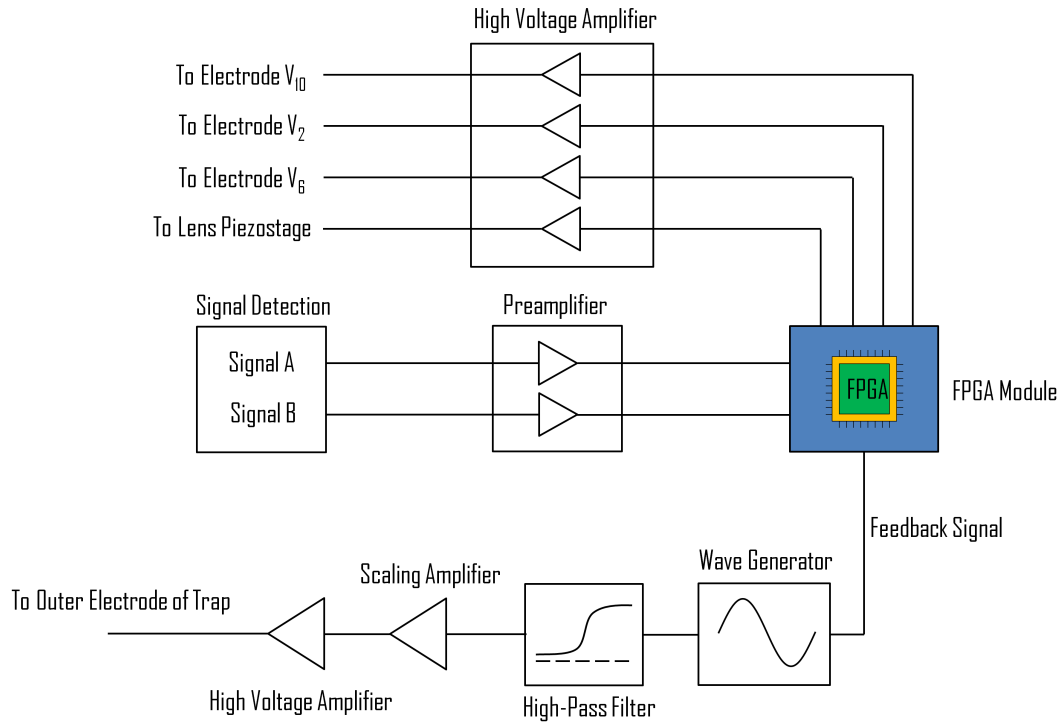
$$Z' = Z \cos \varphi_{prism}. \quad (3.6)$$

Here, we have accounted for the fact that the slot in the trap is chosen to be oriented parallel to the 532 nm laser and is at  $\varphi_{slot}$ , which in turn makes the angle between  $X$  and  $Y$  axes of the trap and the focal plane of the prism setup equal to  $\varphi_{slot} = 45^\circ$ .

Therefore, if we want same scaling of a signal from each of the trap axes, or in other words to have  $X' = Y' = Z'$  when  $X = Y = Z$ , the angle  $\varphi$  has to satisfy:

$$\cos \varphi = \frac{\sqrt{2}}{2} \sin \varphi \rightarrow \tan \varphi = \sqrt{2} \rightarrow \varphi = 54.7^\circ. \quad (3.7)$$

This angle of prism orientation was used for all the experiments discussed in this thesis. To note, if particle motion calibration via lens displacement is required (procedure that was not used in our experiments due to its low accuracy), it is better to set the rotation angle to either 0 or 90 degrees to make some of the particle projections zero.

**Figure 3.8:** Electronics Scheme.

## 3.6 Electronics

The optical signals, signal *A* and signal *B*, created by photodetectors, are what all of our data processing is based on. But before they are saved or used for feedback generation, the signals *A* and *B* (see "Signal Detection" box in Fig. 3.8) are amplified by a preamplifier, which consists of fixed gain  $G = 10^6 \text{V/A}$  current-to-voltage converter and a variable gain amplifier whose gain can be changed in the powers of 10, from 1 to 1000. Amplified signals are used as inputs of a field-programmable gate array (FPGA) module, where the signal is digitally filtered and the feedback is generated (see Chapter 5 for the FPGA discussion). Here, we only mention that the FPGA module produces five output signals. Three of them are constant tunable DC voltages that are amplified via RHK600 high voltage amplifier (HVA) to provide voltages to the set of

auxiliary electrodes (see below).

Two other signals are used for the feedback control, with the first one required for cancelling out the thermal motion of the lens. This signal is applied to the lens piezovoltage [voltage range 0-70 V max] after passing through the RHK amplifier. The final, fifth of the signals created by the FPGA module, is the most important signal - the parametric feedback signal, which is used for the motion cooling. The feedback loop is closed by feeding this signal as an amplitude (AM) or frequency (FM) modulation to the wave generator HP-33522A, which is usually set to operate in the range of 10-40 kHz and at the output voltage of  $5.42V_{pp}$ . The amount of modulation  $G_{AM}$  was tuned between 0 and 35 %, with values higher than 35 % found to lead to a decrease of the feedback efficiency. For experiments discussed in this thesis only AM modulation was used, but we have previously tested and checked that the feedback scheme works in the FM regime as well. Only advantage of AM over FM is the linearity of the trap modulation in the AM case, which can be seen from Eq. 2.16, where  $V_{AC}$  is modulated in the AM settings and  $\Omega$  is varied for the FM.

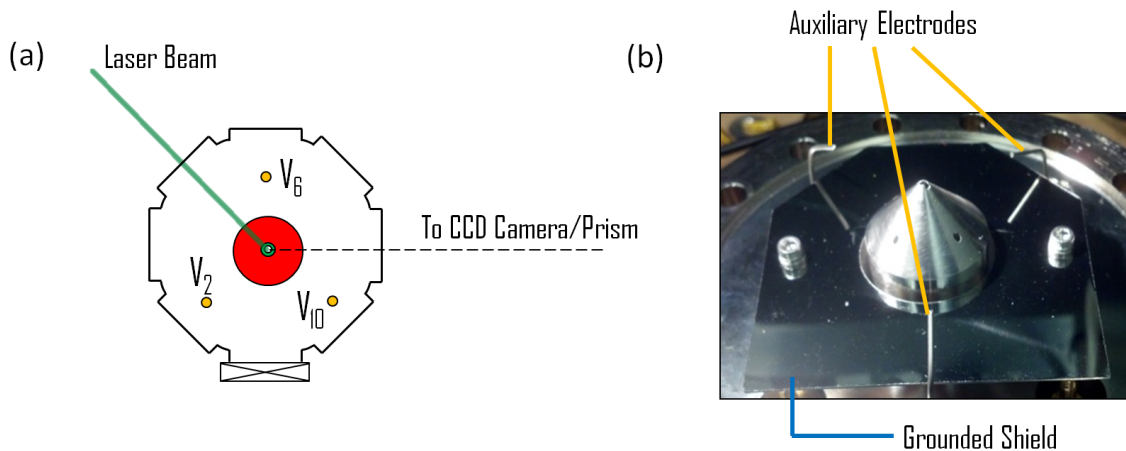
The output of the wave generator is passed through the high-pass filter SIM-965 set to cut-off frequency of 1000 Hz. The frequency was chosen to avoid affecting the trap operation, which has a much larger oscillation frequency, while at the same time limiting the contribution from the low-frequency noise of the wave generator. That contribution was found to be present when AM/FM operation was selected and a modulation level greater than zero was chosen. Since we have found that the noise level was independent of the input signal used for modulation, the conclusion that the noise is created by the wave generator itself was reached and the high-pass filter was

installed.

The filtered signal is amplified by the scaling amplifier SIM-983, whose main purpose is to vary voltage at the trap during the transfer. The settings of the scaling amplifier are kept the same in all other situations. Finally, the scaled signal is connected to an input of the high voltage amplifier A-250 with a fixed gain and the output signal of the amplifier is connected to the outer electrode of the trap. Setting scaling amplifier to gain 3.00 and output peak-to-peak amplitude of the wave generator to  $5.42 V_{pp}$  gives an output of 300 AC V, the trap voltage used for all experiments.

### 3.7 Auxiliary electrodes

**Figure 3.9:** (a) View from above of the relative position of auxiliary electrodes and the particle trap (b) Photo of the trap showing the auxiliary electrodes. The grounded shield, shown in the photo, is used for minimizing the interaction between the wiring and residual charge voltages and the particle motion in the trap.



An additional control over the particle is exercised via a set of three auxiliary electrodes installed close to the trap (labeled after the clock directions as  $V_{10}$ ,  $V_6$  and  $V_2$  on Fig. 3.9.a). The electrodes are set at an angle about 120 degrees between each other

and the distance between the trap and the electrodes is about 2 cm (see Fig. 3.9.b). The voltages on electrodes are set individually by three outputs of RHK High Voltage Amplifier (HVA) and are limited to the range of  $\{-35,35\}$  V (input voltages of  $\{-10,10\}$  V multiplied by gain of 3.5) for cable connections used during the experiments. Higher range of  $\{-450,450\}$  V is achievable, if the voltage cables are connected to higher gain of 45. The input voltages going to the HVA are generated using via an FPGA module (See Fig. 3.8), and are controlled via LabView program running on the host computer.

Here, we only mention that voltage settings of the auxiliary electrodes are chosen depending on the experiment conducted, and describe the criteria for choosing their exact values in Chapter 7, where the dependence of motion cooling on the patch electric fields is observed and studied.

### Parametric feedback : theory and limitation by noise

---

#### 4.1 Parametric feedback principle

To understand the concept of the parametric feedback scheme used in our experiment, let us start by considering the motion of the particle in the harmonic well with a variable well stiffness  $c(t)$ :

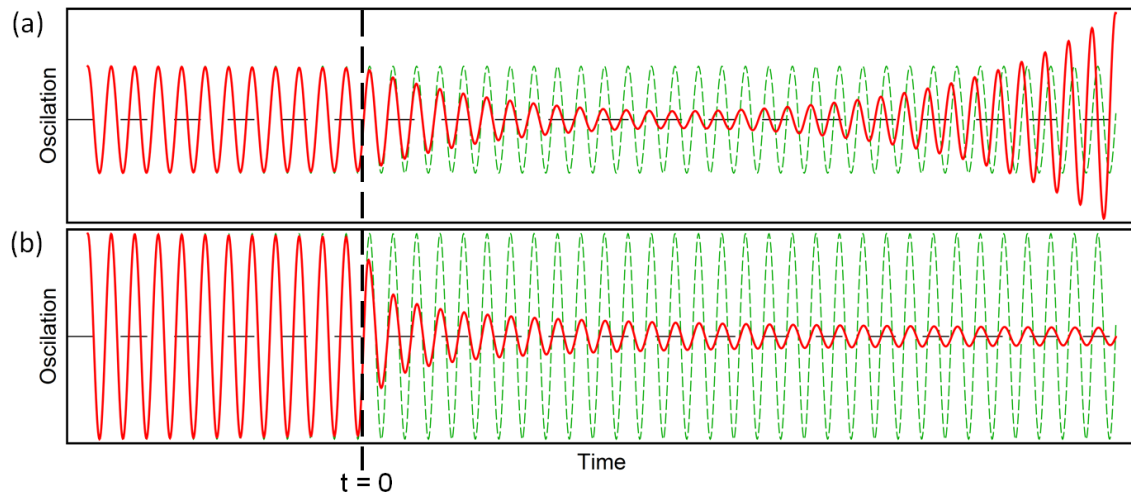
$$\ddot{x} + \Gamma\dot{x} + c(t)x = 0, \quad (4.1)$$

where the case of  $c(t) = \omega^2$  corresponds to regular harmonic oscillator, with particle motion being the sine wave of frequency  $\omega$ .

If  $c(t) = (\omega + \delta\omega \sin(\omega_1 t + \phi_0))^2$  is chosen as a modulation of the trap, the particle motion is parametrically driven and the solution of the equation can be represented in the Floquet form, in a way similar to the Mathieu equations of the trap (see Chapter

2). The case of  $\omega_1 = 2\omega$  is specifically interesting, since it corresponds to the most efficient pumping of the energy into or out of the particle motion, depending on the relative sign of  $\phi_0$ . If  $\phi_0 = \pi$  is chosen and the modulation is turned on at the time  $t = 0$  (see Fig. 4.1.a), we can clearly see that particle motion becomes dampened at first and then changes sign (phase-locks) to the modulation, settling to a divergent behavior. Existence of the transient period, where the particle motion is dampened,

**Figure 4.1:** Transition of the particle motion, when parametric modulation at twice the frequency is turned on (a) and when the feedback modulation is turned on (b)



is the basis for the parametric feedback scheme we chose to use. By making sure that phase difference  $\phi_0$  always stays equal to  $\pi$ , we can constrain the flake motion. The only question left is how to make sure that the trap modulation has the proper phase difference and is generated at twice the frequency of motion we try to dampen (active feedback).

Since the flake motion in our system is sinusoidal, the generation and the sign can be set by multiplying a signal (sine wave) by its derivative (sine wave shifted by  $\pi$ )

to give the proper frequency dependence and the phase. Result of adding this kind of modulation to the potential is shown in Fig. 4.1.b. It can be seen that there is no divergence of the motion, when compared to Fig. 4.1.a, and motion keeps its initial phase (no phase locking) as expected.

#### 4.1.1 Parametric feedback effect on damping

In our system, the parametric feedback is digitally generated by the FPGA module, and the resulting signal is used as an input of a wave generator set to an amplitude modulation (AM) mode. This means that the trap frequency (see Eq. 2.16) dependence on time can be written as:

$$\omega = \omega_0 + \omega_{FB}(t), \quad (4.2)$$

where

$$\omega_{FB}(t) = gS\dot{S}. \quad (4.3)$$

Here,  $g$  is the scaling coefficient that describes the strength of the feedback and is equal to a product of internal FPGA gain and AM modulation setting of the wave generator,  $S$  is the motion signal as generated from photodetectors.

Since the signal  $S$  contains information about motion along all three trap axes, it is necessary to discuss an issue of the possible cross-talk between those components (along the  $X$ ,  $Y$  and  $Z$  axes). As the feedback is proportional to the signal and its derivative (Eq. 4.3), the feedback will contain components that are given by all possible combinations of  $\omega_{x,y,z} + \dot{\omega}_{x,y,z}$ . If any of those combinations add up to an

eigenfrequency  $\omega_{x,y,z}$  or twice the eigenfrequency, an issue of cross-talk will need to be addressed. And while for the ideal quadrupole trap  $\omega_x \pm \omega_y = \omega_z$ , our typical operating conditions lead to  $\omega_x + \omega_y \neq \omega_z$ , which is most likely related to the second derivatives of the stray potential near the trap center (See Section 2.2.5). Other cross-talk terms such as degeneracy between  $2\omega_x$  and  $\omega_y$ ,  $2\omega_x$  and  $\omega_z$  and so on are not the case for the data discussed in this thesis, but should be kept in mind, when trying to cool the particle motion.

Therefore, the cross-term contributions to the feedback between three degrees of motion are considered to be negligible, and equations of motion can be thought of as three independent equations. To be concise, we consider the equation of motion along  $X$  axis, but the same formalism can be used for two other axes. In the presence of the feedback, the equation 2.17 is modified:

$$\ddot{x} + \Gamma\dot{x} + (\omega_0 + \omega_1)^2 x = 0. \quad (4.4)$$

Since  $\omega_1 \ll \omega_0$  for all of our experiments, the last equation can be simplified:

$$\ddot{x} + \Gamma\dot{x} + (\omega_0^2 + 2\omega_0\omega_1)x = 0 \rightarrow \ddot{x} + (\Gamma + 2gS_x^2\omega_0x^2)\dot{x} + \omega_0^2x = 0, \quad (4.5)$$

where  $S_x$  is the sensitivity of the feedback signal  $S$  to motion along  $x$ . Rewriting equation in this form shows that the effect of non-zero feedback ( $g > 0$ ) can be described

as change in the position dependence of the damping:

$$\Gamma_g(x) = \Gamma + 2gS_x^2\omega_0x^2 > \Gamma, \quad (4.6)$$

where it is easy to see that higher gain settings  $g$  will lead to higher average damping experienced by the particle, and therefore to better cooling.

#### 4.1.2 Dependence of cooling on gain

To find the temperature  $T_{cold}$  that the particle motion will settle to in the presence of the thermal noise  $T_0$  and the feedback of strength  $g$ , one needs to rewrite the equations of motion in terms of energy distribution, resulting in the Fokker-Planck equation for energy in the presence of the feedback. These calculations were done in Ph.D. thesis by Jan Gieseler [84] and we choose not to reproduce them here, but instead just discuss the resulting equations for temperature  $T_{cold}$ :

$$T_{cold} = T_0 \left\{ 2\sqrt{\frac{\beta_0}{\alpha}} \frac{e^{-\beta_0/\alpha}}{\sqrt{\pi}\text{erfc}(\sqrt{\beta_0/\alpha})} - 2\frac{\beta_0}{\alpha} \right\}, \quad (4.7)$$

where  $\alpha = g/m\Gamma\omega$  and  $\beta_0 = 1/T_0$ . In the case of  $T_{cold} \ll T_0$ , the case that we are aiming for in the experiments, temperature dependence takes a simpler form:

$$T_{cold} \approx \sqrt{\frac{4m\Gamma\omega T_0}{\pi g k_B}}. \quad (4.8)$$

The formula 4.8 means that no lower limit for the particle temperature is expected, behavior contrary to the dependence of cooling on feedback gain observed in our

experiments (See Fig. 6.4). The difference can be explained by considering the effect the noise has on the efficiency of the feedback [85].

### 4.1.3 Noise effect on the feedback

Let us start discussion of the feedback noise by considering a measured signal  $S_n$ , where:

$$S_n = S + \eta \quad (4.9)$$

and  $\eta$  is a white noise that comes from the photodetectors used for signal detection. Typical signal to noise ratio (ratio of the signal peaks at the eigenfrequency of motion to the noise floor at room temperature) is about 4, and the noise was found to be a limiting factor for our cooling.

The nature of white noise (its presence in all frequencies below the low-pass filter cut-off) is a big issue for our feedback scheme. Since the feedback signal generated by the FPGA is equal to  $S_{feed} = S_n \dot{S}_n$ , a whole range of cross terms between the signal and the noise will be present in the feedback spectrum.

To be more specific, the difference between the ideal feedback and the experimental feedback can be written as:

$$S_{feed} = S\dot{S} + S_{noise} = S\dot{S} + \eta\dot{S} + \dot{\eta}S + \eta\dot{\eta}. \quad (4.10)$$

In the last equation, our discussion can be limited to only those terms that affect the feedback efficiency the most. Our signal  $S$  can be presented as sum of three independent harmonics,  $S = S_x + S_y + S_z$ , where  $S_x$ ,  $S_y$  and  $S_z$  are non-degenerate harmonics of

motion along  $X$ ,  $Y$  and  $Z$  axes. Therefore, the ideal feedback would have components at frequencies limited to  $\omega_{x,y,z} + \omega_{x,y,z}$  ( $\omega_x + \omega_y$ ,  $\omega_x + \omega_z$ , etc.). Of those harmonics, the harmonics that lead to the cooling are the components at  $2 \times \omega_x$ ,  $2 \times \omega_y$  and  $2 \times \omega_z$ . The rest of the cross-terms in ideal feedback are usually very small and don't have any effect on the cooling.

Hence, the terms in  $S_{noise}$  that have  $2 \times \omega_{x,y,z}$  frequency will be what limits the cooling:

$$S_{fnoise} \approx \sum_{\omega_i=\omega_x,\omega_y,\omega_z} \int \omega \eta(\omega_1) S(\omega_2) \delta(\omega_i - \omega_1 - \omega_2) d\omega_1 d\omega_2, \quad (4.11)$$

where  $\eta(\omega)$  is a white noise frequency component at a frequency  $\omega$ . The last equation shows the importance of the bandwidth in the coupling of the white noise to the feedback, since the value of the integral depends on the integration limits, which in turn are defined by the bandwidth. For our experiments, the used bandwidth used is limited by a requirement of detecting both the smallest and the largest eigenfrequencies of motion making it necessary to keep it around 1 kHz.

## 4.2 Derivation of equations of motion

To get more insight into the way noise changes the cooling temperature  $T_{cold}$ , we derive equations of motion in the presence of a noisy feedback and then extend the derivation to an experimentally important case of non-zero DC fields.

Let us consider the motion of the flake along the  $X$  axis in the presence of the thermal force  $\sqrt{2m\Gamma_0 k T_0} \xi$ , where  $\xi$  is a white noise variable. We also assume that the AM modulation of the trap stiffness is much smaller than the stiffness  $k_0$ , with the

resulting equation describing a so-called Brownian parametric oscillator [86]:

$$\ddot{x} + \Gamma_0 \dot{x} + [\omega_0^2 + 2g S \dot{S} \omega_0] x = \frac{1}{m} \sqrt{2m\Gamma_0 k T_0} \xi. \quad (4.12)$$

Here, we are actually interested only in the component of the signal  $S$  that is generated from the motion along the  $X$  axis and we can replace signal  $S$  with:

$$S = S_x(x + \eta), \quad (4.13)$$

where  $S_x$  is the scaling factor relating signal  $S$  and  $x$ . The derivative of the signal  $S$  can be rewritten in a similar way:

$$\dot{S} = \frac{\Delta S}{\Delta t} = \frac{S_x}{\Delta t} (\dot{x} + \eta'), \quad (4.14)$$

where  $\eta'$  is a symbolical representation of the derivative of the noise  $\eta$  and we used  $\Delta$  symbol to represent that derivative is taken digitally in our system and  $\Delta t = 15$  microseconds.

Finally, we can write down the equation of motion as:

$$\ddot{x} + \Gamma_0 \dot{x} + \frac{1}{m} [k_0 + k_1(x\dot{x} + \eta\dot{x} + x\dot{\eta} + \eta\dot{\eta})] x = \frac{1}{m} \sqrt{2m\Gamma_0 k T_0} \xi, \quad (4.15)$$

where  $k_1$  is the overall strength of the feedback and  $k_0 = m \omega_0^2$ . The equation 4.15 is written in a form that can be used for numerical simulations or for derivation of energy distribution.

### 4.2.1 Effect of DC fields

In the presence of stray field  $E_{dc}$ , equation 4.15 can be rewritten as:

$$\ddot{x} + \Gamma_0 \dot{x} + \frac{1}{m} [k_0 + k_1(x\dot{x} + \tilde{\eta})]x - \frac{qE_{dc}}{m} = \frac{1}{m} \sqrt{2m\Gamma_0 k T_0} \xi. \quad (4.16)$$

The last equation is written based on the assumption that signal  $S$  is proportional to  $x$ , which is true only if no lens adjustment is done. The lens motion under the influence of the lens feedback (see Chapter 4) can be taken into account by replacing  $x$  with  $x - x_{dc}$  in the equation for a feedback signal  $S_{feed}$ , where  $x_{dc}$  is the average position of the particle. Here, the modification in the formula for a feedback corrects for the location at which we want our cooled down flake to be ( $x = x_{dc}$  instead of  $x = 0$ ):

$$\ddot{x} + \Gamma_0 \dot{x} + \frac{1}{m} \{k_0 + k_1[(x - x_{dc})(x - x_{dc}) + \tilde{\eta}]\}x - \frac{qE_{dc}}{m} = \frac{1}{m} \sqrt{2m\Gamma_0 k T_0} \xi, \quad (4.17)$$

where  $x_{dc} = qE_{dc}/k_0$  as can be found from an equilibrium condition. By expanding the feedback terms, shifting  $x \rightarrow x - x_{dc}$  and combining distinct noise contributions, we get:

$$\ddot{x} + \left[ \Gamma_0 + \frac{k_1}{m}(x + x_{dc})x \right] \dot{x} + \frac{1}{m} k_0 x + \frac{1}{m} \underline{k_1 x \tilde{\eta}} + \frac{1}{m} \underline{k_1 x_{dc} \tilde{\eta}} = \frac{1}{m} \sqrt{2m\Gamma_0 k T_0} \xi. \quad (4.18)$$

Two of the underlined terms are the noise terms that couple to the particle motion when the feedback is turned on, and we conclude that the presence of the double underlined noise term depends on the value of the DC fields experienced by the flake.

This effect was experimentally observed and was shown to be the limiting factor for cooling if no stray fields nulling was implemented (see Chapter 7).

If we consider the feedback noise as an additional dissipation source, we can write an effective noise force acting on the flake motion:

$$F_{noise} = -k_1 x^2 \eta' - k_1 x \dot{x} \eta - k_1 x x_{dc} \eta' - k_1 x_{dc} \dot{x} \eta - k_1 \eta \eta' x_{dc} + \sqrt{2m\Gamma_0 k T_0} \xi, \quad (4.19)$$

where we have explicitly rewritten  $\tilde{\eta}$  in terms of its components.

It is easy to see that presence of the noise in the feedback leads to various thermal-like forces which can be phenomenologically described as leading to a new  $T'_0$  that is a sum of noise components squared:

$$T'_0 = T_0 + C_1 x_{dc}^2 k_1^2 + C_2 k_1^2, \quad (4.20)$$

where the derivation of coefficients of  $C_1$  and  $C_2$  is a challenging problem and goes beyond the scope of this thesis.

By taking into account  $T'_0$ , we can write down the modification of Eq. 4.8, which is predicted to describe an approximate formula for particle motion in the presence of the feedback noise and DC stray fields:

$$T_{cold} \sim \left[ \frac{T_0}{k_1} \right]^{1/2} \rightarrow T_{cold} \sim \left[ \frac{T_0}{k_1} + C_1 x_{dc}^2 k_1 + C_2 k_1 \right]^{1/2}. \quad (4.21)$$

Last equation shows that unlike the case of an ideal feedback, there is a minimum cooling temperature that is achieved by choosing a proper feedback gain setting  $k_{opt} =$

$\sqrt{(C_1 x_{dc}^2 + C_2)/T_0}$ . If one were to use smaller feedback setting, the particle motion will not be cooled enough, while using larger value of the gain would lead to higher noise contribution from DC stray fields and/or white noise (see Fig 4.2.b).

#### 4.2.2 Alternative explanation of DC noise coupling

In this subsection we describe a different way to understand the reason of why non-zero DC fields lead to stronger coupling of the noise. In the presence of non-zero electric fields, the electrical force displaces the particle from the trap center by  $x_{dc}$ . Here, the displacement  $x_{dc}$  can be found from an equilibrium equation:

$$F_x = qE_x - m\omega_x^2 x_{dc} = 0.$$

In the presence of a time changing component  $\delta\omega_x(t)$  in the  $\omega_x$ , as can be created by a feedback or a feedback noise, the variance of the force  $F_x$  can be written as:

$$\delta F_x = -2m\omega_x x_{dc} \delta\omega_x(t), \quad (4.22)$$

where we assume that  $\delta\omega_x(t) \ll \omega_x(t)$ . The resulting displacement depends on the frequency at which  $\delta\omega_x(t)$  acts and if we consider its component  $\delta\omega_x^0 e^{i\omega t}$  at some frequency  $\omega$ , we can write down the displacement of the particle as:

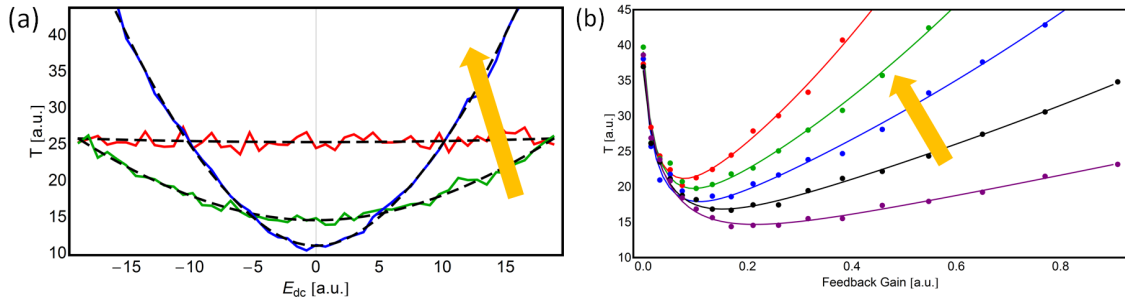
$$\delta x(t) = -x_{dc} \frac{2\omega_x^2}{\omega_x^2 - \omega^2 - i\Gamma\omega_x} \frac{\delta\omega_x^0}{\omega_x} e^{i\omega t}.$$

If we consider that one of the sources for  $\delta\omega_x(t)$  is the noise in the feedback (proportional to the feedback gain and thus to  $k_1$ ) and the relationship  $T \sim \langle \delta x^2 \rangle$ , we can conclude that for large enough feedback noise (such as generated by large enough  $x_{dc}$ ), the cooling temperature is expected to start to depend on  $x_{dc}$ :

$$T_{cold} \sim \sqrt{\frac{T_0}{k_1}} \rightarrow T_{cold} \sim \sqrt{\frac{T_0 + C_0 k_1^2 + C_2 (k_1 x_{dc})^2 + C_4 (k_1 x_{dc})^4 + \dots}{k_1}}, \quad (4.23)$$

where  $C_0, C_2, C_4, \dots$  are coefficients that can be found either through rigorous calculations or through numerical simulations. Here, we have added  $C_0$  term to account for noise contribution present in the parametric feedback even after the DC stray fields are nulled (see Eq. 4.19).

**Figure 4.2:** (a) Numerical Simulation of  $T$  dependence on DC stray field value  $E_{dc}$ . The fit with  $C_0, C_2$  and  $C_4$  is shown as dashed black curves and same values of the coefficients were used to fit all three curves. Gain settings of  $k_1 = 0.032$  (red),  $k_1 = 0.169$  (green) and  $k_1 = 0.545$  (blue) were chosen for simulation. (b) Numerical Simulation of  $T$  dependence on feedback gain  $k_1$  at different stray fields strengths. The yellow arrows are shown for both plots to point the direction, which the feedback strength (a) and stray fields strength (b) are increased.



### 4.2.3 Numerical simulation

While the derivation of exact corrections to the  $T_{cold}$  is left for future calculations, we have still numerically simulated the particle temperature dependence on gain and  $x_{dc}$  value (higher  $x_{dc}$  corresponds to stronger patch fields) to see what to expect from interaction between the noise and the feedback. The simulation was done by numerically solving the Eq. 4.18 for various feedback strength settings  $k_1$  in the presence of thermal noise  $T_0$ , with white noise of temperature  $T_{noise} = 0.17T_0$  coupling to the equations through the feedback. In Fig. 4.2.a we show how the simulation data fits to Eq. 4.23, where we have kept only the two lowest terms in  $x_{dc}$  series. This leaves us with four fitting coefficients ( $C_0$ ,  $C_1$ ,  $C_2$  and overall prefactor), where only thing that changes between curves is the feedback strength  $k_1$ . As can be seen, the formula fits three different curves very well, showing that the semi-empirical Eq. 4.23 describes the expected cooling behavior in a sufficient way.

The dependence of simulated temperatures on feedback strength  $k_1$  is shown in Fig. 4.2.b at different patch fields values, with stronger patch fields having higher feedback saturation temperature (fields strength is increased from curve to curve following the yellow arrow direction). At the same time, even zero patch fields (purple line in Fig. 4.2b) still shows the feedback saturation. This is the result of the interaction between the white noise and the feedback, and can be used as an explanation of why we have observed the feedback saturation in our experiments.

## 4.3 Conclusions

The main points of this chapter can be summarized as follows:

- Particle cooling is expected to be dependent on the DC stray fields values, and the nulling procedure is required for achieving optimal cooling
- Two regimes can be distinguished, depending on the DC stray fields nulling and strength of the feedback: regime, where increasing feedback strength improves the cooling and regime, where cooling is limited by noise and increasing feedback strength does not improve cooling, but rather makes it worse
- Based on previous statement, there is an optimal setting for a feedback strength, value of which depends on the noise level (at zero noise level, increasing feedback strength would always lead to better cooling, see Eq. 4.8)

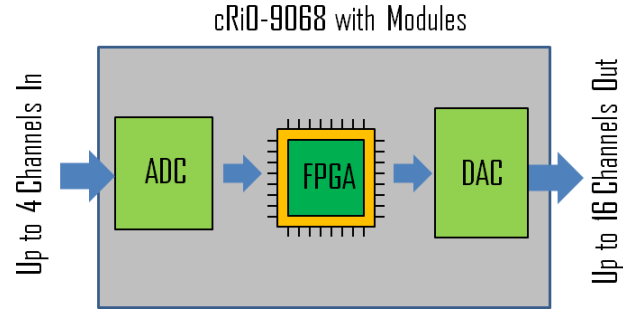
### Field Programmable Gate Array (FPGA) control

---

#### 5.1 FPGA overview

The heart of our feedback system is located at the Field-Programmable Gate Array (FPGA). The FPGA is a flexible device that is easy to customize according to the needs of experiment and consists of a large amount of transistor gates, with quantities reaching tens of millions in modern FPGA. The customization is done by programming the exact connections between these transistors that are typically combined in construction blocks of a few basic level gates. In order to speed up the programming process, National Instruments has designed and is currently producing the FPGA modules that consist of FPGA core embedded in the hardware module, which has multiple slots where input/output/processing modules can be placed in. In this setup the FPGA serves as a programmable CPU unit in a way similar to a regular personal computer.

The specific model of the FPGA module/controller used in our experiment is cRIO-

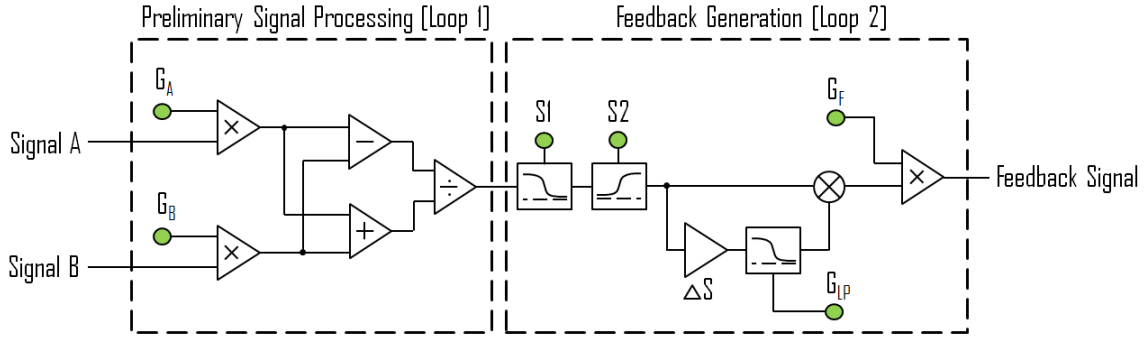
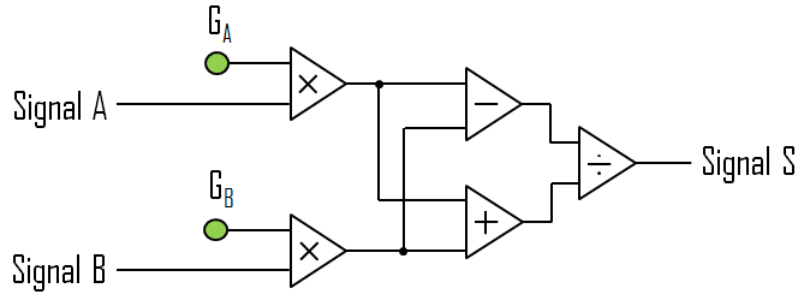
**Figure 5.1:** Scheme of FPGA integration in the experiment.

9068, which was chosen based on capacity of its memory, gates number and on number of slots available for the external modules (See Fig. 5.1). For this type of controller, we have checked that sufficient number of FPGA programs can be fit into the core, including any future designs, and current usage is about 20 % of its total capacity. The modules currently connected are described in the table 5.1. The internal program

**Table 5.1:** FPGA modules installed into the cRIO-9068 controller.

Module Name	Ins	Outs	Purpose
NI-9215	4	-	Main digital-analog converter [2 Ins used, 2 Grounded]
NI-9402	4(0)	0(4)	Bidirectional digital I/O
NI-9264	-	16	16 outs to generate signals via FPGA
5 extra slots	-	-	Up to 5 more NI modules can be installed

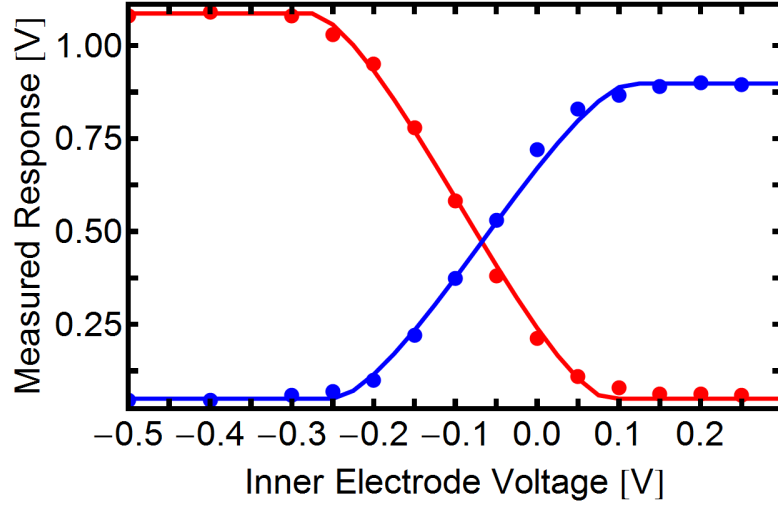
compiled on FPGA for our measurements is schematically represented in Fig. 5.2, where we have depicted two main loops used in the experiment. The first loop, used for conversion of signal detected by Analog Digital Converter (ADC) module operates at an ADC measurement speed, with each measurement taking about 6-20  $\mu$ s to make, depending on the number of the used ADC channels. This value can be improved on, if a faster ADC module is installed, and can be as high as 40 MHz (internal FPGA clock

**Figure 5.2:** Schematics of FPGA VI.**Figure 5.3:** Schematics of loop for signal amplification.

rate). The second (feedback generation) loop is set at a lower frequency of 66 kHz, which is sufficient for our experiments, where all signal frequencies we are interested in are well below 66 kHz.

## 5.2 Signal amplification and balancing

Since our main signal comes from a pair of photodetectors (see Fig. 3.6.b) and their saturation levels are not the same, the preliminary calibration is required in order to get the same response from each photodetector for a given particle displacement. If saturation voltages are measured for the same input signal (e.g. the particle image), they can be used to extract the coefficient which the signal from a weaker photodetector needs to be multiplied by. This was done by varying the DC voltage at the inner

**Figure 5.4:** Measured signals from photodetectors *A* and *B* vs. inner electrode voltage.

electrode, which results in the motion of the particle along the *Z* axis of the trap, and recording the change in the voltages measured by photodetectors (See Fig. 5.4). The beam splitter was positioned to give zero response from *X/Y* motion for this measurement (See Fig. 3.7).

To extract exact gain values  $G_A$  and  $G_B$  for the input signals *A* and *B* (See Fig. 5.3), we model the particle image as a disk of radius  $R$ , part of which is detected by photodetector *A* and part by photodetector *B*, depending on the particle displacement  $z$  from the knifeedge of the prism:

$$S_A = \frac{S_0}{\pi} \left[ \arccos \frac{z}{R} - \frac{z}{R} \sqrt{1 - \frac{z^2}{R^2}} \right] \quad (5.1)$$

$$S_B = S_0 - S_A, \quad (5.2)$$

where  $S_0$  is a total signal from the particle. Since the change in the electrode voltage leads to linear shift of the particle position  $z = \mu(V_Z - V_Z^0)$ , where  $\mu$  is the scaling

coefficient, we can extract the  $G_A/G_B$  ratio by fitting observed curves to Eq. 5.1 with  $S_A$  and  $S_B$  multiplied by  $G_B$  and  $G_A$ . The ratio found this way:

$$\frac{G_A}{G_B} \approx 1.22, \quad (5.3)$$

the value that was set and never changed in our experiments.

After the signals are scaled and subtracted from each other, we can calculate signal  $S$ , which is defined as:

$$S = \frac{A - B}{A + B}, \quad (5.4)$$

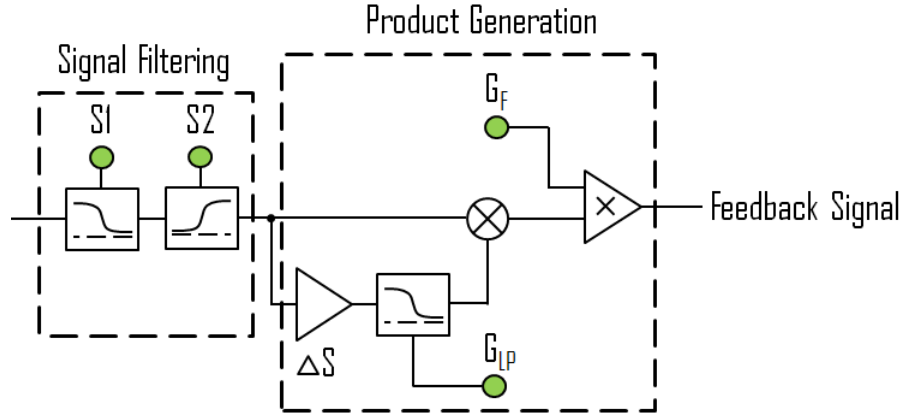
where  $A$  and  $B$  are the signals from photodetectors  $A$  and  $B$  after their scaling. Signal  $S$  provides a normalized motion signal, limiting the effects from variance in the particle brightness or laser power change. The  $A+B$  part of this signal is digitally filtered using a low-pass filter ( $f_c = 4.4$  Hz).

### 5.3 Signal filters and signal phase shift

After the signal  $S$  is acquired, it is important to filter out all the unnecessary signal components. The filtering was done by a band-pass filter made of a sequence of two digital high-pass and two digital low-pass filters of 1st order, where all filters were written as single pole recursive filters [87]. Both low-pass and high-pass filters are defined in terms of their output  $\hat{S}_n$  and can be written as:

$$\hat{S}_{n+1} = \alpha S_n + (1 - \alpha) \hat{S}_{n-1} \quad (5.5)$$

**Figure 5.5:** Feedback loop consists of two subloops. First loop is used for signal filtering. The second generates a product of the signal by its derivative and scales the product based on gain  $G_F$ .



for the low-pass filter, and:

$$\hat{S}_{n+1} = \frac{\alpha + 1}{2} S_n - \frac{\alpha + 1}{2} S_{n-1} + \alpha \hat{S}_{n-1} \quad (5.6)$$

for the high-pass filter, where  $\alpha$  is the digital setting of the filter, defining its cut-off frequency [87] and  $S_n$  is the  $n$ -th signal point processed by the FPGA. The reason behind using this version of the band-pass filter is the minimization of memory space required for the compiled filter. This is related to the way FPGA filter logic grows, when the filter order is increased. Adding one more order to the filter not only increases the total number components that need to be considered (which grows linearly with a filter order), but also all the interconnecting logic, which turns out to take a lot of space. For example, the initially used cRIO-9075 had a memory space that was easily filled by the 4th-5th order filters.

While memory/space capacities of the current FPGA module stopped being a limiting factor, we have settled on using the simplest signal filtering in order to avoid

possible complications (e.g. filter instability) that can arise, when complex digital filters are considered [87]. Therefore, it is important to remember that the band pass filter we use is not necessarily the best filter to have, and an improvement of signal over noise ratio can be searched for by considering other filter schemes.

Before discussing any further signal processing, it is important to discuss the phase delay that is acquired by signal during the filtering and at the ADC stage. The delay of the filtered signal is frequency dependent, with filter delay calculated by adding up phase delays of each filter. There is also an additional phase delay component that appears during the ADC conversion. The ADC module delay is strongly affected by number of channels used and we had to limit the number of channels we connect to ADC down to two in order to speed up the signal conversion (ADC has a max of four channels available for input). In this case, the delay is about  $\tau = 38 \mu s$  and though this number doesn't look large, one has to remember that at frequencies of even 2 kHz this will lead to the phase shift of about 30 degrees. The exact formula for the phase shift at a given frequency  $f$  after bandpass filtering is given by formula:

$$\Delta\varphi(f) = -360 \cdot f \cdot \tau + 2 \cdot \frac{180}{\pi} \left[ -\text{atan} \left[ \frac{f}{f_{LP}} \right] + \frac{\pi}{2} - \text{atan} \left[ \frac{f}{f_{HP}} \right] \right], \quad (5.7)$$

where  $\tau$  is digital delay from analog to digital conversion,  $f_{LP}$  and  $f_{HP}$  are low-pass and high pass cut-off frequencies.

## 5.4 Feedback generation

As mentioned earlier, the FPGA's main purpose is to create a feedback signal that is sent to the wave generator input for amplitude modulation. We have chosen to use the scheme implemented in Ref. [44], which had  $S_{feed} = S\dot{S}$ , where  $\dot{S}$  is taken digitally in our setup. Digital derivative means that  $\dot{S} \sim (S_{n+1} - S_n)/\Delta t$ , where  $n$  and  $n + 1$  are indices of two consecutive data points separated by a signal acquisition time  $\Delta t$ . In order to avoid additional time delays in processing and digital rounding errors, we chose our feedback to have a form of

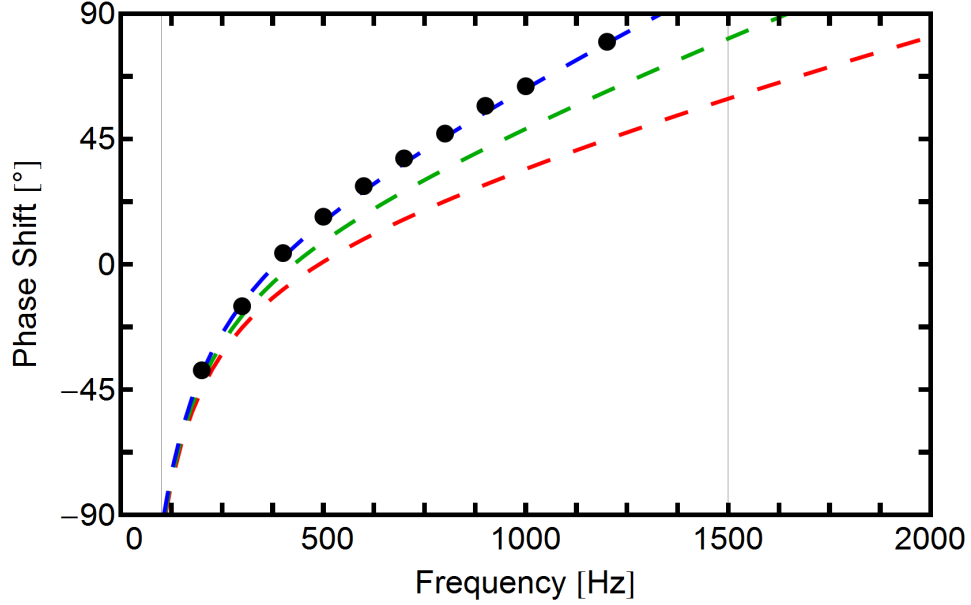
$$S_{feed} = (S_{n+2} + S_n)(S_{n+2} - S_n), \quad (5.8)$$

which is functionally the same to  $S\dot{S}$  and division by  $\Delta t$  would just use an extra FPGA space.

We have chosen to use points separated by  $2\Delta t$  ( $n$  and  $n + 2$ ) instead of  $\Delta t$  ( $n$  and  $n + 1$ ), because we have found that this helps to make digital effects from subtracting two points much lower than in the case when the version of the derivative with two consecutive points is used. The signal difference is low-pass filtered to decrease the digitization spikes in the signal even further.

As mentioned earlier, the signal processing leads to an extra phase shift that is dependent on the frequency, which in turn leads to the phase shift of the feedback at

**Figure 5.6:** Phase shift of generated feedback signal relative to the ideal feedback signal for three different values of filter settings. At phase shifts greater than 90 degrees, the feedback leads to heating rather than to cooling of the particle motion.



twice the phase shift of the filtered signal:

$$\Delta\varphi_{feedback} \approx 2\Delta\varphi. \quad (5.9)$$

The  $\approx$  sign is used in the last equation, because of the minor correction that is added to the feedback phase shift due to the low-pass filtering of the digital derivative. This correction is neglected as being much smaller than the shift values discussed below.

Since our feedback relies on having a right phase shift between the feedback signal and the particle motion, adding an extra phase shift from signal processing would make the cooling inefficient or even lead to heating(!) of the motion if the phase shift becomes greater than  $\pm 90$  degrees. As can be seen from plot showing the phase shift versus frequency dependence (see Fig. 5.6), only frequencies that lie in a small

frequency region (between 100 Hz and 2000 Hz for the parameters shown by a red dashed line in Fig. 5.6) have phase shift within the  $\pm 90$  degrees region. This places a big restriction on operation of the feedback and the type of particles that can be cooled, since each of the three eigenfrequencies of particle has to be within the positive feedback region. If one or more eigenfrequencies are outside of the region, turning up the cooling scheme results in a fast loss of the particle within only a few seconds.

As a quick note, we would like to point out that although the filtering does lead to the phase shift, the dominant contribution to the phase comes from the constant term. Higher speed ADC can be used to amend this issue, though quick search of the module models available for our cRIO controller shows that the acquisition time can not be improved by more than a factor of ten.

## 5.5 Correction of lens position

The last loop in the FPGA program is responsible for controlling position of the lens. The lens is held at the piezoelectric stage with three degrees of motion, two of which are connected to the same voltage output (two degrees moving in directions parallel to lens' focal plane), while the third one is grounded. The voltage is generated by the high voltage amplifier that gives an output  $V_{\text{HVA}} = 3.46 V_{\text{IN}}$ , where  $V_{\text{IN}}$  is limited by a digital-analog converter range of  $\{-10, 10\}$  V. The  $V_{\text{IN}}$  signal is created by the loop that is set to have a very long time scale via filtering the signal  $S$  through low-pass filter with  $f_c = 4.4$  Hz. The cut-off frequency value is usually kept the same during experiments, but is sometimes adjusted to be even lower if particle motion is too unstable (averaged position of the particle has a time component slower than the

set  $f_c$  frequency). If position of the lens is not properly controlled, the particle escape can happen due to the improper feedback generation (feedback will be proportional to average particle position rather than the fast component of the motion).

---

## Flakes in high vacuum

---

### 6.1 Calibration of signal

Before discussing the cooling of the particle motion, it is necessary to calibrate the motion in terms of temperature. Since the particle motion at high enough pressures (pressures higher than 1 mTorr in our case) is thermalized with the ambient gas [13], the signal  $S$  measured in those conditions can be used as a calibration setpoint of 293 K (ambient temperature).

As is known from the fluctuation-dissipation theorem [5], power spectrum of the motion in a harmonic potential in the presence of a thermal bath can be written as:

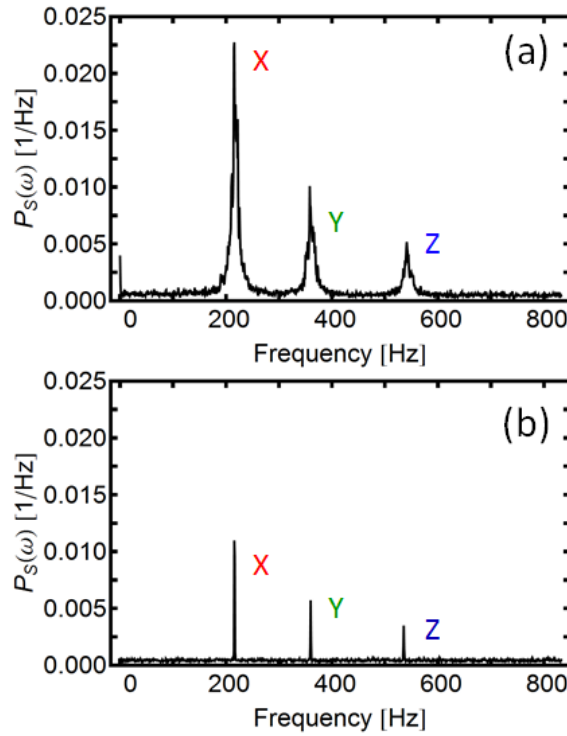
$$P_{xx} = \frac{2\Gamma k_B T}{m} \frac{1}{(\omega^2 - \omega_x^2)^2 + \Gamma^2 \omega^2}, \quad (6.1)$$

where the integral over frequency gives:

$$\langle x^2 \rangle = \frac{k_b T}{m \omega_x^2} = \int_{\omega_x} P_{xx}(\omega) d\omega \sim \int_{\omega_x} P_S(\omega) d\omega, \quad (6.2)$$

where  $P_S$  is the power spectrum of the signal  $S$  taken in the vicinity of  $\omega_x$ . Here, we

**Figure 6.1:** Power spectrum of signal  $S$  at pressure of 4 mTorr (a) and  $4 \times 10^{-7}$  Torr (b).



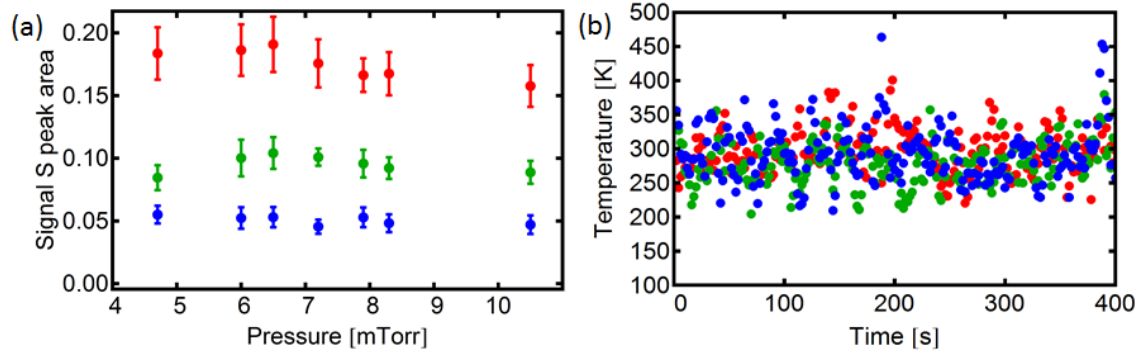
wrote equations for motion along  $X$  axis, but similar equations can be written for two other axes. Ability to separate contributions to the signal  $S$  from different degrees of freedom is the result of the previously discussed asymmetry of our trap (See Chapter 2 for discussion of the trap and Chapter 3 for discussion of signal detection). As can be seen by plotting the spectrum of the signal  $S$ , the motion along each of the trap axes is easily distinguished from the rest (see Fig. 6.1). The Fig. 6.1 shows the spectrum in

two different regimes - 4 mTorr (used for motion calibration) and  $4 \times 10^{-7}$  Torr. In both cases, the clear separation of peaks from each other is visible and area under each peak is proportional to  $T$  as mentioned in Eq. 6.2. While the Fast Fourier Transform (FFT) implemented in our setup does not provide high enough resolution to have more than 4-5 data points per each peak in Fig. 6.1.b, the following discussion does not rely on high resolution of the peaks since only total area of the peaks is used for calibration. This, in combination with the Parseval's theorem, allows us to use the calibration for all pressures. At the same time, if study of the peaks themselves is required (e.g. if the shape of the peaks in the presence of the feedback and the corresponding damping are of interest), a new implementation of FFT with better resolution will have to be added.

As a first step of calibration, we measure areas under each of the peaks in the power spectrum  $P_s$  at different pressures (see Fig. 6.2), procedure equivalent to taking integral under the peak. This is done to check that the pressures used for calibration are high enough to avoid an overheating of the particle motion by the laser. The values found this way are used to scale all the experimental data (see Fig. 6.2.b for typical data after calibration).

It is important to point out that recalibration is required every time a new particle is trapped, since the amount of scattered light depends on the dimensions of the particle (and if there is a suspicion that a non-graphene particle is trapped, on the particle material). At the same time the calibration is required only once per particle and was observed to stay close to constant for the whole experimental runs.

**Figure 6.2:** Peaks' dependence on pressure (a) and time (b) for motion along  $X$  (red),  $Y$  (green) and  $Z$  (blue) axes.

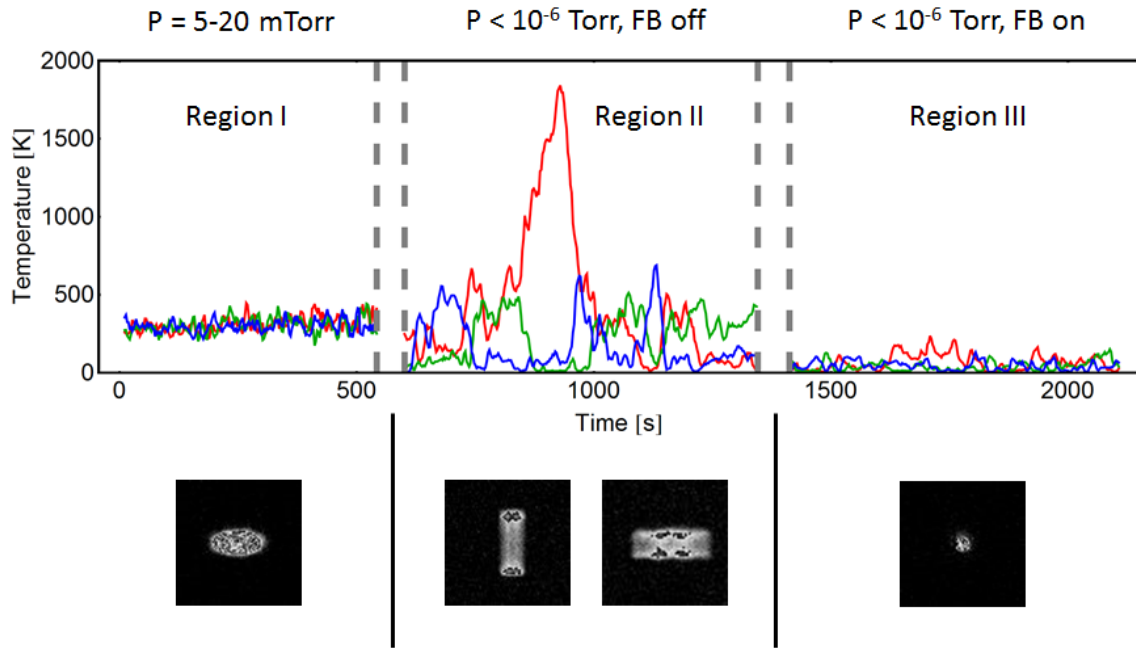


## 6.2 Particle behavior at high vacuum

We can observe the flakes heating in high vacuum by either studying their images in the CCD camera or by tracking their temperature. The first method gives a qualitative insight, useful for figuring out why particles escape and how. Temperature analysis helps to characterize how fast particles heat up.

We start the discussion of the various possible regimes by considering the configuration, in which the particle temperature is independent of the pressure (pressures of 1 mTorr or higher) and which corresponds to the thermal equilibrium of the flake with the ambient gas (Region I of Fig. 6.3). In this case,  $T_x = T_y = T_z$ , and CCD image of the flake in that regime is shown below the time plot. The ellipsoid-like nature of image is the result of larger thermal oscillations of the flake along  $X$  and  $Y$  axes compared to  $Z$  (see Eq. 6.2).

**Figure 6.3:** Comparison of different regimes of particle motion (description in the text). Curves are labeled as red ( $T_x$ ), green ( $T_y$ ) and blue ( $T_z$ ).



### 6.2.1 Behavior in high vacuum without cooling

Once the pressure goes below a level sufficient for particle thermalization (Region II of Fig. 6.3, all pressures below 1 mTorr), a chaotic shaking of the particle is observed. The CCD images shown for Region II are typical of how the particle motion looks during the heating. The Lissajous curve is recognizable in one of the images, which show two examples of the particle motion during the heating. In both cases, the particle escape usually happens along the  $Z$  axis of the trap (corresponding to up-down direction of the particle images). If left uncontrolled, the excited motion leads to the escape of the flake within a few hours time scale at pressures below  $\mu$ Torr. Our current belief is that this motion is excited by the laser.

When the feedback cooling is introduced, behavior of the particle changes dramati-

ically as the particle gets stabilized (Region III of Fig. 6.3). Best cooling temperatures achieved so far are limited to about 15 K, and trapping times exceeding more than a few days were observed. We can also see that CCD image of a cooled down flake is more spherical than in the region I. This is explained due to the optics limitation which begins to dominate the visual image of the flake in the CCD camera, once the particle motion becomes lower than the optics limit.

Observed cooling and stabilization of the flake are the key results to take from this section. The behavior we have showed was repeated on many flakes and proves the viability of our approach with two caveats involved. First, cooling of a mono-layer flake has not been tested for, since even trapping and checking whether a flake is close to a monolayer one is currently only a work in progress. Second, ultra-high vacuum conditions (pressures below  $10^{-7}$  Torr) were not seriously studied at this stage of the experiment, since we were mostly concerned with sorting out the optimization protocol for particle cooling. Hence, the UHV cooling of the monolayer graphene flake will have to be addressed in the future.

### 6.3 Cooling vs. amplitude modulation

The amount of feedback fed to the trap potential is defined by product of an internal gain of FPGA circuit  $g$  (see Chapter 5) and amplitude modulation  $G_{AM}$  set at the wave generator (see Chapter 3). Therefore, we usually vary only one of them while keeping the other constant, and the choice of which parameter to change depends on the experiment in question. For warm up/cool down experiments (see subsection below), we set up automatic jumps in internal FPGA gain to create reproducible heat-

ing/cooling conditions and leave  $G_{AM}$  setting the same. For experiments on efficiency of cooling, we set the FPGA gain to a fixed value and vary only  $G_{AM}$ .

In general, the typical operating parameters are chosen to be  $g = 20$  (as set by VI, corresponds to  $g = 2.4 \times 10^{-4}$  s in real time units) and  $G_{AM} = 30\%$  as set at the front panel of the wave generator. The reason of why we do not go to higher values of  $G_{AM}$  is related to the shot noise limitation of our cooling scheme and is described in more detail in Chapter 4. Gain value of  $g = 20$  is chosen to avoid overloading the digital-analog converters that feed the signal to the wave generator. Here, higher values of  $g$  can be chosen once the particle motion becomes sufficiently small (lower than 10-20 K), but any increase in the temperature can easily lead to the DAC overload. While such overload does not damage any equipment, it will lead to an overload in the feedback signal, resulting in a particle loss.

With these values in mind, let us study how the amplitude modulation (AM) of the trap potential affects the particle temperature ( $g = 20$  is assumed unless specified otherwise). At low values of  $G_{AM}$ , the feedback cooling does not dissipate enough energy and particle stays warm (see Fig. 6.4.a), and going to higher values of the  $G_{AM}$  improves cooling. But at values of  $G_{AM} \sim 30\%$ , there is a visible saturation of cooling and increasing a setting  $G_{AM}$  to values higher than 30% does not improve the temperature, which is explained by noise limitations of our feedback (see Chapter 4).

To be more thorough, we also show the dependence of cooling on FPGA feedback gain  $g$  in Fig. 6.4.b, where we expect a curve qualitatively similar to the one in Fig. 6.4.a, including the cooling saturation at high gain values. And indeed, it is easy to see that no improvement in cooling is observed for  $g > 20$ , explaining our choice

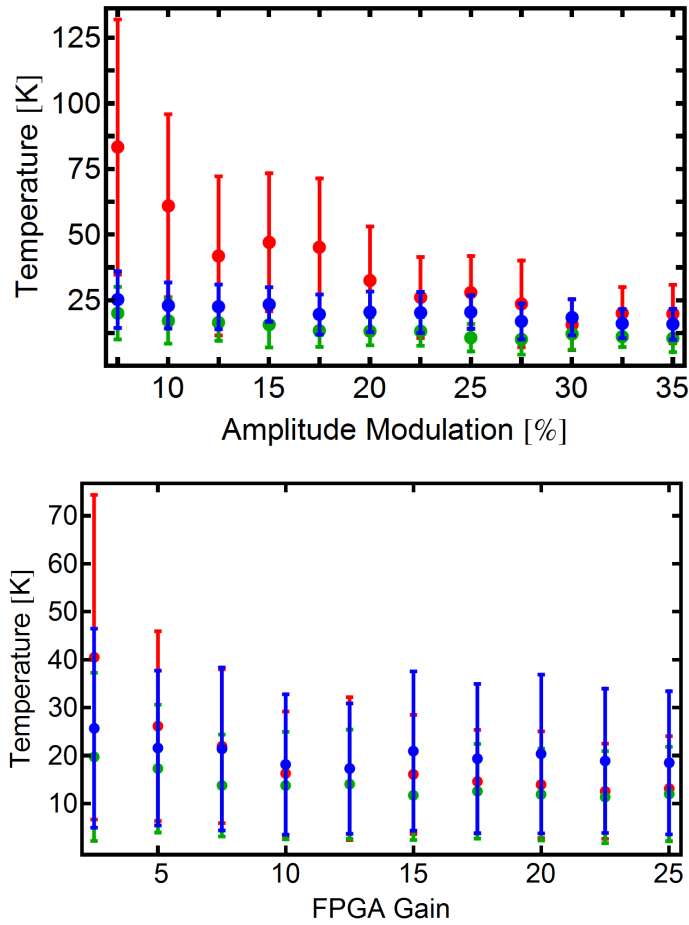
of  $g$  setpoint.

It is also interesting to note that going to higher  $G_{AM}$  settings can actually result in overheating(!) of the particle, behavior that is dependent on the quality of stray fields nulling and the amount of shot noise in the signal (see Chapter 7). Another dangerous effect is observed when  $G_{AM}$  values are set too high: a sudden escape of the flake, where no clearly measurable change in either the CCD image intensity or temperature of the particle is detected, and the escape typically happens in less than a few seconds. We suspect that this is the result of an increased sensitivity of the feedback to noise at high feedback strength values. Indeed, if a sudden jump in a signal appears due to a flake reorientation or some unwarranted shaking of the optical setup, the amount of push the particle experiences at high values of  $G_{AM}$  can be too large and will result in the flake escape.

### 6.3.1 Cooling dependence on laser power

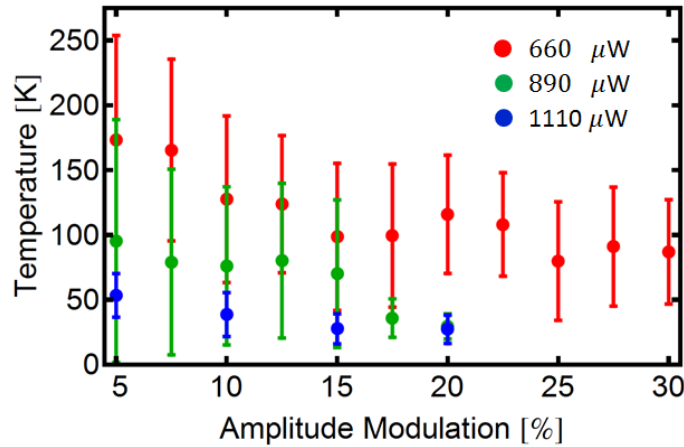
Another parameter affecting the efficiency of the cooling is the laser power. Since the cooling temperature depends on the signal to noise ratio and main contribution to the noise in our experiment comes from a shot noise of photodetectors, it is beneficial to use larger laser powers. The dark current of the photodetectors we use is about  $0.06 \mu\text{A}$  and typical current value measured from the flake is set to be about  $0.5 \mu\text{A}$  by increasing laser power to the proper level. Higher laser powers are not used for two reasons. First, we have observed a fast discharge of the flakes when exposed to laser powers bigger than  $1 \text{ mW}$  (corresponding to photocurrent levels of  $0.3\text{-}0.5 \mu\text{A}$ ). While this discharge tends to slow down from a discharge rate of about  $1 e$  per sec

**Figure 6.4:** Dependence of cooling on (a) Amplitude Modulation ( $G_{AM}$ ) and (b) FPGA gain ( $g$ ).



at the beginning of the discharge to 1  $e$  per minute (typical charge of the flake is on the order of few thousand  $+e$ ), it still makes it hard to control the particle cooling due to shifts in eigenfrequencies of motion. While we have not fully studied, whether there is a saturation point in discharge, we chose to avoid going above 1 mW in power during our experiments. The second, more general, issue is related to photodetectors and an analog-digital converter used as an input in the FPGA module, is an overload in measured photocurrent, observed at photocurrents on the order of a few  $\mu A$ .

Though it is not clear if there is a limit on how much laser power can be used in

**Figure 6.5:** Dependence of  $T_Z$  on  $G_{AM}$  at three different laser power levels.

our experiments, we have still tried to figure out if there is an optimal operating laser power for powers below 1 mW. Since the most important parameter for our experiments is the cooling temperature of the particle, we have collected curves showing dependence of  $T$  on  $G_{AM}$  at three different laser powers (see Fig. 6.5). In Fig. 6.5 we present only laser dependence of cooling for  $Z$  direction as it was observed to be the hardest to cool, and therefore is expected to depend on the laser power level the most. It can be seen that by increasing a laser power from 660  $\mu\text{W}$  to 1100  $\mu\text{W}$ , one can achieve a drastic improvement of cooling.

## 6.4 Warm up and cool down tests

Finally, we discuss a preliminary data on warming up and cooling down of the particles in high vacuum. The experiment was done on the particle spinning under the influence of the red circularly polarized laser (See Fig. 3.6.b) at pressure level of  $4 \times 10^{-7}$  Torr. For these measurements, the FPGA Gain setting  $g$  was a control variable and was set to jump back and forth between  $g = 0$  and  $g = 20$  after fixed periods

of time. The sequence of keeping  $g = 20$  for 500 sec and setting  $g = 0$  for 154 sec was repeated overnight, giving a time sequence of about 12 hours with four overnight runs conducted this way. The 197 warm-up curves were collected this way, four of which are shown in Fig. 6.6 and display the stochastic nature of the heating up [19]. By combing curves in a 3D histogram, we can get more information on how fast the particle warms up.

We expect that right after the feedback is turned off ( $g = 0$  is set), the particle is still in a cooled state and its temperature distribution will have a very small variance. The following evolution of the distribution results in a broader energy histogram at any given time with average temperature constantly going up. This means that 3D histogram density plot of total energy (labeled  $T$ ) vs. time is expected to have a triangular like shape, where the average temperature will follow a monotonically growing line (see the fit line in Fig. 6.7). Although, the amount of data taken is not enough to get information necessary for making a high resolution fit of the dependence of average temperature on time, we can still get an estimate of a heating to be about 3-5 K/sec for a total energy of the particle. This type of measurement can be useful if we try to locate and eliminate the source of the particle heating, since the speed of heating found this way can be compared with theoretical heating rates expected for different noise and heating sources.

Improvement of the experiment is required before the sufficient data averaging can be done, since it was shown in similar experiments [19] that an averaging of 10,000 curves was necessary to get detailed information about the particle energy distribution. This means that if we were to study warming of our flake to 293 K at the

speed of 5 K/sec, allowing for it to cooldown for 10-20 seconds in-between, the total experimental run will take close to 200 hours to complete. A potential speed-up in the experiment can be achieved by using higher laser powers, but their effect on the particle cooling needs to be checked for first, as mentioned earlier in this chapter.

**Figure 6.6:** Typical dependence of warm up of the particle motion, once the feedback is turned off. Four temperature trajectories, labeled 1-4, are shown for relative comparison. The difference of time dependence between the trajectories is a sign of stochastic nature of the particle heating.

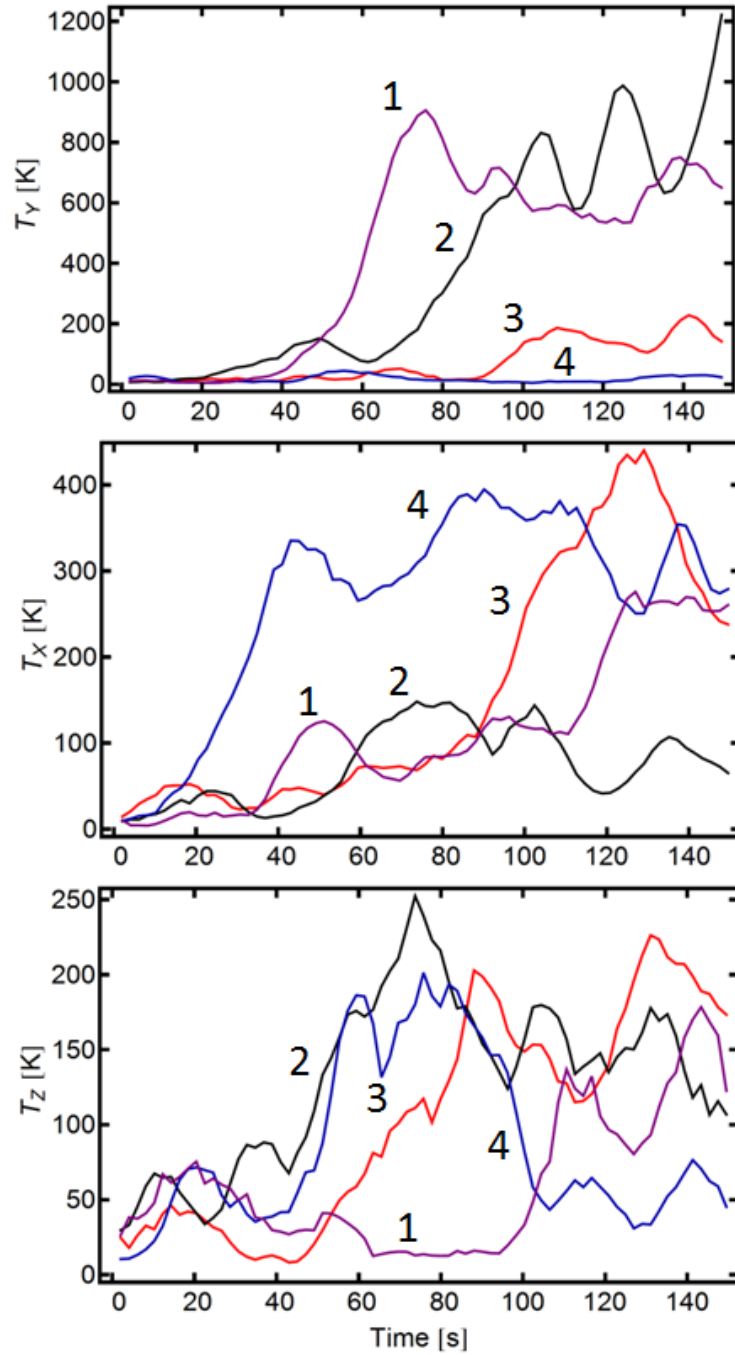
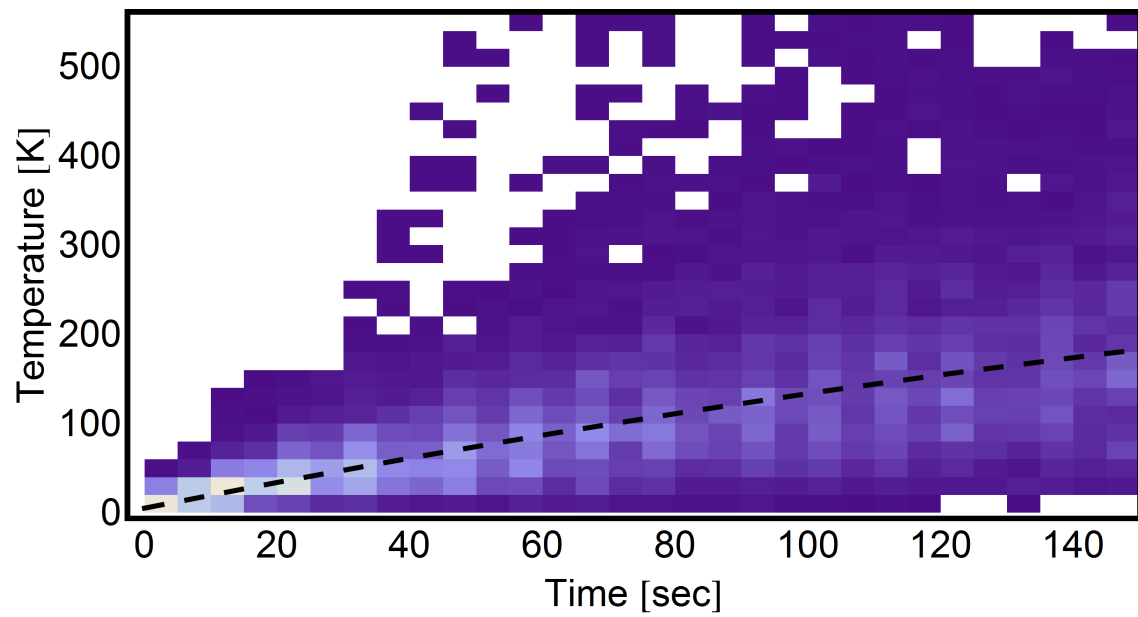


Figure 6.7: 3D Histogram of particle heating up [contains 197 heat up curves].



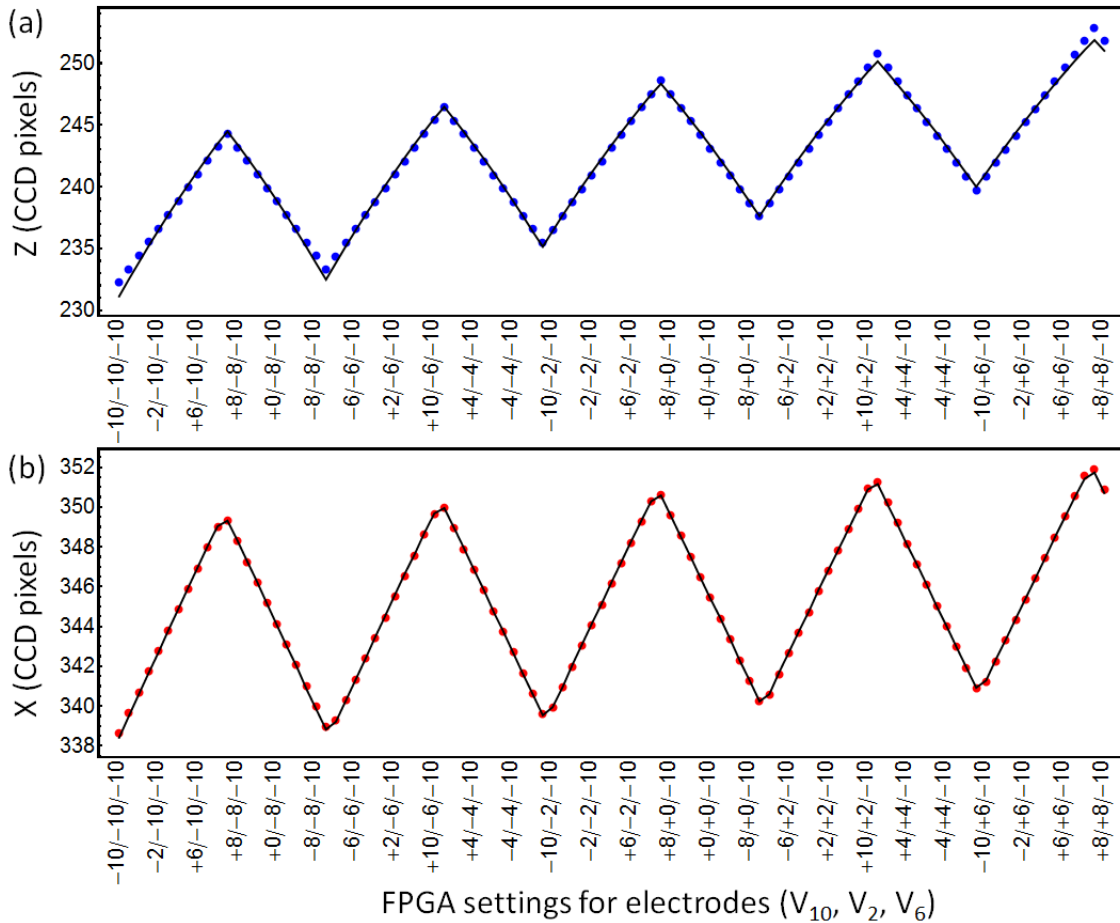
### Effect of DC fields on cooling

---

As has been mentioned in Chapter 4, the particle cooling is strongly affected by the feedback noise, which in turn depends on the DC fields acting on the flake. This means that achieving an optimal cooling requires some way to balance out any unwanted fields (also called patch or stray fields) that can be present in the chamber. In our experiment this is done by using a set of three auxiliary electrodes, which are set at a distance of about 2 cm away from the trap center (See Fig. 3.9). Electrodes are positioned at angles of about 120 degrees between each other and we label them as  $V_{10}$ ,  $V_6$  and  $V_2$  based on the clock hour hand directions. When a non-zero DC voltage is applied to one of these electrodes, there is an additional DC field created near the trap center leading to change of the total DC field acting on the trap. Therefore, by choosing a proper linear combination of voltages, we can null down the effect of any DC field. E.g., if we want to change a DC field acting along  $Z$  axis of the trap, we can apply similar voltages to all of the electrodes and so on. Since

the auxiliary electrodes are far from the trap center (a few cm) when compared to the trap size (mm scale) and motion of the flake (micron scale), their contribution to the total DC field can be approximated as having a linear effect on the particle displacement and the DC field. This can be tested by measuring the average position

**Figure 7.1:** Dependence of particle position, as measured by CCD camera, on FPGA settings of electrodes  $V_{10}/V_2/V_6$ . Linear fit is shown for comparison with measured data points.



of the flake via the CCD camera versus a variations of applied auxiliary electrodes' voltages. For our experiments, voltages are limited by FPGA settings, giving range of  $\{-10,+10\}$ V output for each of electrodes (voltages on electrodes are equal to FPGA

voltages times 3.46). As is shown in Fig. 7.1, the measured position of the flake image in CCD camera ( $X_{CCD}$  and  $Z_{CCD}$ ) fits very well to a linear combination of electrodes' voltages ( $X_{CCD}/Z_{CCD} = \gamma_{x/z}^{10} V_{10} + \gamma_{x/z}^6 V_6 + \gamma_{x/z}^2 V_2$ , where  $\gamma_{x/z}$  are some constants). This proves that our statement that contributions of electrodes to DC field at the center of the trap can be approximated as linear is valid. Interestingly, while measuring position of the flake via CCD camera gives us information only about its 2D position ( $X_{CCD}$  and  $Z_{CCD}$ ), we can still control its position/electric fields in all three directions. The only tricky position to tune is the position of the flake along the axis that is orthogonal to the CCD camera screen. This displacement can be achieved if a constraint on  $\Delta X_{CCD} = 0$  and  $\Delta Z_{CCD} = 0$  is set for electrodes voltages based on linear fits. Since the flake motion is not detected by CCD camera under the constraint even when voltages are varied, the only possible resulting motion is the motion along the desired axis.

## 7.1 Nulling of DC stray fields

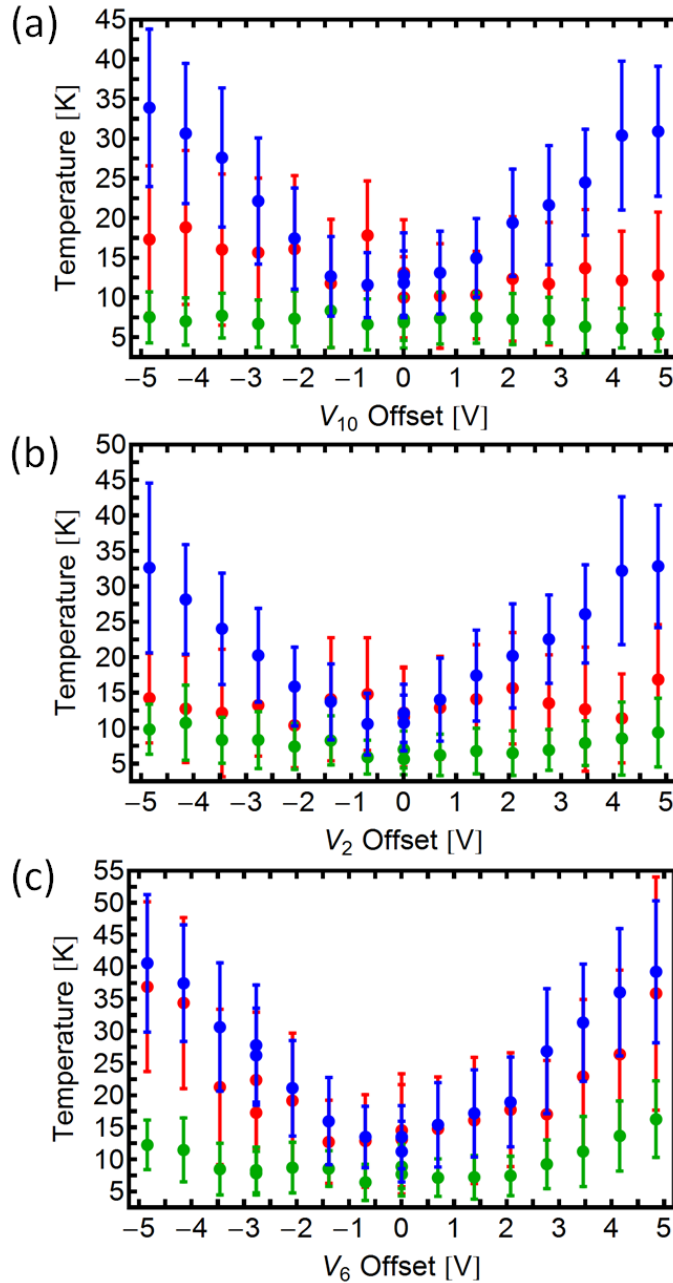
Since particle cooling is affected by any non-zero fields present (see Chapter 4 for discussion on how DC fields affect coupling of noise to the particle motion), we are interested in finding auxiliary electrodes settings that give  $E_{dc} = 0$ . The procedure is based on measuring the particle motion change created by the AM excitation at a given frequency [88], which is proportional to the particle displacement from the trap center and therefore to the amount of DC field acting on the flake. By making sure that no measurable response is observed for each of the degrees of motion, we can locate the optimal settings of auxiliary electrodes, called *nulling settings*.

The search for nulling settings is done in a few steps. At first, an arbitrary elec-

trodes configuration is chosen, while keeping the pressure level at the region of 5-30 mTorr. The response of motion to the 15-25 % AM driven by external source (lock-in amplifier Perkin-Elmer 7280 DSP) at these electrode settings is measured for lock-in frequencies set off by 50 Hz from each of three eigenfrequencies. This way, three lock-in response values are measured, where each of the numbers is proportional to the patch field acting along the corresponding direction of motion. After that similar measurements are done in the vicinity of the chosen voltages (see Appendix A for the description of full protocol).

By using a linear fit for the measured dependence of each of three lock-in responses on the electrode settings, we can estimate a nulling settings location by setting all fit values to zero. This provides us with a first-order approximation for the nulling settings, which was observed to work well enough as long as starting point is not too far from the nulling settings. E.g., if the optimal electrodes values are  $V_{10} = -1\text{V}, V_6 = -2\text{V}, V_2 = -5\text{V}$ , starting at  $V_{10} = 0\text{V}, V_6 = 0\text{V}, V_2 = 0\text{V}$  would generally work, while starting at  $V_{10} = 10\text{V}, V_6 = 10\text{V}, V_2 = 10\text{V}$  would lead to too large of a fitting error. The measurements are repeated in the vicinity of newly found settings until the satisfactory nulling of the response is achieved. Once the nulling settings are found via the lock-in response minimization, we pump down the system and turn on the feedback. This leads to particle cooling, and the electrode voltage values can be fine tuned to find exact values of the nulling settings. As an example, typical dependence of cooling temperature on small changes in DC settings near the nulling settings is shown in Fig. 7.2. As expected (see the numerical simulation in Fig. 4.2.a), there is a minimum in temperature at the nulling settings ( $E_{dc} = 0$ ), and

**Figure 7.2:** Dependence of temperature on electrode voltage near the nulling settings ( $T_X$  - red,  $T_Y$  - green,  $T_Z$  - blue): (a) vs. offset in  $V_{10}$ , (b) vs. offset in  $V_2$ , (c) vs. offset in  $V_6$ .



moving away from them leads to quick increase in the particle temperature.

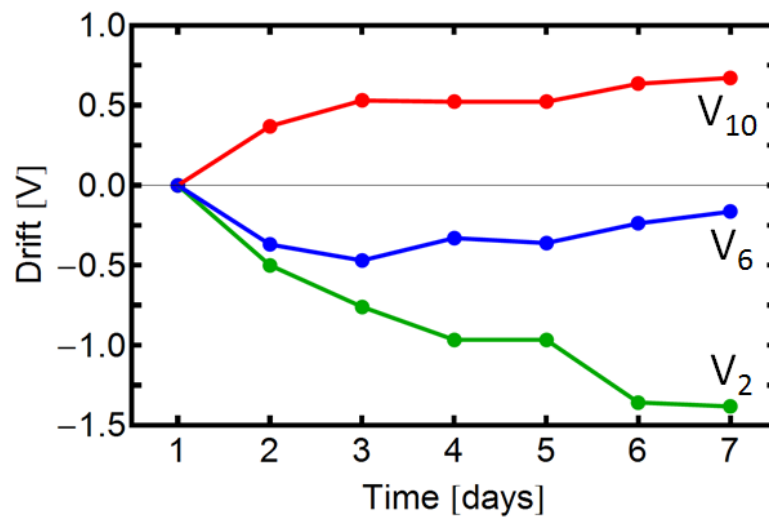
The strong dependence of cooling on DC settings shows that it is very important to null the electric fields before trying the cool down process. It also explains our initial

observation that if no nulling of the stray fields is done, cooling of the flakes was either impossible to achieve, leading to particles' escape and overheating in high vacuum, or was very inefficient and cooling only to 100-200 K was achieved.

### 7.1.1 Nulling settings dependence on time

One of the important questions to answer is how much and how fast do the nulling settings change in time. Indeed, their time dependence defines our ability to conduct experiments and to automate their readjustment without stopping the experiment. We have checked for such dependence for a time period of a week, during which other experiments were done on the particle and a few venting and pumping operations of the UHV chamber were done. The nulling settings were readjusted via lock-in response minimization and their dependence on time was observed (see Fig. 7.3). We believe that the explanation of the nulling settings drift lies in the time dependence of DC stray fields, which were previously observed to have a similar time dependence [89].

**Figure 7.3:** Drift of auxiliary electrodes settings vs time.



The speed of DC settings drift can be estimated to be about 0.6 V/day on average,

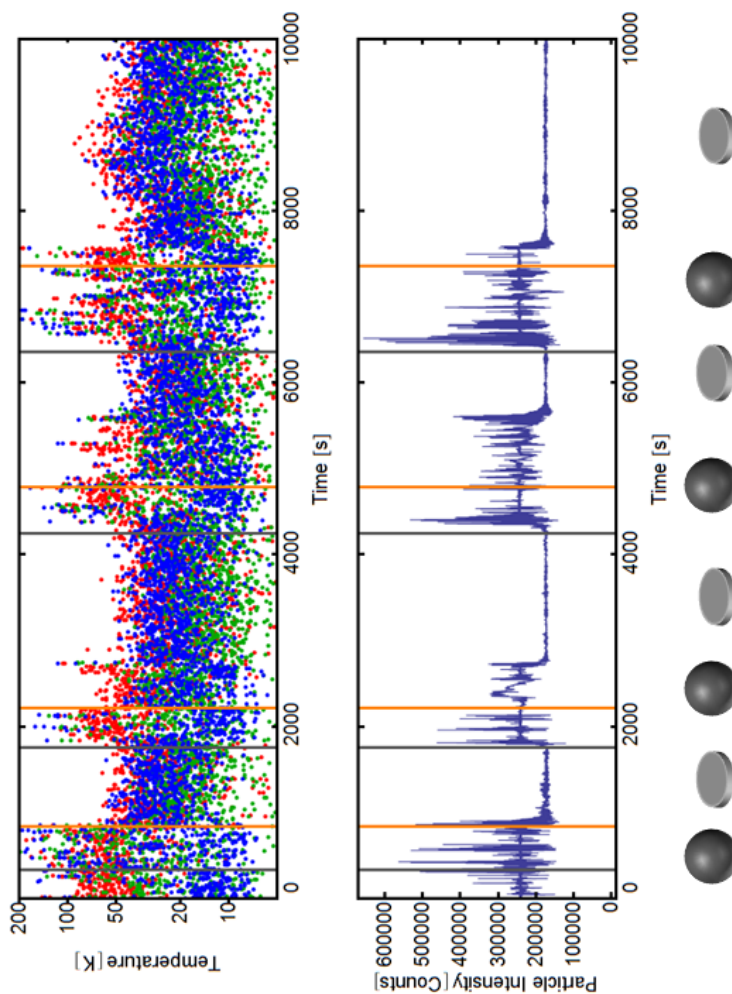
giving a change of a few percent in total value per day. In combination with the fact that quantities measured in our experiments have much faster time scales (longest time scale observed was a precession period of flakes at about 30 min/period), we chose not to modify the experimental setup. But if future experiments requiring a longer time scale were to be conducted, an additional feedback loop for varying the DC settings will need to be implemented.

### 7.1.2 Flake stabilization with circularly polarized light

Another aspect of stabilizing the particle motion is the minimization of the noise in the signal that is present due to the particle rotation and its flexural fluctuations. While this is not an issue at higher pressures, at HV and UHV pressures we have observed a significant increase in oscillations of the flake intensity. This means that some way to stabilize the particle spinning is required. The 671 nm circularly polarized laser (CPL) illuminating the particle (See Fig. 3.6.b) was chosen for this purpose and its effect on the efficiency of cooling has been studied. As can be seen from Fig. 7.4.b, where we turn the red laser on and off (red laser power = 200  $\mu$ W), the particle intensity fluctuations do depend on whether the laser is turned on. When the laser is off, high oscillations and larger average intensity value are observed (regions between gray and orange lines), with the cooling temperature showing a fluctuating behavior (see Fig. 7.4.a). Turning the red laser on leads to forced spinning and reorientation of the flake to lay in the  $X - Y$  plane. At the same time, intensity fluctuations vanish and resulting improvement of signal to noise ratio leads to higher stability and better cooling with  $T$  going down from 30-50 K down to 10-20 K range (regions between

orange and gray lines). The full protocol used for cooling is described in Appendix B.

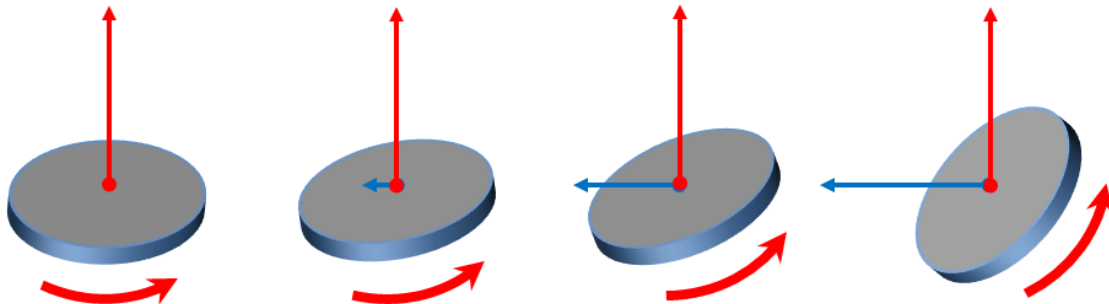
**Figure 7.4:** Dependence of particle temperature (a) and CCD intensity (b) on time. Grey and orange vertical lines show the times, when the CPL laser is turned off and on. Sphere and disk represent the chaotic spinning of the flake and the CPL stabilized spinning correspondingly.



## 7.2 Flake reorientation vs. DC stray fields

While spinning stabilization is important for particle cooling, one can go further by conducting measurements based on interplay between the induced spinning of the flake and the external DC fields. For high enough values of DC fields (at electrode

**Figure 7.5:** Schematic depiction of how the interaction between the CPL produced torque (red) and the patch fields torque (blue) is expected to lead to the reorientation of the flake rotation. Increase in the patch fields torque is assumed from left to right and would correspond to experimental case of moving away from the nulling settings.

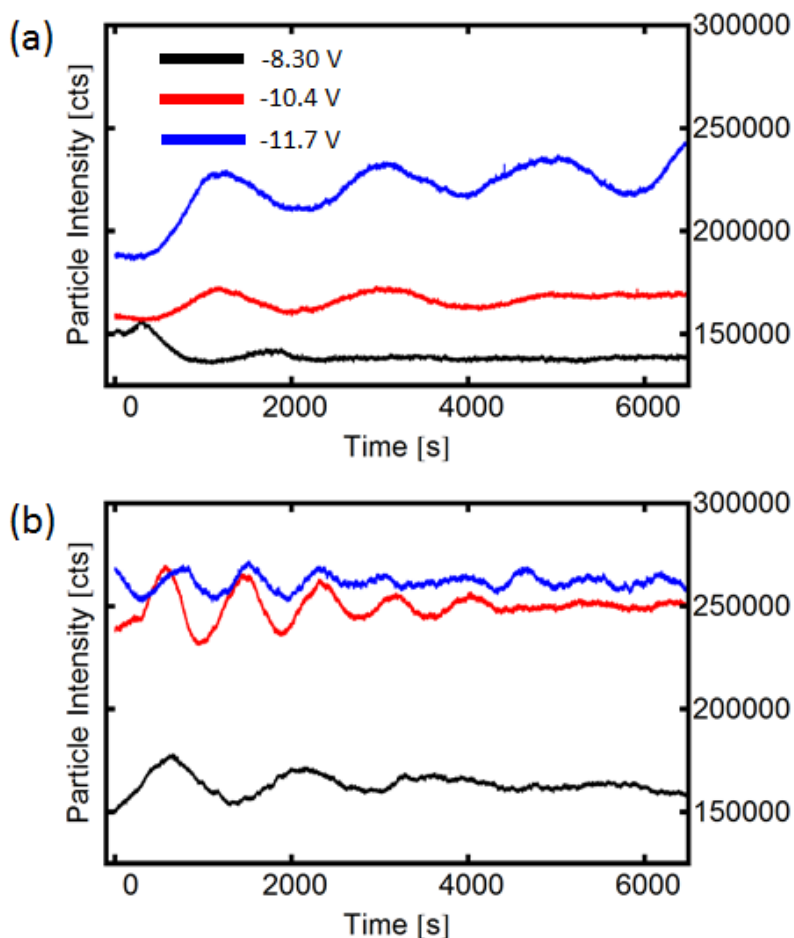


settings far from the nulling ones), the charged flake will start to experience the torque comparable with the torque produced by the circularly polarized light. This means that overall orientation of the flake will be different from the case of zero stray fields, and we can study the reorientation of the flake, including transient precession, by varying the electrode settings.

Based on the simple model of competing torques (See Fig. 7.5, where red and blue arrows represent torques created by the CPL and the patch fields correspondingly), we expect the spinning axis tilt to be dependent on the ratio of torques produced by laser light and the DC fields. Therefore, larger CPL power should make spinning less susceptible to the stray fields. This effect can be tested for by measuring particle intensity dependence on settings of one of the electrodes at different laser powers. Since the intensity of light scattered from the flake is dependent on its effective cross-section relative to the polarization plane of the light, the tilting of the flake spinning should be detectable via the CCD camera.

Due to the loss of the flake we used for the precession experiments, our data is

**Figure 7.6:** Comparison of transient behavior of particle intensity at CPL of (a) 245  $\mu\text{W}$  and (b) 145  $\mu\text{W}$ . Curves of the same color correspond to the switching to the same offset values.



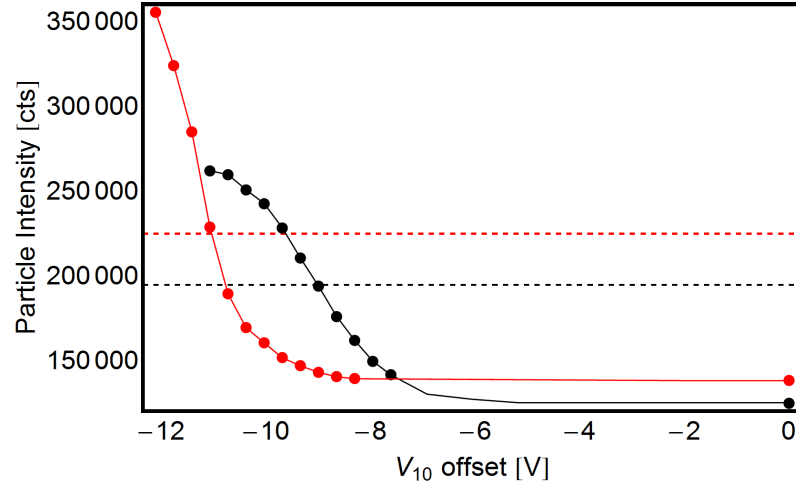
limited to only two values of circularly polarized light laser power – 145  $\mu\text{W}$  and 245  $\mu\text{W}$ . Also, while reproducible on two different days following venting and pumping down of the UHV chamber, the variation of the flake intensity was not observed at least on one occasion even while all parameters were set to be the same. The exact reason for this behavior is not clear, but the intensity locking/reorientation at high auxiliary electrodes settings was observed at two different particles and, for the same particle, on three different days separated in time. Hence, we do believe that the behavior observed and discussed below is general in nature, but more measurements

are required to get the full understanding of the dynamics involved.

Prior to the experiment, particle motion was stabilized with the CPL and cooled down at the nulling settings. For the particle prepared this way, voltage on an electrode  $V_{10}$  was changed in increments of -0.35 V every 6000 sec and two other electrodes were kept at their nulling values. For the electrode offset values below a threshold value of -7.8 V, no visible change of the intensity was observed (See Fig. 7.7). At higher values, a "delocking" of intensity and transient period of decaying oscillations were observed every time the DC offset was changed. These decaying oscillations are shown in Fig. 7.6 for  $V_{10}$  settings of -8.30 V (black line), -10.4 V (red line) and -11.7 V (blue line), where each curve is plotted from the moment the voltage  $V_{10}$  is set to the corresponding value. The intensity oscillations are assumed to be a sign of dampened precession, which is expected to happen when one of the torques acting on the flake is changed, where the torque changed in our case is the torque created by DC stray fields.

If we consider the values that the measured intensity settles to for each CPL power when the voltage  $V_{10}$  is changed from 0 to -12.8 V, the resulting plot shows some interesting features (See Fig. 7.7). As a reference, we show the values of the particle intensity (dashed lines) measured at 10 mTorr pressures, when no feedback is present and the particle spinning is highly chaotic and leads to averaging over all orientations of the flake. As expected, flake reorientation is observed depending on the DC settings and requires higher value of the offset, when larger circularly polarized light power is applied (compare red and black curves). At the same time, higher laser power led to bigger intensity growth with saturation at larger value, which we can not currently

**Figure 7.7:** Comparison of average intensity dependence on offset of  $V_{10}$  from nulling settings at CPL power of  $145 \mu\text{W}$  (black) and  $245 \mu\text{W}$  (red). Dashed lines represent the levels of intensity measured at 10 mTorr with no cooling at corresponding CPL power levels. Lines going through the data points are shown for a visual guidance.



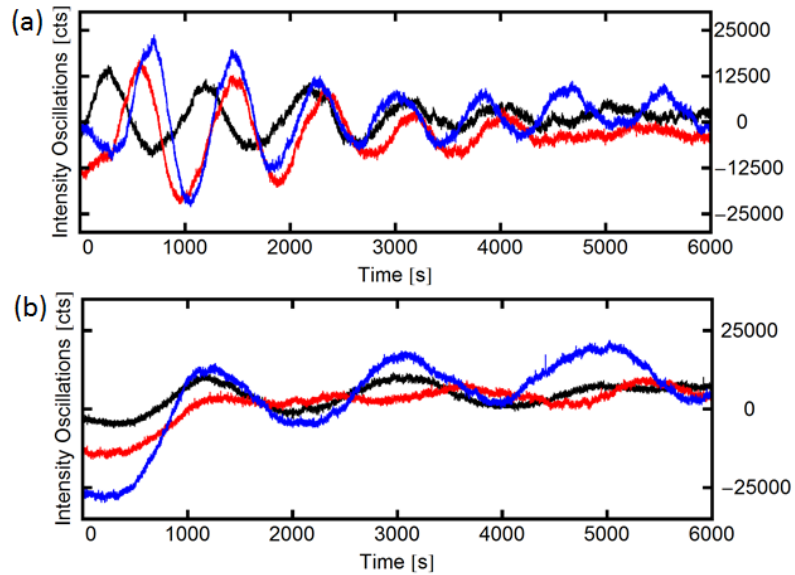
explain. No data is shown for  $V_{10}$  greater than  $-12.8 \text{ V}$ , because the particle was lost at the moment, when the offset was increased above that value.

Another effect we expect from the interaction of two torques is the dependence of the precession on the angular momentum of motion. In other words, for higher laser power, where higher spinning frequency is expected, we predict the longer precession period during the transient period. In Fig. 7.8 we show intensity oscillations at three different offset values at both laser powers. In the plots, the intensity is offset by the average value to make it easier to see that higher laser power indeed results in slower precession period [90].

### 7.2.1 Conclusions

We have presented preliminary data on particle reorientation and transient precession in the presence of patch fields. As expected, higher patch fields values lead to larger particle reorientation, while higher CPL powers make the particle less sus-

**Figure 7.8:** Transient oscillations of intensity observed at red laser power of (a) 145  $\mu\text{W}$  and (b) 245  $\mu\text{W}$ .



ceptible to the patch fields effect. More experiments are required to make any further conclusions, but the data collected allows one to speculate that a variety of experiments can be conducted based on the methods we have used.

### Particle characterization

---

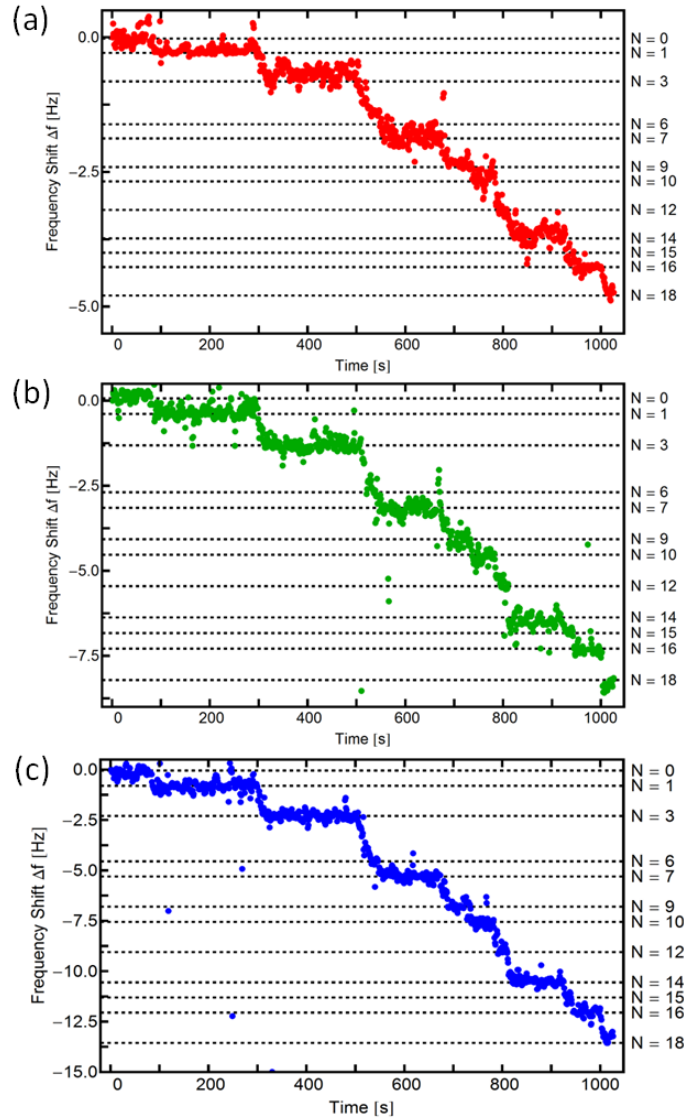
In the two previous chapters we concentrated our discussion on study of the particle motion, neglecting the question of what particles do we actually work on. While the solution we use creates graphene-like flakes, there is no easy way for us to check their mass, charge and shape - thickness and area. At the same time, these parameters are what defines how far we are from our goal - trapping and conducting experiments on single-layer graphene flakes. The following subsections show how we try to extract these numbers, with all of discussed data measured on the same particle as in previous chapters (101614A).

#### 8.1 Mass and charge extraction

Main complication in extracting absolute values of charge and mass of the flake is the way those parameters affect the equations of motion. Based on Newton's second law and linear dependence of electric force on charge, it is easy to see that only the

ratio of charge to mass matters (e.g. see Eq. 2.17). Therefore, a way to change either only mass or only charge of the particle is required for extraction of absolute values.

The most convenient measurement to use is the discharge sequence that was often observed at the beginning of pumping down the pressure for the first time. While the speed of discharge and its amount tend to change from flake to flake, the distinct jumps in eigenfrequencies were observed on different particles (see Fig. 8.1 for a discharge sequence for the particle 101614A). Here, the limitation of our FFT resolution is overcome by having enough data points per frequency peak to get a high accuracy position of the peaks with resolution of about 0.05 Hz. For fitting our data, we assume that only charge of the particle is changing during a discharge event, since it was observed that during all of discharge events, the frequency only decreased in value. As follows from formula for eigenfrequency 2.16, the only situation which can lead to this in HV is the particle discharge, because mass value is expected to either stay the same or decrease in HV conditions and this type of mass changes would correspond to increase of the frequency, behavior opposite to the observed one. Possible explanation for discharge events, based on the slow down in discharge observed, is the evaporation of the solution residue from the surface of the flake. If we use a single IPA molecule evaporation event to get an estimate on relative mass changes during the evaporation, the resulting mass change would be  $10^{-5} - 10^{-4}$  percent of the total particle mass for particle mass values of  $10^{18} - 10^{17}$  kg (typical values for the particles we trap). Therefore, mass stays close to constant if we consider the evaporation as a main source of frequency changes. By considering the mass of the flake constant during the discharge, we come to a conclusion that the distinct steps observed during

**Figure 8.1:** Dependence of frequency shift on time for  $f_x$  (a),  $f_y$  (b) and  $f_z$  (c)

the discharge correspond to the charge quantization [52] and can be used to extract the total charge of the flake. By assigning integer values to each of the discharge events, we fit the observed jumps in eigenfrequency to be equal to  $N\delta\omega$ , where  $\delta\omega$  is a minimal frequency change corresponding to  $\delta q = e$  [50, 53]. The  $\delta\omega$  serves as a parameter fit and  $N$  values shown on the right side of each of the plots in Fig. 8.1 are found based on the quantization fit. The absolute mass value can be expressed in

terms of minimum discharge event:

$$m_x = \alpha_x \frac{\delta q}{\delta \omega_x} \frac{V_{AC}^0}{\sqrt{2z_0^2 \Omega}}, \quad (8.1)$$

where similar equations can be written for  $m_y$  and  $m_z$  and the values found from each of the frequency sequences are expected to be equal to each other within the error margin (See Table 8.1). Since the main error of the fit comes from finding the value of  $\delta \omega$ , we estimate the error of the fit to be close to 2% (see subsection on reproducibility of the estimates), making three found values equal within the error margin as expected. Total charge of the particle can be estimated by using a ratio

**Table 8.1:** Particle mass estimation from the discharge sequence.

Direction	$\omega/2\pi$ (Hz)	$\delta\omega/2\pi$ (Hz)	Mass (kg)
X	290	0.265	$1.36 \times 10^{-17}$
Y	486	0.460	$1.42 \times 10^{-17}$
Z	731	0.750	$1.38 \times 10^{-17}$

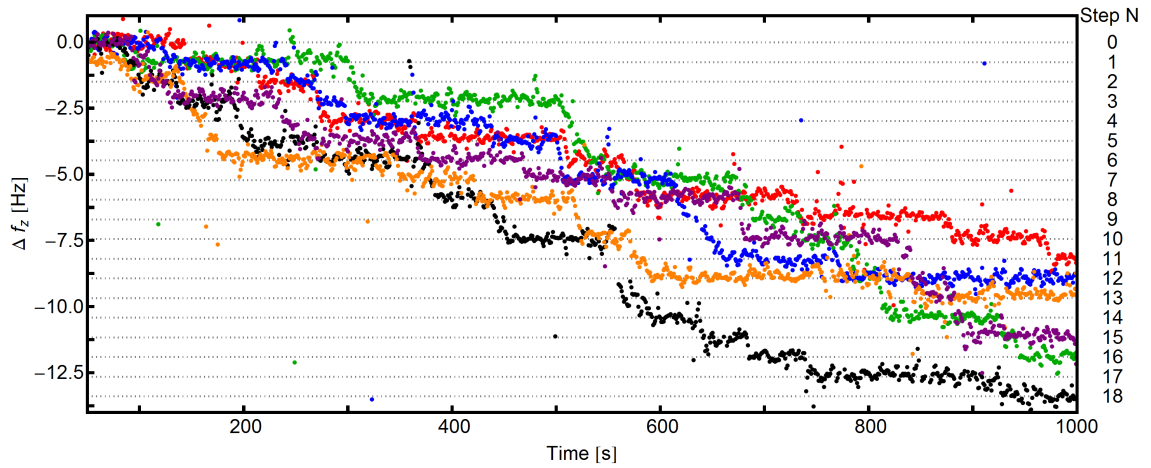
$\delta q/q = \delta \omega/\omega$  that is true in the assumption of the particle mass being constant. The charge value of  $q = +973e$  is calculated for the particle in question, giving  $q/m = 6.95 C/kg$ .

### 8.1.1 Reproducibility of charge and mass estimates

To check if the discharge technique provides a reproducible and accurate method for mass and charge extraction, we have collected six consecutive series of discharge data, each taken for a 1000 sec period. For each of the series the discharge step is calculated separately and the resulting variance in the  $\delta \omega_z$  was found to be equal to

$0.74 \pm 0.01$  Hz, proving the high accuracy of our method and giving a 2% error of the mass and charge estimation. A visual representation of the series is shown in Fig. 8.2, where one can see the overlap of plateaus for different series. The total time of 100 minutes is covered during this measurement, and no clear change in the values of the steps is observed, showing that constant mass approximation is a valid one to take.

**Figure 8.2:** Comparison of six (6) consecutive discharge series, used to independently extract the minimum frequency jump  $\delta\omega_z$ .



## 8.2 Alternative estimation of temperature

In this section we discuss an alternative method for temperature calibration, which relies on knowledge of the particle mass, as found via a discharge (see previous Section) or by any other means, and on using a fluctuation-dissipation theorem (FDT) to calculate the temperature of the flake in the thermalized state [91]:

$$\frac{k_B T_x}{2} = \frac{m \omega_x^2 \langle x^2 \rangle}{2}; \quad \frac{k_B T_y}{2} = \frac{m \omega_y^2 \langle y^2 \rangle}{2}; \quad \frac{k_B T_z}{2} = \frac{m \omega_z^2 \langle z^2 \rangle}{2}, \quad (8.2)$$

where  $T_x = T_y = T_z$  for thermalized motion. Since we measure particle motion in terms of signal  $S$ , we need to translate the signal  $S$  to the motion of the particle itself, where relationship between the displacement of the flake by  $X, Y, Z$  and the measured signal  $S$  is:

$$S = S_\delta \{Z \cos(54.7^\circ) + \sin(54.7^\circ)[X \cos(45^\circ) + Y \sin(45^\circ)]\}, \quad (8.3)$$

where  $S_\delta$  is the sensitivity of the signal  $S$  to the displacement of the particle image  $\delta R$  towards one of the photodetectors. Eq. 8.3 can be used to rewrite sensitivity of  $S$  as a sensitivity to motion along each of the axes:

$$S_x = S_\delta \sin(54.7^\circ) \cos(45^\circ) \quad (8.4)$$

$$S_y = S_\delta \sin(54.7^\circ) \sin(45^\circ) \quad (8.5)$$

$$S_z = S_\delta \cos(54.7^\circ), \quad (8.6)$$

where  $S_x = S_y = S_z = 0.578S_\delta$ , which is not surprising since the angle of rotation for our prism knifeedge was specifically chosen to make sensitivity of signal  $S$  the same for motion along all trap axes (See Fig. 3.7.b).

By rewriting average squared deviation in terms of power spectrum of signal  $S$  and by using FDT equations, we get:

$$T_{x,y,z} = \frac{m \omega_{x,y,z}^2}{k_B} \frac{2}{S_{x,y,z}^2} \int_{\omega_{x,y,z}-\delta\omega}^{\omega_{x,y,z}+\delta\omega} P_S(\omega) d\omega = \frac{m \omega_{x,y,z}^2}{k_B} \frac{2}{0.578^2 S_\delta^2} \int_{\omega_{x,y,z}-\delta\omega}^{\omega_{x,y,z}+\delta\omega} P_S(\omega) d\omega, \quad (8.7)$$

where range of integration  $2 \delta \omega$  is chosen to be wider than the spectrum peak width. We have included the prefactor of **2** since integration over a single peak in power spectrum  $P_S(\omega)$  gives only half of total energy, with the second part coming from an opposite peak at  $\omega = -\omega_{x,y,z}$ .

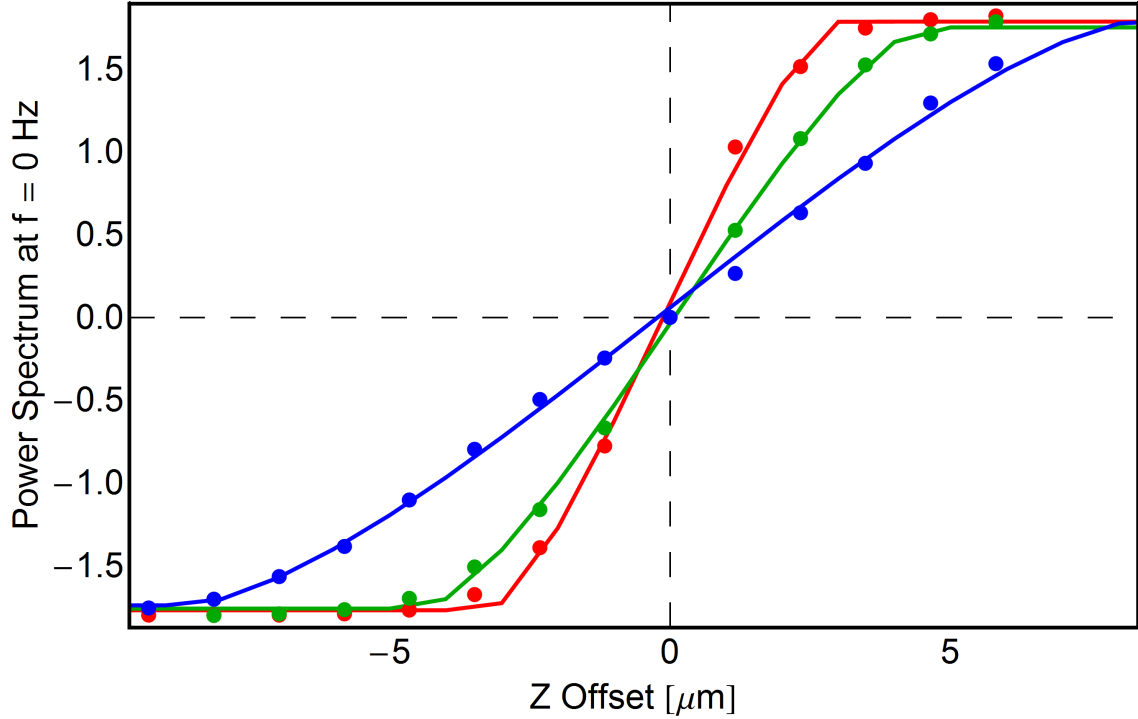
The key parameter to keep a track of, when trying to use this method for temperature estimation, is  $S_\delta$ , which depends on the focusing of the particle image and is hard to measure accurately. As can be seen in Fig. 8.3,  $S_\delta$  found by calculating the slope of signal response in the linear region of the curves, changes depending on the focusing of the flake from  $0.77/\mu m$  down to  $0.25/\mu m$ . High fit error and unclear relationship between the  $S_\delta$  that has to be measured at mTorr pressures and  $S_\delta$  of the particle in the cooled state, when the image size can shrink up to twice in size, lead us to believe that this method can be used only to check a general consistency of the experiment. Precise temperature measurements should be still conducted using the previously discussed calibration technique (Chapter 6).

### 8.3 Discussion of the flake shape

Particle size and shape are not measurable directly for levitated flakes and their discussion is open to some speculation, but we can still try to estimate the number of layers in the flake based on modelling the graphene flake as a solid disk. While this model is very crude, it helps us to get a sense of how far the flakes we trap are from the monolayer ones.

Since we are discussing very crude estimates, we consider our flake to have a maximum size of about  $3\text{-}4 \mu$ , value based on the smallest size of CCD camera image we

**Figure 8.3:** Comparison of dependence of  $P_S(\omega = 0)$  on particle displacement along  $Z$  at three different focusing settings.



could see, when camera plane was right at the focusing plane of the lens. Granted that this is almost definitely an overestimate, it gives us only a lower boundary on the flake thickness, since smaller flakes of the same mass would have to be correspondingly thicker. By using density of the graphene monolayer  $\rho_{grph} = 7.37 \times 10^{-7} \text{ kg/m}^2$  and distance between graphene layers of  $r_{layer} = 0.335 \text{ nm}$  [57], we get an estimate for number of layers in the flake we look at (101614A):

$$N_{layers} = \frac{m}{\rho_{grph} \pi r^2 r_{layer}} > \sim 10. \quad (8.8)$$

Therefore, the particle we have studied is definitely not the single-layered flake, but it is still a highly non-spherical one (as can be seen from intensity change in Fig. 7.7).

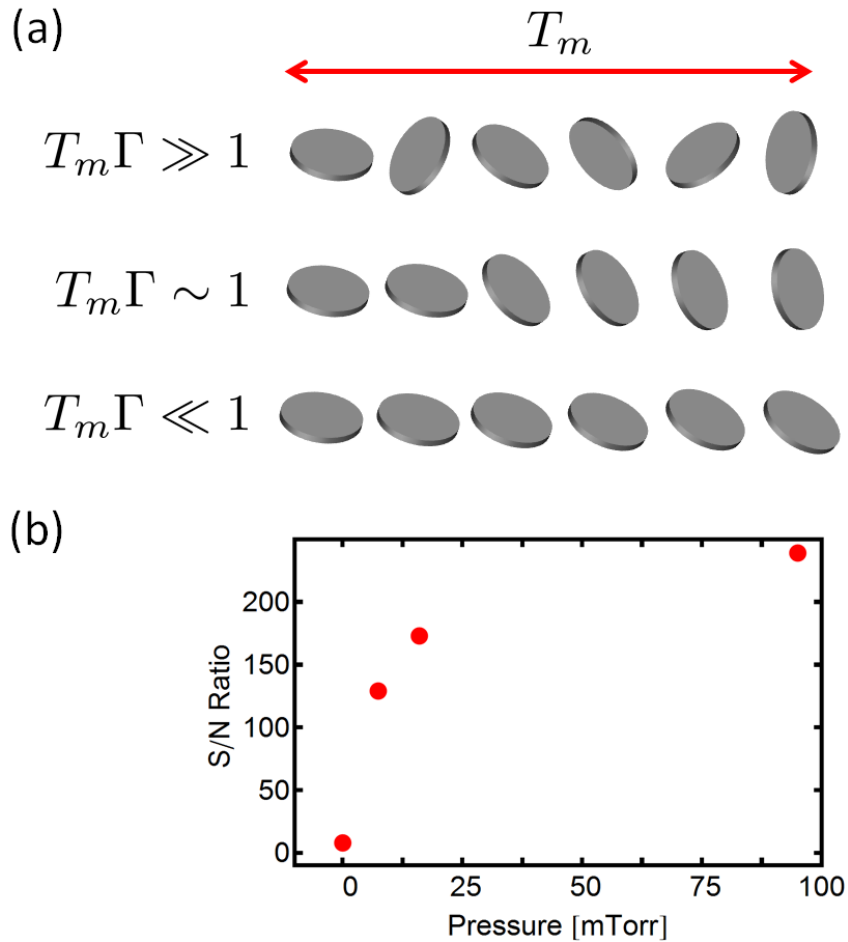
### 8.3.1 Dependence of S/N ratio in CCD intensity on pressure

Another way to get an insight into the flake shape is by studying the amount of light scattered from the flakes, which is dependent on the flake rotation angle [92]. This measurement was done via photcounter set to an averaging time of 1 second and gave an average count number of 20000 for the data discussed below (this particle was different from the particle 101614A).

For high enough pressures the ambient gas molecules hit the flake from all directions leading to an effective averaging of the flake orientation, making it "resemble" a sphere as long an averaging time  $T_m$  longer than one over the damping ratio  $\Gamma$  is chosen (corresponding to the case of  $T_m\Gamma \gg 1$  as shown in Fig. 8.4.a). As we know, signal to noise ratio for a discrete signal is proportional to  $\sqrt{N}$  ( $N$  is a an events number), meaning that if our particle was a pure sphere, the signal to noise ratio would be the same independent on the pressure. On the other hand, once the pressure level is decreased low enough to make relaxation processes longer than the averaging times (regime  $T_m\Gamma \sim 1$  as shown in Fig. 8.4.a), the particle reorientation will start to show itself in the signal. In this transient regime, signal to noise ratio is expected to go down since the amount of scattered light will fluctuate based on the reorientation of the flake. Therefore, if signal to noise ratio dependence on pressure is expected in the regime, where crossover between  $T_m\Gamma \gg 1$  and  $T_m\Gamma \sim 1$  happens, we should see a monotonically decreasing curve. This can be indeed confirmed by starting the measurement of the particle brightness at pressures of 100 mTorr and going down to pressures  $10^{-6}$  Torr (See Fig. 8.4.b). Observed behavior proves that the trapped

particles have a non-spherical shape.

**Figure 8.4:** (a) Schematic representation of the particle reorientation during the photcounter averaging at different regimes, corresponding to different ratios between the damping  $\Gamma$  and the measurement time  $T_m$ . (b) Dependence of the signal to noise ratio of the photocount number on the pressure.



### Conclusions and future work

---

#### 9.1 Conclusions

##### 9.1.1 Cooling and stabilization

In conclusion, we have presented data proving that the parametric feedback scheme implemented in our experiment has stabilized and cooled down the particle motion in high vacuum (Chapter 6). Cooling of center of mass motion to temperatures below 20 K has been routinely observed, and trapping time longer than a few days has been achieved.

It was found that cooling of the flake is strongly dependent on presence of the CPL, required for spinning stabilization of the flake. In the absence of the CPL, chaotic spinning and reorientation of the flake produced enough noise to limit the cooling temperatures to about 100 K, while as long as high enough CPL power was applied,

same feedback parameters produced the temperature of about 20 K.

The results on cooling and its dependence on the DC stray fields as well as the discussion of the flake charge and mass were written in the paper [93].

### 9.1.2 Effect of DC stray fields on cooling

The coupling of the feedback noise in the presence of the DC patch fields has been studied (Chapter 7), where the importance of nulling the patch fields acting on the flake was shown. The nulling was done by using a set of auxiliary electrodes. The electrodes' settings corresponding to the completely cancelled patch fields were found by minimizing the response of the particle motion to an amplitude modulation at frequencies close to the particle eigenfrequencies. We have checked that the nulling of the fields is necessary for keeping the flake in the trap at HV, with overheating and escape of the flakes observed if no fields nulling was done prior to the cooling procedure.

Therefore, we believe that proper protocol for further experiments on the levitated flakes (including testing their stability in UHV) requires both nulling of DC stray fields and the presence of the CPL. In regard to the nulling configuration of the electrodes, its recalibration *in situ* can become necessary due to stray fields drifts, when the experiments on a time scale longer than a few days are to be conducted. At the same time, smaller length experiments with time scale of one or two days should not require any significant readjustment of the voltage values.

### 9.1.3 Particle characterization

Characterization of the flake 101614A in terms of absolute values of its charge and mass was done by calibrating an observed discharge sequence quantization (Chapter 8), giving  $m = 1.4 \times 10^{-17}$  kg and charge  $q = +973 e$ . For the FFT resolution (2048 frequency bins at frequency range of 0-1000 Hz) used in the experiments, we estimate that the discharge quantization should be detectable for flakes with mass to charge ratios higher than 1.75 C/kg. If flakes with lower charge over mass ratio were to be studied, FFT acquisition has to be probably rewritten with a higher frequency resolution.

### 9.1.4 Particle precession : preliminary data

Preliminary data on interaction of the torques created by CPL and DC stray fields was presented in the second part of Chapter 7. We have observed that cooled down and spinning-stabilized flakes reorient in the presence of the non-zero DC fields and the amount of their reorientation depends on the CPL power and the DC offset values relative to the nulling settings. While not enough data is present to have a meaningful fitting to a theoretical model, we believe that basic behavior of reorientation and dampened precession can be explained in terms of the spinning object under the influence of an external torque. Typical frequency of the intensity oscillations during the initial precession, right after the DC offset on auxiliary electrodes was changed, was observed and had a mHz scale, with oscillations taking a few hours to completely decay.

Although the precession and flake reorientation data presented in Chapter 7 was taken only for the particle 101614A, a similar behavior was observed on at least two more particles. Therefore, we think that this kind of measurements can be used for study of non-equilibrium dynamics of the flakes, if a better consistency in the flakes' shape and charge over mass ratio is achieved.

## 9.2 Future work

First, we discuss the possible directions that do not require any significant modification of the experimental setup or reprogramming of an FPGA. By collecting more data on precession and reorientation of the flake, it would be interesting to see how well the observed behavior is explained by basic model of a solid spinning disk. As a goal, the relationship between the spinning axis and the DC offsets can be studied and, if calibrated, would mean a full control over all degrees of freedom of the flake - motion of its center of mass in the trap and spinning around an arbitrarily oriented axis. Full control of particle motion would benefit any study requiring a specific orientation of the flake, e.g. molecular deposition.

Similarly, no change in the setup is required for study of graphene folding, the effect predicted to be observed for any 2D material due to thermal fluctuations if no opposing forces are present [5]. While in regular experiments on graphene, the main constraints are either the boundary near the suspended graphene or the graphene substrate, in our experiment the folding is prevented due to the net charge present on the flake and due to the flake spinning. Therefore, one can envision an experiment during which the discharge of the flake is initiated via exposing it to high enough laser power

or to an electron gun beam (already installed in the UHV chamber). If one were to keep trap frequency in the stable trapping regime (see Eq. 2.21) during the discharge, we expect an observation of transition of the flake from a spinning sheet to the folded state, the effect that can be measured via tracking the ratio between the maximum and minimum values of the flake intensity at different DC offset levels.

While our flakes are too large for macroscopic quantum experiments, with nK temperatures required for our particles, achieving maximum cooling of the center of mass motion is still important. Here, the current record of cooling to 15 K can be improved on by changing the feedback bandwidth, using photodectors with lower noise level or increasing the laser power used in experiments.

Another possible direction to take is by changing to faster analog digital converters (ADC), where (see Chapter 5) the issue of slow analog-digital conversion limits the highest frequency that can be cooled down by the FPGA feedback. Getting faster ADC can widen the range of accessible frequencies, which could be a necessary step to take once smaller/thinner flakes are studied and charge to mass ratio becomes large enough for eigenfrequencies to be greater than the currently used cut-off frequency of 2 kHz.

The FPGA circuitry can be rewritten as well by either replacing the product based feedback loop with a phase-lock loop (PLL) feedback or by adding a PLL setup for an additional control. Switching to PLL will decrease the feedback bandwidth, which would result in decreased noise coupling to the feedback. This can be necessary as well, since lower reflectivity of the smaller/thinner flakes means lower signal to noise ratio, which in turn makes cooling less efficient. Programming three independent

---

PLLs (one per eigenfrequency) with tracing frequency centers should be implemented in this approach with a separate feedback gain for each of the motion directions. The center frequency tracing capability is crucial for avoiding delocking of the PLL signal when an intentional or unintentional change of the eigenfrequencies occurs as a result of evaporation of volatiles, flake breaking or some residue deposition. At the same time, the implementation of PLL can be delayed or found not necessary if future experiments show that laser powers higher than 10-20 mW can be applied to the flakes without losing the whole charge on flakes.

## Appendix A: Electric fields nulling

Stray fields nulling is based on the fact that if the trap minimum is not in the stray fields' nulling point, there is a residue interaction between the particle and those fields. This interaction is picked up by applying an amplitude modulation (AM) to the trap potential. As long as AM frequency is close to one of the three eigenfrequencies of motion, corresponding mode would be affected. By measuring particle response with a lock-in at different electrode voltage settings, one can map the stray fields and find their minimum.

1. Check that RHK HVA is on [all red lights should be on during operation] and all the BNC cables are properly connected.
2. Check that lock-in oscillation amplitude is set to 1V for both lock-ins and that both lock-ins show "LOCKED" on the display. Make sure that neither of lock-ins' "INPUT OVERLOAD" signs is flickering since that will lead to inaccuracy in the procedure. Decreasing lock-ins' sensitivity or signal level by lowering the green laser power should be enough to stop the overload.
3. Set AM modulation to 15-25 %.
4. Set, electrode voltages to [-1, -1, -4] or the previously found electrodes' configu-

- ration. Shift electrodes' settings by  $[-1, 0, 0]$  (easiest way to do this is by setting corresponding offsets in VI program to be -1, 0 and 0). Make sure that piezo-voltage stays within the range every time you change the voltages on electrodes.
5. Check values of eigenfrequencies either by looking at FFT spectrum on the VI plot or on spectrum analyzer located next to the lock-ins.
  6. For each of the eigenfrequencies, measure the X component of lock-in response (it provides you with combined information of phase and amplitude) to modulation at frequency set to be lower than the eigenfrequency by 50 Hz. You have measured response of X, Y and Z harmonics to the AM modulation. NOTE: X and Y harmonics have a weak dependence on the voltage settings, but Z harmonic shifts by up to 100-200 Hz and thus requires more attention in keeping response measurements consistent (trying to stay at a similar distance from the eigenfrequency peak).
  7. Repeat the procedure by shifting electrodes' voltages by  $[0, -1, 0]$ ,  $[0, 0, -1]$  and  $[1, 0, 0]$ ,  $[0, 1, 0]$  and  $[0, 0, 1]$ . NOTE: taking 6 points to fit 4 point curves (we expect close to linear dependence of lock-in response to voltages and therefore have 4 fitting parameters to extract) is an oversampling, but improves a convergence of the procedure and seems to be necessary due to high noise of the signal.
  8. Use fitting in Mathematica or any convenient program to find the voltage settings that null the lock-in response [Fit is done assuming linear dependence of

response on voltages:  $Response = a V_{10} + b V_2 + c V_6 + d$ ].

9. Check the response of lock-ins at the newly found settings. If it is non-zero within the noise range, repeat the nulling procedure again using new voltage settings as a starting point.
10. After nulling settings are found, don't forget to set lock-in amplitudes back to zero.

## Appendix B: Cooling and stabilization protocol

1. Check that green laser power is set high enough to see the photocurrent of about 0.3-0.5 or higher  $\mu\text{A}$  (noise level is about 0.06  $\mu\text{A}$ ). At higher photocurrent levels, particles tend to start discharging, effect that can be used for charge and mass calibration.
2. If the particle is discharging even at a photocurrent of 0.3  $\mu\text{A}$  (all the eigenfrequencies go down with time) and discharge doesn't slow down over a large period of time (30-60 minutes), try lowering the laser power even more. If the discharge doesn't stop at that point, changing the particle could be required.
3. Due to digital delay and digital filters used in the signal processing, only frequencies in the range of 100-2000 Hz are efficiently cooled. Check that all three of the eigenfrequencies are within the range between 150 and 1300 Hz. If those frequencies are out of the range, adjust trap frequency correspondingly (increasing frequency will lower eigenmodes and vice versa).
4. Make sure that the right sign for feedback product is set in the virtual instrument (VI). It should be set to PLAIN PRODUCT for AM modulation (INVERSE PRODUCT is used for FM modulation).

5. Set AM modulation to 30 % and slowly open the turbopump valve.
6. When pressure gauge reading drops below 1-3 mTorr, set product gain value to 20 and open turbopump valve all the way. As soon as pressure gets lower than  $10^{-5} - 10^{-6}$  Torr, you will observe particle cooling (peaks in Fast-Fourier Transform (FFT) of the signal will start to go down and get close to noise level, size of the particle visible in CCD camera will decrease). If no cooling is observed and particle motion gets too big in one of the directions, stop pumping by closing the turbopump valve and check all the settings.
7. Accuracy of the fields nulling can be confirmed/checked at this point:
  - Make sure that intensity fluctuations are small enough for the efficient cooling. If not, refer to intensity stabilization with a red laser procedure.
  - Vary electrode voltages by increments of 0.1 (setting offset to the number desired) and keep the track of temperature for each of three eigenfrequencies. You expect to see the minimum in cooling when offsets from the chosen electrodes settings are equal to zero. If that is not the case, the renulling of the fields is required.

### B.1 Damping of intensity fluctuations via CPL

Fluctuations in the integral intensity are observed for cooled asymmetric particles. These oscillations limit the effectiveness of the cooling and lead to the oscillations of the piezofeedback voltage as well. Red circularly polarized light (CPL) is used in order to stabilize spinning of the particle along the fixed axis.

- (a) Turn on red laser at a very low set point (0.003). Wait till red laser supply starts working.
- (b) Once red laser is on, check that you can see its reflection on the ceiling/-going through the top window of the UHV chamber. If you don't see it, the laser is probably misaligned and red laser mirror' position has to be readjusted.
- (c) Keep raising red laser power in small increments, waiting about 4-5 minutes in between (transient period for damping fluctuations at a sufficient laser level) until damping of the oscillations is observed.
- (d) If fluctuations do not go away over a long period of time (20-30 minutes), check that stray voltages are properly nulled. Even large red laser power could be not enough to stabilize intensity at incorrectly nulled stray fields.

## Bibliography

- [1] K. S. Novoselov, A. K. Geim, and S. V. Morozov. Electric field effect in atomically thin carbon films. *Science*, 306:666, 2004. (Cited on page [1](#).)
- [2] Sheneve Z. Butler, Shawna M. Hollen, Linyou Cao, Yi Cui, Jay A. Gupta, Humberto R. Gutiérrez, Tony F. Heinz, Seung Sae Hong, Jiaying Huang, Ariel F. Ismach, Ezekiel Johnston-Halperin, Masaru Kuno, Vladimir V. Plashnitsa, Richard D. Robinson, Rodney S. Ruoff, Sayeef Salahuddin, Jie Shan, Li Shi, Michael G. Spencer, Mauricio Terrones, Wolfgang Windl, and Joshua E. Goldberg. Progress, challenges, and opportunities in two-dimensional materials beyond graphene. *ACS Nano*, 7(4):2898–2926, 2013. PMID: 23464873. (Cited on pages [1](#), [2](#), and [3](#).)
- [3] A. K. Geim and I.V. Grigorieva. Van der Waals heterostructures. *Nature*, 499:419 – 425, 2013. (Cited on pages [1](#) and [2](#).)
- [4] R. E. Peierls. Quelques propriétés des corps solides. *Ann. Inst. Henri Poincaré*, 5:177, 1935. (Cited on page [1](#).)
- [5] L. D. Landau. Theory of phase transformations. I. *Phys. Z. Sowjetunion*, 11:26, 1937. (Cited on pages [1](#), [79](#), and [119](#).)
- [6] Yuanbo Zhang, Joshua P. Small, William V. Pontius, and Philip Kim. Fabrication and electric-field-dependent transport measurements of mesoscopic graphite devices. *Applied Physics Letters*, 86(7), 2005. (Cited on page [1](#).)
- [7] Xuesong Li, Weiwei Cai, Jinho An, Seyoung Kim, Junghyo Nah, Dongxing Yang, Richard Piner, Aruna Velamakanni, Inhwa Jung, Emanuel Tutuc, Sanjay K. Banerjee, Luigi Colombo, and Rodney S. Ruoff. Large-area synthesis of high-quality and uniform graphene films on copper foils. *Science*, 324(5932):1312–1314, 2009. (Cited on page [1](#).)
- [8] Wataru Norimatsu and Michiko Kusunoki. Epitaxial graphene on SiC{0001}: advances and perspectives. *Phys. Chem. Chem. Phys.*, 16:3501–3511, 2014. (Cited on page [1](#).)

- [9] K. S. Novoselov, V. I. Fal'ko, L. Colombo, P. R. Gellert, M. G. Schwab, and K. Kim. A roadmap for graphene. *Nature*, 490(7419):192–200, 2012. (Cited on page 2.)
- [10] Patrick Vogt, Paola De Padova, Claudio Quaresima, Jose Avila, Emmanouil Frantzeskakis, Maria Carmen Asensio, Andrea Resta, Bénédicte Ealet, and Guy Le Lay. Silicene: Compelling experimental evidence for graphenelike two-dimensional silicon. *Phys. Rev. Lett.*, 108:155501, Apr 2012. (Cited on page 2.)
- [11] D.C. Elias, R. R. Nair, T. M. G. Mohiuddin, S. V. Morozov, P. Blake, M. P. Halsall, A. C. Ferrari, D. W. Boukhvalov, M. I. Katsnelson, A. K. Geim, and K. S. Novoselov. Control of graphene's properties by reversible hydrogenation: Evidence for graphane. *Science*, 323(5914):610 – 613, 2009. (Cited on page 2.)
- [12] Elisabeth Bianco, Sheneve Butler, Shishi Jiang, Oscar D. Restrepo, Wolfgang Windl, and Joshua E. Goldberger. Stability and exfoliation of germanane: A germanium graphane analogue. *ACS Nano*, 7(5):4414–4421, 2013. PMID: 23506286. (Cited on page 2.)
- [13] Yoshihiko Arita, Michael Mazilu, and Kishan Dholakia. Laser-induced rotation and cooling of a trapped microgyroscope in vacuum. *Nature Communications*, 4:2374, January 2013. (Cited on pages 3, 6, 21, and 79.)
- [14] Eduardo V. Castro, H. Ochoa, M. I. Katsnelson, R. V. Gorbachev, D. C. Elias, K. S. Novoselov, A. K. Geim, and F. Guinea. Limits on charge carrier mobility in suspended graphene due to flexural phonons. *Physical Review Letters*, 105(26):266601, December 2010. (Cited on page 3.)
- [15] S. V. Morozov, K. S. Novoselov, M. I. Katsnelson, F. Schedin, D. C. Elias, J. A. Jaszczak, and A. K. Geim. Giant intrinsic carrier mobilities in graphene and its bilayer. *Phys. Rev. Lett.*, 100:016602, Jan 2008. (Cited on page 3.)
- [16] L. Lindsay, D. A. Broido, and Natalio Mingo. Flexural phonons and thermal transport in graphene. *Phys. Rev. B*, 82:115427, Sep 2010. (Cited on page 3.)
- [17] J. H. Los, K. V. Zakharchenko, M. I. Katsnelson, and Annalisa Fasolino. Melting temperature of graphene. *Phys. Rev. B*, 91:045415, Jan 2015. (Cited on page 3.)
- [18] Klaus Kroy. Levitating nanoparticles: Non-equilibrium nano-thermometry. *Nature Nanotechnology*, 9(6):415–417, 2014. (Cited on page 3.)
- [19] Jan Gieseler, Roman Quidant, Christoph Dellago, and Lukas Novotny. Dynamic relaxation of a levitated nanoparticle from a non-equilibrium steady state. *Nature Nanotechnology*, 9:358 – 364, 2014. (Cited on pages 3, 7, and 89.)
- [20] Jan Gieseler, Marko Spasenović, Lukas Novotny, and Romain Quidant. Thermal nonlinearities in a nanomechanical oscillator. *Nature Physics*, 9:806 – 810, Jul 2013. (Cited on pages 3 and 34.)

- [21] Yonggun Jun, Momčilo Gavrilov, and John Bechhoefer. High-precision test of Landauer's principle in a feedback trap. *Phys. Rev. Lett.*, 113:190601, Nov 2014. (Cited on page 3.)
- [22] Tongcang Li, Simon Kheifets, David Medellin, and Mark G. Raizen. Measurement of the instantaneous velocity of a Brownian particle. *Science*, 328(5986):1673–1675, 2010. (Cited on pages 4 and 7.)
- [23] Ninghai Su, Miao Liu, and Feng Liu. Chemical versus thermal folding of graphene edges. *Nano Research*, 4(12):1242–1247, 2011. (Cited on page 4.)
- [24] Verónica Barone, Oded Hod, and Gustavo E Scuseria. Electronic structure and stability of semiconducting graphene nanoribbons. *Nano Letters*, 6(12):2748–54, December 2006. (Cited on page 4.)
- [25] Ksenia V. Bets and Boris I. Yakobson. Spontaneous twist and intrinsic instabilities of pristine graphene nanoribbons. *Nano Research*, 2(2):161–166, 2009. (Cited on page 4.)
- [26] C. Cocchi, D. Prezzi, and A. Ruini. Electronics and optics of graphene nanoflakes: edge functionalization and structural distortions. *J. Phys. Chem. C*, 116(33):17328 – 17335, 2012. (Cited on page 4.)
- [27] Vasilios Georgakilas, Michal Otyepka, Athansios B. Bourlinos, Vimlesh Chandra, Namdong Kim, Christian Kemp, Pavel Hobza, Radek Zboril, and Kwang S. Kim. Functionalization of graphene: covalent and non-covalent approaches, derivatives and applications. *Chemical Reviews*, 112(11):6156 – 6214, 2012. (Cited on page 4.)
- [28] Alexander Kuhlicke, Antonio Rylke, and Oliver Benson. On-demand electrostatic coupling of individual precharacterized nano- and microparticles in a segmented paul trap. *Nano Letters*, 15(3):1993–2000, 2015. PMID: 25688754. (Cited on page 4.)
- [29] R. F. Wuerker, H. Shelton, and R. V. Langmuir. Electrodynamic containment of charged particles. *Journal of Applied Physics*, 30:342–349, 1959. (Cited on page 5.)
- [30] Pradip K. Ghosh. *Ion Traps*. Oxford University Press, 1st edition, 1995. (Cited on pages 5, 16, 17, and 19.)
- [31] C. E. Pearson, D. R. Leibbrandt, W. S. Bakr, W. J. Mallard, K. R. Brown, and I. L. Chuang. Experimental investigation of planar ion traps. *Phys. Rev. A*, 73:032307, Mar 2006. (Cited on page 5.)
- [32] Robert Maiwald, Dietrich Leibfried, Joe Britton, James C. Bergquist, Gerd Leuchs, and David J. Wineland. Stylus ion trap for enhanced access and sensing. *Nature Physics*, 5(8):551–554, June 2009. (Cited on pages 5, 29, and 31.)

- [33] H. C. Nägerl, D. Leibfried, H. Rohde, G. Thalhammer, J. Eschner, F. Schmidt-Kaler, and R. Blatt. Laser addressing of individual ions in a linear ion trap. *Phys. Rev. A*, 60:145–148, Jul 1999. (Cited on page 5.)
- [34] Alexander Kuhlicke, Andreas W. Schell, Joachim Zoll, and Oliver Benson. Nitrogen vacancy center fluorescence from a submicron diamond cluster levitated in a linear quadrupole ion trap. *Applied Physics Letters*, 105(7):073101, 2014. (Cited on page 5.)
- [35] D. J. Berkeland, J. D. Miller, J. C. Bergquist, W. M. Itano, and D. J. Wineland. Minimization of ion micromotion in a Paul trap. *Journal of Applied Physics*, 83(10):5025–5033, 1998. (Cited on pages 5 and 11.)
- [36] A. Ashkin. Acceleration and trapping of particles by radiation pressure. *Phys. Rev. Lett.*, 24:156–159, Jan 1970. (Cited on page 5.)
- [37] A. Ashkin and J. M. Dziedzic. Optical levitation in high vacuum. *Applied Physics Letters*, 28(6), 1976. (Cited on page 5.)
- [38] A. Ashkin and J. M. Dziedzic. Optical trapping and manipulation of viruses and bacteria. *Science*, 235:1517 – 1520, 1987. (Cited on page 5.)
- [39] Z.-Q. Yin, A. A. Geraci, and T. Li. Optomechanics of levitated dielectric particles. *Int. J. Mod. Phys. B*, page 1330018, 2013. (Cited on pages 5 and 6.)
- [40] Onofrio M. Maragò, Philip H. Jones, Pietro G. Gucciardi, Giovanni Volpe, and Andrea C. Ferrari. Optical trapping and manipulation of nanostructures. *Nature Nanotechnology*, 8(11):807–19, November 2013. (Cited on page 6.)
- [41] Tongcang Li, Simon Kheifets, and Mark G. Raizen. Millikelvin cooling of an optically trapped microsphere in vacuum. *Nature Physics*, 7(7):527–530, March 2011. (Cited on page 6.)
- [42] Nikolai Kiesel, Florian Blaser, Uroš Deliċ, David Grass, Rainer Kaltenbaek, and Markus Aspelmeyer. Cavity cooling of an optically levitated submicron particle. *Proceedings of the National Academy of Sciences*, 110(35):14180–14185, 2013. (Cited on page 6.)
- [43] Peter Asenbaum, Stefan Kuhn, Stefan Nimmrichter, Ugur Sezer, and Markus Arndt. Cavity cooling of free silicon nanoparticles in high vacuum. *Nature Communications*, 4:2743, November 2013. (Cited on page 6.)
- [44] Jan Gieseler, Bradley Deutsch, Romain Quidant, and Lukas Novotny. Subkelvin parametric feedback cooling of a laser-trapped nanoparticle. *Physical Review Letters*, 109(10):103603, September 2012. (Cited on pages 6, 9, and 75.)
- [45] Zhang Qi Yin, Tongcang Li, Xiang Zhang, and L. M. Duan. Large quantum superpositions of a levitated nanodiamond through spin-optomechanical coupling. *Physical Review A - Atomic, Molecular, and Optical Physics*, 88(3):1–6, 2013. (Cited on page 6.)

- [46] Jasper Chan, T. P. Mayer Alegre, Amir H. Safavi-Naeini, Jeff T. Hill, Alex Krause, Simon Gröblacher, Markus Aspelmeyer, and Oskar Painter. Laser cooling of a nanomechanical oscillator into its quantum ground state. *Nature*, 478(7367):89–92, October 2011. (Cited on page 6.)
- [47] Andreas Albrecht, Alex Retzker, and Martin B. Plenio. Testing quantum gravity by nanodiamond interferometry with nitrogen-vacancy centers. *Phys. Rev. A*, 90:033834, Sep 2014. (Cited on page 6.)
- [48] Oliver Krauß and Gerhard Wurm. Radiation pressure forces on individual micron-size dust particles: a new experimental approach. *J. Quant. Spectrosc. Radiat. Transfer*, 89:179–189, 2004. (Cited on page 6.)
- [49] Andrew A. Geraci, Scott B. Papp, and John Kitching. Short-range force detection using optically cooled levitated microspheres. *Phys. Rev. Lett.*, 105:101101, Aug 2010. (Cited on page 6.)
- [50] David C. Moore, Alexander D. Rider, and Giorgio Gratta. Search for millicharged particles using optically levitated microspheres. *Phys. Rev. Lett.*, 113:251801, Dec 2014. (Cited on pages 6 and 108.)
- [51] M. Grimm, B. Langer, S. Schlemmer, T. Lischke, U. Becker, W. Widdra, D. Gerlich, R. Flesch, and E. Rühl. Charging mechanisms of trapped element-selectively excited nanoparticles exposed to soft X-rays. *Phys. Rev. Lett.*, 96:066801, Feb 2006. (Cited on page 7.)
- [52] Stephan Schlemmer, Jens Illema, Stefan Wellert, and Dieter Gerlich. Non-destructive high-resolution and absolute mass determination of single charged particles in a three-dimensional quadrupole trap. *Journal of Applied Physics*, 90(10):5410–5418, 2001. (Cited on pages 7 and 108.)
- [53] David M. Bell, Collin R. Howder, Ryan C. Johnson, and Scott L. Anderson. Single CdSe/ZnS nanocrystals in an ion trap: Charge and mass determination and photophysics evolution with changing mass, charge, and temperature. *ACS Nano*, 8(3):2387–2398, 2014. (Cited on pages 7 and 108.)
- [54] J. Millen, T. Deesuan, P. Barker, and J. Anders. Nanoscale temperature measurements using non-equilibrium Brownian dynamics of a levitated nanosphere. *Nature Nanotechnology*, 9(6):425–9, 2014. (Cited on pages 7 and 9.)
- [55] Mo Yang, John M. Dale, William B. Whitten, and J. Michael Ramsey. Laser desorption mass spectrometry of a levitated single microparticle in a quadrupole ion trap. *Analytical Chemistry*, 67(6):1021–1025, March 1995. (Cited on page 7.)
- [56] B. E. Kane. Levitated spinning graphene flakes in an electric quadrupole ion trap. *Physical Review B*, 82(11):115441, September 2010. (Cited on pages 7, 8, 30, and 47.)

- [57] Steven Cranford, Dipanjan Sen, and Markus J. Buehler. Meso-origami: Folding multilayer graphene sheets. *Applied Physics Letters*, 95(12), 2009. (Cited on pages 7 and 113.)
- [58] W. L. Harries and D. Dimock. Levitation and stabilization of a single particle by use of negative feedback. *Review of Scientific Instruments*, 43(8), 1972. (Cited on page 9.)
- [59] Robert A. Millikan. On the elementary electric charge and the Avogadro constant. *Physical Review*, 2(2):109–143, 1913. (Cited on page 16.)
- [60] S. Earnshaw. On the nature of the molecular forces which regulate the constitution of the luminiferous ether. *Trans. Camb. Phil. Soc.*, 7:97 – 112, 1842. (Cited on page 16.)
- [61] R. Bowler, J. Gaebler, Y. Lin, T. R. Tan, D. Hanneke, J. D. Jost, J. P. Home, D. Leibfried, and D. J. Wineland. Coherent diabatic ion transport and separation in a multizone trap array. *Phys. Rev. Lett.*, 109:080502, Aug 2012. (Cited on page 17.)
- [62] Oleg V. Boyarkin and V. Kopysov. Cryogenically cooled octupole ion trap for spectroscopy of biomolecular ions. *Review of Scientific Instruments*, 85(3):033105, March 2014. (Cited on page 17.)
- [63] Wolfgang Paul. Electromagnetic traps for charged and neutral particles. *Rev. Mod. Phys.*, 62:531–540, Jul 1990. (Cited on page 18.)
- [64] R. I. Thompson, T. J. Harmon, and M. G. Ball. The rotating-saddle trap: a mechanical analogy to RF-electric-quadrupole ion trapping? *Canadian Journal of Physics*, 80(12):1433–1448, 2002. (Cited on page 18.)
- [65] L. D. Hinkle and B. R. F. Kendall. Pressure dependent damping of a particle levitated in vacuum. *Journal of Vacuum Science & Technology A*, 8(3), 1990. (Cited on page 21.)
- [66] E. T. Whittaker. On the general solution of Mathieu’s equation. *Proc. Edinburgh Math. Soc.*, 32:75–80, 1914. (Cited on page 23.)
- [67] Gaston Floquet. Sur les équations différentielles linéaires à coefficients périodiques. *Annales de l’École Normale Supérieure*, 12:47–88, 1883. (Cited on page 23.)
- [68] Cooling and heating of the quantum motion of trapped Cd<sup>+</sup> ions. *Ph. D. Thesis*, 2006. (Cited on page 24.)
- [69] Jan Eric Strang. On the characteristic exponents of Floquet solutions to the Mathieu equation. *Acad. Roy. Belg. Bull. Cl. Sci.*, 6(16)(7-12):269 – 287, 2005. (Cited on pages 25 and 26.)

- [70] W. Paul and H. Steinwedel. Ein neues massenspektrometer ohne magnetfeld. *Zeitschrift für Naturforschung A*, 8(7):448 – 450, 1953. (Cited on page 29.)
- [71] Ulf Von Zahn. Monopole spectrometer, a new electric field mass spectrometer. *Review of Scientific Instruments*, 34(1):1–4, 1963. (Cited on page 29.)
- [72] Nikolai Konenkov, Frank Londry, Chuanfan Ding, and D. J. Douglas. Linear quadrupoles with added hexapole fields. *Journal of the American Society for Mass Spectrometry*, 17(8):1063–1073, 2006. (Cited on page 29.)
- [73] A. L. Michaud, A. J. Frank, C. Ding, Xianzhen Zhao, and D. J. Douglas. Ion excitation in a linear quadrupole ion trap with an added octopole field. *Journal of the American Society for Mass Spectrometry*, 16(6):835–849, 2005. (Cited on page 29.)
- [74] S. R. Jefferts, C. Monroe, E. W. Bell, and D. J. Wineland. Coaxial-resonator-driven RF (Paul) trap for strong confinement. *Physical Review A*, 51(4):3112–3116, 1995. (Cited on page 29.)
- [75] H. Kaufmann, S. Ulm, G. Jacob, U. Poschinger, H. Landa, A. Retzker, M. B. Plenio, and F. Schmidt-Kaler. Precise experimental investigation of eigenmodes in a planar ion crystal. *Phys. Rev. Lett.*, 109:263003, Dec 2012. (Cited on page 29.)
- [76] J. E. Coppock, P. Nagornykh, Ian McAdams, and B. E. Kane. (*in preparation*). (Cited on pages 33 and 41.)
- [77] Jan Gieseler, Marko Spasenović, Lukas Novotny, and Romain Quidant. Nonlinear mode coupling and synchronization of a vacuum-trapped nanoparticle. *Physical Review Letters*, 112(10):1–5, 2014. (Cited on page 34.)
- [78] N. Akerman, S. Kotler, Y. Glickman, Y. Dallal, A. Keselman, and R. Ozeri. Single-ion nonlinear mechanical oscillator. *Phys. Rev. A*, 82:061402, Dec 2010. (Cited on page 34.)
- [79] Hao-Yu Wu, Yi Xie, Wei Wan, Liang Chen, Fei Zhou, and Mang Feng. A complicated Duffing oscillator in the surface-electrode ion trap. *Applied Physics B*, 114(1-2):81–88, 2014. (Cited on page 34.)
- [80] W. Wan, H. Y. Wu, L. Chen, F. Zhou, S. J. Gong, and M. Feng. Demonstration of motion transduction in a single-ion nonlinear mechanical oscillator. *Physical Review A*, 89(6):1–10, 2014. (Cited on page 34.)
- [81] John B. Fenn, Matthias Mann, Chin Kai Meng, Shek Fu Wong, and Craige M. Whitehouse. Electrospray ionization - principles and practice. *Mass Spectrometry Reviews*, 9(1):37–70, 1990. (Cited on page 38.)
- [82] Yenny Hernandez, Valeria Nicolosi, Mustafa Lotya, Fiona M Blighe, Zhenyu Sun, Sukanta De, I. T. McGovern, Brendan Holland, Michele Byrne, Yurii K. Gun'ko, John J. Boland, Peter Niraj, Georg Duesberg, Satheesh Krishnamurthy, Robbie

- Goodhue, John Hutchison, Vittorio Scardaci, Andrea C. Ferrari, and Jonathan N. Coleman. High-yield production of graphene by liquid-phase exfoliation of graphite. *Nature Nanotechnology*, 3(9):563–8, September 2008. (Cited on pages 38 and 40.)
- [83] J. A. Stratton. *Electromagnetic Theory*. Swedenborg Press, 2010. (Cited on page 42.)
- [84] Jan Gieseler. Dynamics of optically levitated nanoparticles in high vacuum. *Ph. D. Thesis*, Feb 2014. (Cited on page 58.)
- [85] M. Poggio, C. L. Degen, H. J. Mamin, and D. Rugar. Feedback cooling of a cantilever’s fundamental mode below 5 mK. *Phys. Rev. Lett.*, 99:017201, Jul 2007. (Cited on page 59.)
- [86] C. Zerbe, P. Jung, and P. Hanggi. Brownian parametric oscillators. *Phys. Rev. E*, 49(5):3626, 1994. (Cited on page 61.)
- [87] Steven W Smith. *Digital Signal Processing*. Elsevier Science, 2003. (Cited on pages 72, 73, and 74.)
- [88] Y. Ibaraki, U. Tanaka, and S. Urabe. Detection of parametric resonance of trapped ions for micromotion compensation. *Applied Physics B*, 105(2):219–223, March 2011. (Cited on page 95.)
- [89] A. Härter, A. Krüchow, A. Brunner, and J. Hecker Denschlag. Long-term drifts of stray electric fields in a Paul trap. *Applied Physics B*, 114(1-2):275–281, 2014. (Cited on page 98.)
- [90] Marion Thornton. *Classical Dynamics of particles and systems*. Saunders College Publishing, 1995. (Cited on page 104.)
- [91] L.D. Landau and E.M. Lifshitz. *Statistical Physics*. Elsevier Science, 3 edition, 2013. (Cited on page 110.)
- [92] Donald R. Huffman. *Absorption and Scattering of Light by Small Particles*. Wiley-VCH, 1998. (Cited on page 114.)
- [93] Pavel Nagornykh, Joyce E. Coppock, and Bruce E. Kane. *Applied Physics Letters (accepted)*, 2015. (Cited on page 117.)